Establishment of an inducible human pluripotent stem cell-based 3D model of Alzheimer's disease

Dissertation

zur Erlangung des Doktorgrades (PhD)

der Medizinischen Fakultät

der Rheinischen Friedrich-Wilhelms-Universität

Bonn

<u>Matthias</u> Alexander Sebastian Hebisch

aus Wuppertal

2020

Angefertigt mit der Genehmigung

der Medizinischen Fakultät der Universität Bonn

1. Gutachter:	Prof. Dr. med. Oliver Brüstle

2. Gutachter:	Prof. Dr. med. Dr. rer. nat. Wolfgang Wagner

Tag der mündlichen Prüfung: 6. November 2020

Aus dem Institut für Rekonstruktive Neurobiologie

Direktor: Prof. Dr. med. Oliver Brüstle

Table of Contents

Abbreviations

AAVS1	Adeno-associated virus 2 integration site 1
AD	Morbus Alzheimer (Alzheimer's disease)
AGE	Agarose gel electrophoresis
Amp	Ampicillin
APP	Amyloid precursor protein
APP-ICD	Amyloid precursor protein intracellular domain
Aβ	Amyloid β peptide
BABB	Benzyl-alcohol / benzyl-benzoate
BACE1	β-site APP cleaving enzyme 1 or β-secretase
BCA	Bicinchoninic acid
BME	β-Mercaptoethanol
bp	Base pairs
BSA	Bovine serum albumin
Cas9	CRISPR-associated system protein 9
CNS	Central nervous system
CRISPR	Clustered regularly interspaced palindromic repeats
CSF	Cerebro-spinal fluid
DACH1	Dachshund homolog 1
DAPT	N-[N-(3,5-Difluorophenacetyl)-L-alanyl]-S-phenylglycine t-butyl ester
DMEM	Dulbecco's modified eagle medium
DMSO	Dimethyl sulfoxide
DNA	Deoxyribonucleic acid
dNTP	Deoxyribonucleotide triphosphate
DOX	Doxycycline
EDTA	Ethylenediaminetetracetic acid
EGF	Epidermal growth factor
ELISA	Enzyme-linked immunosorbent assay
FA	Formic acid

FAD	Familial Alzheimer's disease
FGF	Fibroblast growth factor
GABA	*gamma*-Aminobutyric acid
GAD	Glutamate decarboxylase
GFP	Green fluorescent protein
HOX	Homeobox protein
HRP	Horseradish peroxidase
imAP	Inducible APP-PS1-mCherry cassette
iPSC	Induced pluripotent stem cell
IRES	Internal ribosomal entry site
kb	Kilo bases
kDa	Kilo Dalton
LB	Lysogeny broth
LDS	Lithium dodecyl sulfate
LN	Laminin
LOH	Loss of heterozygosity
LSFM	Light-sheet fluorescence microscopy
Lt-NESC	Long-term neuroepithelial stem cell
MAPT	Microtubule-associated protein tau
MCI	Mild cognitive impairment
MES	2-(N-Morpholino)ethanesulfonic acid
mRNA	Messenger ribonucleic acid
MVB	Multi-vesicular body
NGMC	Neural growth medium with cAMP
NHEJ	Non-homologous end joining
NPC	Neural precursor cell
NSC	Neural stem cell
OCR	Oxygen consumption rate
P-tau	(Hyper-) phosphorylated microtubule-associated protein tau
PAGE	Polyacrylamide gel electrophoresis
PAX6	Paired box 6
PBS	Phosphate-buffered saline

PET	Positron-emission tomography
PLZF	Promyelocytic leukemia zinc finger
PO	Polyornithine
PS-1	Presenilin-1
PSC	Pluripotent stem cell
PVDF	Polyvinyiledene fluoride
ReN VM	ReNeuron cells with V-MYC
RI	Rho-associated coiled-coil containing protein kinase (ROCK) inhibitor (Y-27632)
RNP	Ribonucleoprotein complex
RO	RO4929097
sAPP α/β	Soluble amyloid precursor protein α/β
SDD	Semi-denaturing detergent
SDS	Sodium dodecyl sulfate
SNP	Single-nucleotide polymorphism
SOX1 / SOX2	Sex-determining region Y box 1 / 2
SSEA 3/4	Stage-specific embryonic antigen 3/4
TALEN	Transcription activator-like effector nuclease
Tau	Microtubule-associated protein tau
TB	Terrific broth
TBS(-T)	Tris-buffered saline (with Tween-20)
TRA-1-60 / TRA-1-81	Podocalyxin
ZFN	Zinc finger nuclease
ZO-1	Zonula occludens 1

1. Introduction

1.1. Morbus Alzheimer
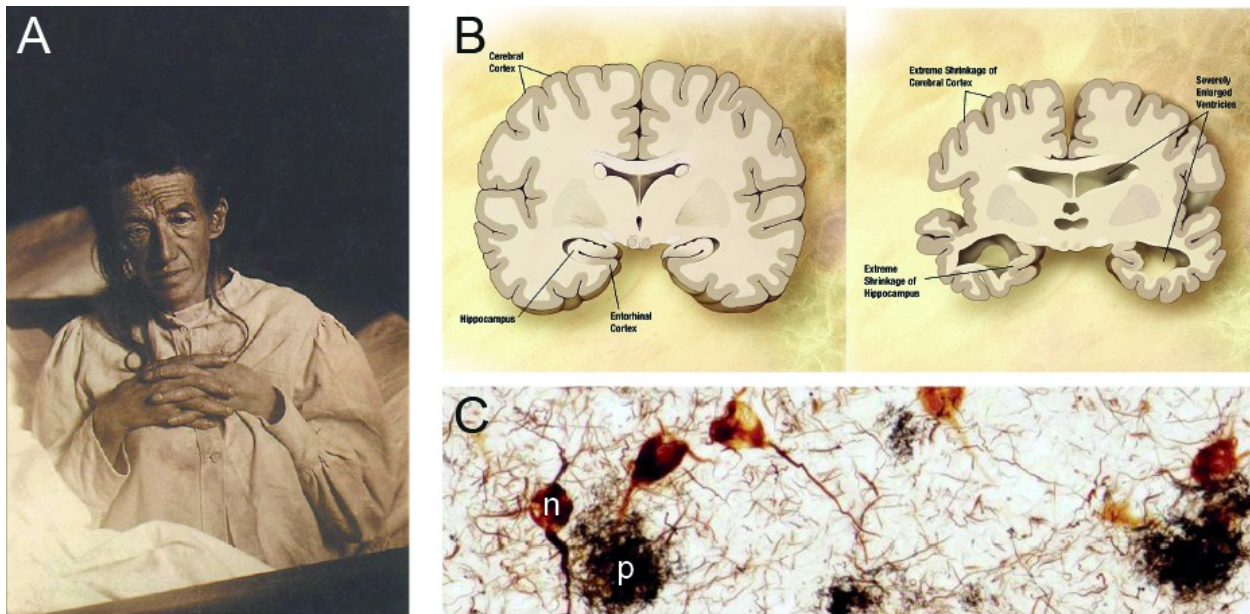
Figure 1.1 Alzheimer's disease
(**A**) Historic photograph of Auguste Deter taken in 1902, the first patient described by Alois Alzheimer. Image part of the public domain, photographer unknown. (**B**) Comparison between control (left) and AD patient (right) brains. Note the overall volume reduction, enlarged ventricles and thinning of the gyri. Image from the Alzheimer's disease education and referral center, National Institute of Aging, Bethesda, Maryland, USA. (**C**) Campbell-Switzer histological staining of AD patient gray matter. Extracellular deposition of amyloid plaques (p) and intracellular formation of neurofibrillary tangles (n). Image modified from neuroscienceassociates.com.

1.1.1. Clinical presentation and epidemiology

In 1907, Alois Alzheimer first described a patient with "presenile dementia" (Fig. 1.1 A). *Post mortem* examination of the patient's brain revealed substantial loss of brain matter and distinct morphological changes, most notably enlarged ventricles and broadened sulci (Fig. 1.1 B). Histopathology uncovered plaques and tangles that could be stained with silver using the Bielschowsky method (compare Fig. 1.1 C, Mirra et al., 1991). Since its discovery, Alzheimer's disease has become a household name as the leading cause for age-related dementia currently affecting approximately 46 million patients. On average, females are more often affected than males (16 % of females vs. 11 % of

males over 71 years), a phenomenon that can not be explained by lower mortality in the female population (Hebert et al., 2013). The definitive diagnosis is generally difficult due to variable and non-exclusive symptoms that partly overlap with other syndromes like vascular dementia or Pick's disease. New diagnostic tools such as plasma/CSF Aβ measurement or Aβ-PET can boost diagnostic confidence, but AD is still definitely confirmed only via brain histopathology (Villemagne et al., 2018, Wurtman, 2015).

The disease onset is not sharply defined. Instead, patients or their families notice increasing difficulty to perform complex cognitive tasks or remember recently learned information, especially in short-term memory. Termed mild cognitive impairment (MCI), this phenomenon is considered the prodromal stage of Alzheimer's disease (Petersen et al., 2001, 2018). MCI can be diagnosed by a variety of cognitive tests, so it is often listed in the inclusion criteria of clinical studies that assess the efficacy of potential AD treatments. With further progression, patients reach early stage Alzheimer's disease. Loss of cognition and memory becomes apparent and fine motor skills degrade rapidly. In addition to difficulties retaining new information, many patients undergo personality changes such as mood swings or atypical behavior, that place an additional burden on caregivers and may necessitate constant supervision (Chen et al., 2018, Grabher, 2018). During late stage Alzheimer's disease, cognition and motor functions are heavily disturbed, and a large fraction of memories, safe earlier episodic memory and implicit memory, are lost. The last disease stage encompasses the stereotypical loss of recognition of friends, loved ones or the own home, as well as frequent profound confusion, hallucinations or seizures. AD ends in death, on average 3 – 9 years after initial diagnosis (Lane et al., 2018).

AD risk is strongly linked to a small number of genetic factors and weakly to numerous others. Mutations of the amyloid precursor protein (APP), presenilin 1 and 2 (PS-1, PS-2), APP duplication, or trisomy 21 (Down syndrome) cause an autosomal dominant, early onset variant of AD (EOAD). These mutations directly promote β-amyloid generation and are often passed down in families, leading to the term "familial AD" or FAD (Selkoe et al., 2016). However, FAD accounts for only about 5 % of AD cases. The remainder is classified as sporadic AD, and typically starts later in life (late onset AD, LOAD). LOAD does not exhibit mendelian inheritance, but is associated with numerous

genetic risk factors. Most importantly, the apolipoprotein E ε4 allele variant (APOE ε4) is highly enriched in LOAD patients (Corder et al., 1993). In comparison to the most common ε3/ε3 genotype, the ε3/ε4 and ε4/ε4 genotypes increase lifetime AD risk 3-fold and 12-fold, respectively (Michaelson, 2014). Genome-wide association studies (GWAS) discovered further LOAD-associated gene variants like the microglial receptors TREM2 and CD33, or less well-known genes like CR1, BIN1 or MS4A4A that confer low to moderate risk increases (Atagi et al., 2015, Chan et al., 2015, Guerreiro et al., 2013, Naj et al., 2014).

1.1.2. Amyloid pathology
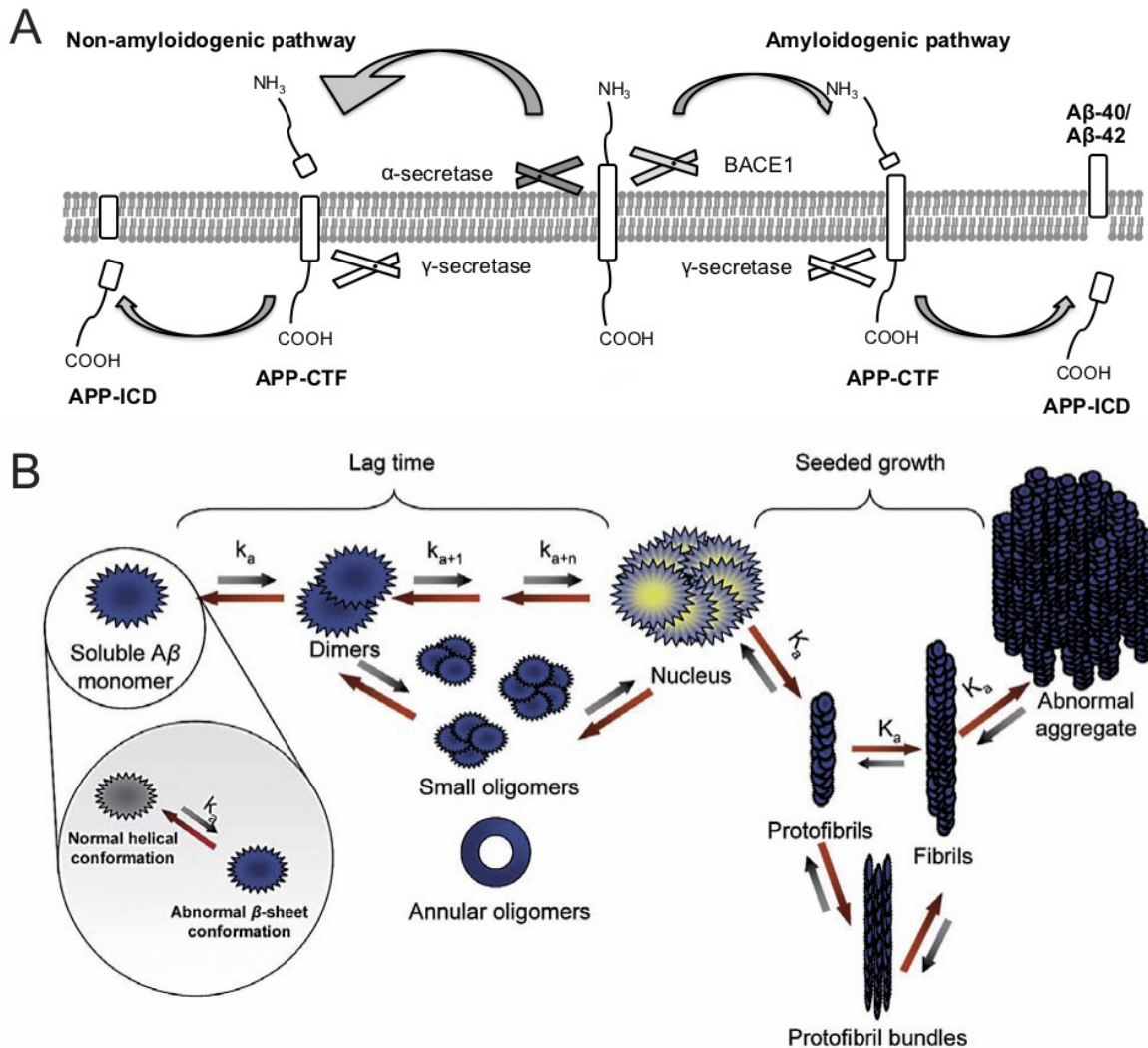
Figure 1.2 Processing and aggregation kinetics of the amyloid precursor protein
(**A**) APP is dominantly processed by sequential cutting of α-secretase and γ-secretase in the non-amyloidogenic pathway. Alternatively, processing by β- (BACE1) and γ-secretase leads to Aβ release, the 40 and 42 amino-acid isoforms being most common. (**B**) Schematic overview of the diverse stages of Aβ aggregation. Lower-order aggregates are prone to spontaneous dissolution, whereas higher-order fibrils are stable. Modified from Finder et al., 2007.

AD patient brain tissue contains extensive extracellular deposits of aggregated protein, known as amyloid. These deposits predominantly consist of the small endogenous peptide amyloid β (Aβ) that is generated in neurons by proteolytic cleavage of the amyloid precursor protein (APP). APP is a type I transmembrane protein with distinct extracellular, membrane and intracellular domains that can be separately liberated through secretase processing (Finder et al., 2007). The majority of APP is cleaved

sequentially by α-secretase and γ-secretase (Fig. 1.2 A). The first cleavage step releases the soluble extracellular domain (sAPPα) from the C-terminal fragment (APPα-CTF). Then, γ-secretase cleaves off the intracellular domain (APP-ICD). The remaining membrane peptide is not aggregation prone. However, in a pathogenic setting, β-secretase cleavage can take precedence over α-secretase in endocytic vesicles (Olsson et al., 2014). In that case, β-secretase cleaves closer to the membrane than α-secretase, resulting in liberation of a longer extracellular domain (sAPPβ). The remaining peptide (APPβ-CTF, also known as C99) is then processed by γ-secretase. γ-secretase can bind to a number of different, yet closely positioned sites within C99. Depending on the site of first binding, a plethora of Aβ peptides of different lengths can be generated, including 51, 49, 48, 46, 45, 43, 42, 40 and 38 amino acid variants (Olsson et al., 2014). Clinically, $A\beta_{42}$ and $A\beta_{40}$ have proven most relevant, for example as CSF biomarkers (Hu et al., 2015, Lehmann et al., 2018). Specifically, there is mounting evidence that the relative abundance of these two isoforms, termed the $A\beta_{42/40}$ ratio, is a major predictor of amyloid pathogenicity in patient brains and *in vitro* models (Arber et al., 2019, Kwak et al., 2020). β-secretase operates most efficiently in acidic environments like acidified endosomes, and recent reports suggest that initial Aβ oligomerization might occur in the endosomal-secretory pathway (Friedrich et al., 2010, Takahashi et al., 2002). Aβ enrichment in endosomes and amyloid fibril formation in multi-vesicular bodies (MVB) was observed in human cells lines (HEK 293T, SH-SY5Y, THP-1) upon treatment with Aβ. Problematically, the fibril formation process is thermodynamically favored over fibril dissolution and does not necessarily occur step-wise, especially in the presence of catalyzing factors like metal ions that stabilize aggregation-prone Aβ conformations (Fig. 1.2 B, Hane et al., 2014). Therefore, the most promising way of approaching amyloidosis is by preventing or interfering with the most toxic lower order oligomers and protofibrils (Benilova et al., 2012, Stroud et al., 2012, Tanokashira et al., 2017). Many therapeutic candidates have aimed to reduce Aβ production, accumulation or aggregation in the last decades, including secretase inhibitors and antibodies (Bullock et al., 2018, Huang et al., 2012). Still, no efficacious treatment has been found.

Over time, extracellular amyloid forms large, insoluble aggregates termed plaques. Amyloid plaques are divided into two major types, neuritic and diffuse (Bussière et al.,

2004, Vinters et al., 2012). Neuritic plaque deposition is most typical for AD in the human brain and strongly associated with synaptic terminals (Sadleir et al., 2016). Neuritic plaques consist of a central amyloid aggregate with condensed or "burned out" morphology and several dystrophic, p-tau-positive neurites in its immediate vicinity. "Dystrophic" means that the neurites are irregularly shaped, i.e. swollen or crooked and likely to be incapable to fulfill their physiological function. Dystrophic neurites also display enrichment of presynaptic proteins and β-secretase (BACE1, Sadleir et al., 2016). This constellation is unsurprising as APP's physiological functions have been proposed to involve pre-synapse maintenance and long-term potentiation, both of which are measurably affected in APP-KO mice (Tyan et al., 2012). Overall, neuritic plaques appear to be specifically structured functional units that arise from highly specialized, non-physiologic pre-synaptic terminals. It is still unclear whether these structures represent dysregulated synapses caught in a vicious cycle of Aβ generation or whether they form to sequester surplus APP breakdown products into extracellular deposits (plaques). One notable hypothesis links the central plaque core to the surrounding neurites by suggesting that intracellular Aβ aggregation in the somatic or nuclear compartments causes dystrophic collapse of the neurites followed by neuronal death (Pensalfini et al., 2014). Opposing data from an AD mouse model show amyloid plaque formation occurring in a dense, extracellular manner in *in vivo* live-cell imaging, but the report is difficult to judge due as the model relies on overexpression and an amyloid dye that interferes with Aβ deposition (Cohen et al., 2009). Distinct from the neuritic plaques, amyloidosis also encompasses diffuse plaques that lack distinguishable structure or sharply defined borders and that tend to be larger than neuritic plaques (20 μm vs. 100 μm) (Bussière et al., 2004). Several concurrent hypotheses address the creation of diffuse plaques ranging from regular plaques that have not been condensed by immune cells or astrogliosis to amyloid leakage from blood vessels. Either way, the exact origin of diffuse and condensed plaques is not yet clear.

While certainly the most well known hallmark of AD, cerebral amyloidosis is insufficient for AD diagnosis or prognosis since, on the one hand, plaque load correlates poorly with neurodegeneration across brain regions, and, on the other hand, several amyloid PET studies detected participants with enormous plaque load but no cognitive impairment (Huang et al., 2012, Snowdon, 2003, Wurtman, 2015).

1.1.3. Tauopathy
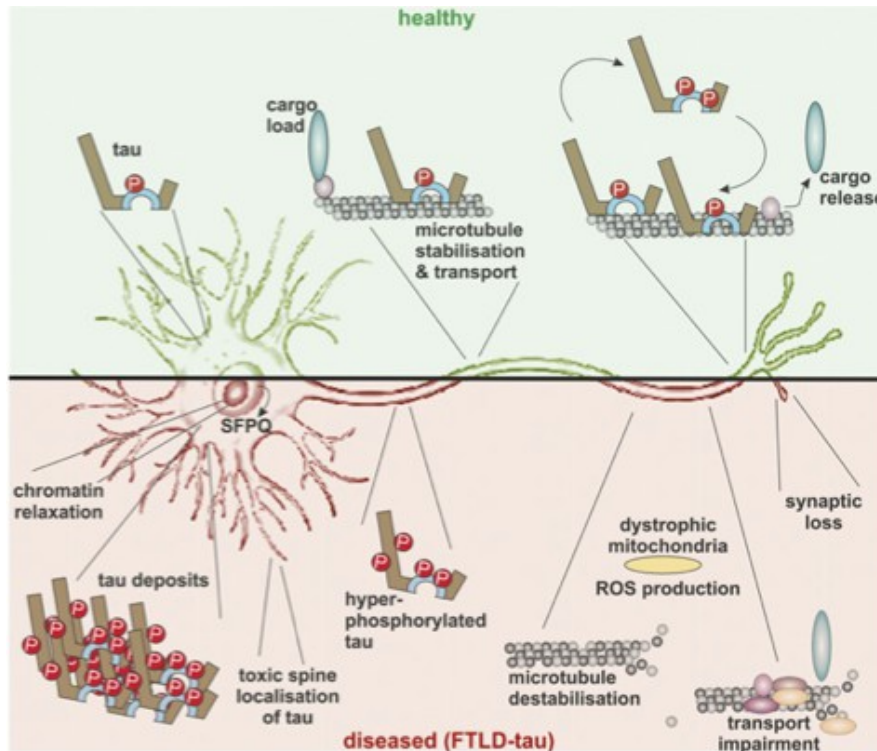
Figure 1.3 Homeostatic and pathologic roles of tau
Schematic overview of the roles of tau in healthy (upper panel) and diseased (lower panel) states. Limited tau phosphorylation is pivotal for microtubule stabilization and cargo transport. Hyperphosphorylated tau is highly prone to aggregation and loses its microtubule stabilizing function, impairing cytoskeleton dynamics, cargo transport, mitochondrial transport and thus distal process maintenance. Modified from Bodea et al., 2016.

In contrast to amyloid plaque load, accumulation of hyperphosphorylated tau (microtubule-associated protein tau, MAPT) and deposition of neurofibrillary tangles has been shown repeatedly to correlate with neurodegeneration, and common models of AD pathology development place tau pathology well after amyloid deposition (Sasaguri et al., 2017). While this assumption fits the amyloid cascade hypothesis, it has been excruciatingly difficult to test in mouse models that do not recapitulate disease staging (Sasaguri et al., 2017). Furthermore, the staging divide has sparked the "tau hypothesis" that assumes tau hyperphosphorylation as the initial cause of AD. Tau is a complex axonal protein with six splice isoforms in adult humans (Bussiere et al., 2000). Alternative splicing can result in exons 2, 2+3 and 10 being differentially present. Exon 10 is a fourth repeat domain that is included mostly in the mature brain, so tau is often

distinguished between immature "three-repeat" (3R) and mature "four-repeat" (4R) isoforms. For AD in particular, the 4R isoforms are thought to be most pathogenic. Recent mouse studies demonstrated convincingly that, at least in the mouse brain, 4R human tau is highly neurotoxic, whereas 3R tau is not (Schoch et al., 2016). This does not mean that 3R tau is non-pathogenic, as it has been implicated in syndromes like Pick's disease and frontotemporal dementia (Bodea et al., 2016, Irwin et al., 2016). In the adult human brain, 3R and 4R tau isoforms balance out at a 50:50 ratio, whereas the developing brain expresses the 3R isoforms almost exclusively (Caillet-Boudin et al., 2015). In physiological conditions, tau is attached to axonal microtubules via its repeat domains, where it serves to improve microtubule stability (Fig. 1.4). Microtubule binding is regulated by tau phosphorylation, but while the protein contains 79 putative phosphorylation sites when all optional exons are included, only about half are phosphorylated in homeostatic conditions. In pathology, hyperphosphorylation drives an accumulation of negative charges on the protein, thus interfering with the binding to negatively-charged microtubules. In short, increasing phosphorylation detaches the protein from the axonal microtubules and enables it to enter the somatodendritic segment (Stoothoff et al., 2005). Without the stabilizing tau, microtubule-dependent mechanisms like axonal transport are increasingly likely to fail. These mechanisms include replenishing synaptic vesicles, various materials for axonal and synaptic maintenance and mitochondrial transport for energy provision and quality management. The effects of transport impairment are easy to investigate via microscopic inspection of neural processes: Stuck cargo accumulates in "swellings", local enlargements of the process that leave the cytoskeleton intact (Bussiere et al., 2000, Mertens et al., 2013). In late stages, however, these swellings can produce a beads-on-a-string look and potentially persist after the neurite has fully degenerated, leaving a spotted trace pattern. Tau proteins are relatively unstructured in physiological circumstances, but undergo highly specific changes during hyperphosphorylation and recruitment into a p-tau fibril (Inoue et al., 2014). Tau in fibrils is folded up, assuming a "paperclip" morphology that presents specific, discontinuous epitopes for antibody development (Jeganathan et al., 2008). Today, dozens of tau antibodies have been raised against various stages of (site-specific) phosphorylation or conformational states. The most common one - AT8 - recognizes double-phosphorylated tau in the Ser202 and Thr205 positions. Also relevant

is MC-1 for detection of the discontinuous paperclip epitope in fibrillar tau. Similar to Aβ fibrils, cytotoxic p-tau fibrils have been hypothesized to multiply in a prion-like manner once formed and recent research showed that p-tau pathology can spread across a mouse brain from a primary site of infection (Goedert et al., 2017, Mudher et al., 2017). This finding has enormous implications for approaches to model AD or other tauopathies because on the one hand, p-tau aggregation appears to be a continuous process, again similar to Aβ fibril formation once a seed has been formed, and on the other hand spreads between neurons. Intriguingly, *post mortem* studies on recipients of human brain-derived growth factors hint at transmission of amyloid plaques (Jaunmuktane et al., 2015), and other pathologies have been linked to retrograde infection with pathogenic agents, e.g. after oral uptake of aggregated α-synuclein in Parkinson's disease mouse models (Garrido-Gil et al., 2018).

The cause of p-tau aggregation is, like for Aβ, not fully understood. One current hypothesis states that p-tau is simply aggregation-prone in a stochastic, concentration-dependent manner. Studies on p-tau recruitment into stress granules (an RNA sequestering mechanism in response to cell stress) via interaction partners like TIA-1 unveiled a putative location of local p-tau hyperaccumulation (Apicco et al., 2018, Ash et al., 2014, Vanderweyde et al., 2016).

Subcellular localization of p-tau appears to depend on the context. In neuritic plaques, p-tau is prominently present in dystrophic neurites in the immediate vicinity of the amyloid aggregate (Serrano-Pozo et al., 2011). Outside the plaque vicinity, p-tau is often found accumulated around nuclei and in the dendrites of affected neurons, although it should be noted that only a small fraction of neurons is ever affected at once so that AD brain slices present a salt-and-pepper pattern of isolated p-tau-positive cells (Blazquez-Llorca, 2010). In the neuronal soma, neurofibrillary tangles appear as thick, curled up fibers. In extreme cases, the neuron itself has already degenerated leaving only the insoluble p-tau material (termed "husks" or "remnants") (Fukutani et al., 1995). In contrast, early degeneration is obvious from the breakdown of axonal transport as first shown by strongly p-tau-positive swellings along the axon and later axonal fragmentation into beads-on-a-string dot patterns of highly p-tau material along the axons' former path (Kanaan et al., 2013).

1.1.4. Neuroinflammation

Microglia and astrocytes normally form an effective system to remove pathogens and waste products from the brain and to protect and support neurons. To this day, the exact reasons for their failure to cope with the amyloid or p-tau pathology in AD patient brains remains a mystery. Both microglia and astrocytes are stimulated by the presence of amyloid plaques and react in specific ways. Astrocytes become activated (as indicated by increased GFAP expression), start proliferating and cluster around plaque sites (Bouvier et al., 2016). Microglia undergo a similar activation by retracting their finely arborized processes and migrating to the plaque site (Thériault et al., 2015). It has been hypothesized that this behavior serves to form a protective shell around the plaque in order to limit the spread of toxic Aβ species and plaque growth (Scheffler et al., 2011). In fact, microglia and astrocyte clusters occur dominantly around the condensed plaques. However, the microglia do not seem to be responsible for the growth-limiting effect of the local reactive changes (Grathwohl et al., 2009). A large body of literature addresses ways in which the microglial response is attenuated in the AD brain, for example via chronic Aβ overexposure or receptor interactions (e.g. TREM2, CD33) (Atagi et al., 2015, Bailey et al., 2015, Chan et al., 2015, Hellwig et al., 2015). Another set of mechanisms that has been implicated in neuroinflammation relates to a microglial shift towards a proinflammatory phenotype. In this state, microglia secrete proinflammatory cytokines as well as neurotoxic reactive oxygen species (ROS) and commence unwarranted phagocytosis of neuronal components (Solito et al., 2012). On a small scale, this entails elevated synaptic pruning. Neuronal connectivity is physiologically regulated in part by microglia that selectively remove superfluous synapses. When dysregulated, this process can become excessive, especially in conjunction with complement system activation. The resulting reduction in overall network connectivity is likely involved in cognitive impairment and other synapse-dependent mechanisms, such as memory retention (Hong et al., 2016). On a larger scale, hyperactivated microglia can also engage in phagocytosis of live neurons, a process termed neurophagy (Neniskyte et al., 2016).

1.1.5. Synaptic impairment

Synapses serve as the functional units of information processing in the brain. In Alzheimer's disease, the synaptic integrity is impaired in several ways. Mouse studies have shown that APP itself has a limited but considerable role in synapse maintenance, learning and memory, especially during aging (Tyan et al., 2012). APP might have subtly different roles in human neurons, but cognitive effects of altered synaptic APP levels still need to be studied, for example in cases of APP triplication or Down syndrome (Shi et al., 2012, Wiseman et al., 2015). APP's breakdown products, first and foremost Aβ, have well established synaptotoxic properties, particularly the $A\beta_{42}$ variant (Mucke et al., 2000). Oligomeric Aβ (Aβo), on the other hand, directly interacts with the cellular prion protein (PrPc) and glutamate receptors (mGluR) to cause intracellular Ca^{2+} elevation and kinase activation via Fyn (Bush et al., 2002). The resulting excitotoxicity and tau phosphorylation are implicated in the loss of postsynaptic densities, dendritic spine shrinkage and overall neuronal decline, but can be rescued by Fyn inhibition (Kaufman et al., 2015). In the plaque stage of AD, presynapses are closely associated with plaques even though it is unclear whether they contribute to their initial formation, growth or maintenance, or whether they are more resilient to degeneration than their postsynaptic counterparts and undergo reactive changes at the plaque site (Sadleir et al., 2016). Irrespectively, presynaptic proteins like synapsin are highly enriched in the vicinity of cored plaques along with components of the APP processing machinery, such as β-secretase. Together these processes suggest a major role of synaptic structures in the initial appearance and growth of extracellular amyloid plaques and, at the same time, suffer directly from the effects.

1.1.6. Neuronal degeneration

In the later stages of AD, neuronal loss leads to progressive shrinkage of brain matter characterized by thinning gyri, deepening sulci and ventricle enlargement. Neurodegeneration in AD has been linked to numerous independent effects that encompass Aβ, tau, and even other cell types like astrocytes and microglia. It should be

noted that neuronal loss in AD is not an orchestrated, population-wide phenomenon, but rather affects a small fraction of relatively isolated cells at any given time, i.e. neurons die surrounded by seemingly healthy cells, not in groups (Perl, 2010).

Aβ pathology can potentially cause neuronal degeneration in a multitude of ways. Extracellular Aβo interactions in the synaptic cleft or with the neuronal membrane likely cause Ca^{2+} influx and other ion misbalances (Shirwany et al., 2007). Intracellular Ca^{2+} is an important signal for apoptosis, among others. The Ca^{2+} challenge can be precipitated even further by Aβo interactions with astrocytes. Astrocytes support and tune neuronal activity via precise regulation and buffering of neurotransmitters, most importantly glutamate, at the synapse and in the interstitium (Dallérac et al., 2013). Aβo have been shown to impair glutamate reuptake in astrocytes, again causing increased neuronal activation and aggravating excitotoxicity (Hoshi et al., 2018). Furthermore, Aβo activate the receptor tyrosine kinase Fyn and thus directly elevate tau phosphorylation (Crews et al., 2010). Intracellularly, Aβ generation in secretory vesicles can lead to pore formation in vesicle membranes or to fibril formation (Takahashi et al., 2002). Intracellular Aβ can also interfere with processes like mitochondrial protein import leading to an energy crisis and reducing cellular stress resistance (Cenini et al., 2016, Pinho et al., 2014). Interestingly, a current hypothesis on the higher AD incidence in post-menopausal women argues that estrogen signaling exerts strong protective effects on mitochondria via ROS reduction, and that, following menopause, women are effectively more at risk than men (Vina et al., 2010). In summary, amyloid and p-tau pathology apply an array of different cellular stressors to affected neurons, e.g. axonal transport impairment, mitochondrial fragmentation, excitotoxicity and oxidative stress that appear to collaborate towards neuronal loss. Interestingly, the main driver of cell death is still a matter of debate. While dying neurons in AD patient brains often show apoptotic markers like cleaved caspase 3 (cCas3), the extended languishing of dysfunctional neurons makes an argument in favor of necrotic processes as apoptosis is typically fast and efficient. Independently, recent studies have implied innate immune surveillance, either through microglia or cell-autonomous necroptosis, as the major degenerative mechanism of dystrophic neurons (Richards et al., 2016).

1.2. Models of Alzheimer's disease

1.2.1. Mouse models

Mouse models of Alzheimer's disease have been introduced shortly after the FAD mutations in the APP and presenilin genes were discovered (Sasaguri et al., 2017). Overexpression of these transgenes causes elevated Aβ generation and leads to deposition of plaque-like structures in the mouse brain within, depending on the model, 1.5 - 12 months. Although these models recapitulate plaque development and varying degrees of functional impairment, there is a general lack of NFT pathology and large-scale neuronal loss (Hsiao et al., 1995, Lalonde et al., 2005, Verret et al., 2012). Extensive efforts to induce p-tau deposition resulted in multiple-transgene models, e.g. the 3xTg model that overexpresses APP, presenilin and mutant tau (Oddo et al., 2003). Although this strategy succeeded to recapitulate both major AD pathologies, it is unsuitable to illuminate the connection between amyloid and p-tau pathologies as mutant tau overexpression is sufficient to drive tauopathy in mouse models. The underlying problem of mouse models for AD is the substantial physiological difference between mice and humans, especially in regard of tau physiology. Wild-type mice do not develop AD or similar pathologies, and mouse Aβ is less aggregation-prone than its human homolog (Nalivaeva et al., 2013). Similarly, mouse tau is not subject to complex splicing and numerous isoforms, and many AD-relevant human tau isoforms are highly neurotoxic in mouse models (Schoch et al., 2016). Accordingly, AD mouse models have a devastating track record of predictive validity for human AD therapies. No curative treatment and only a handful of agents for short-term symptom suppression have been discovered despite hundreds of candidates entering into clinical trials (Cummings et al., 2014). In 2017, over 100 drugs were in clinical trials, 28 out of which had progressed phase III (Cummings et al., 2017, Umar et al., 2017).

1.2.2. 2D and 3D cell culture models
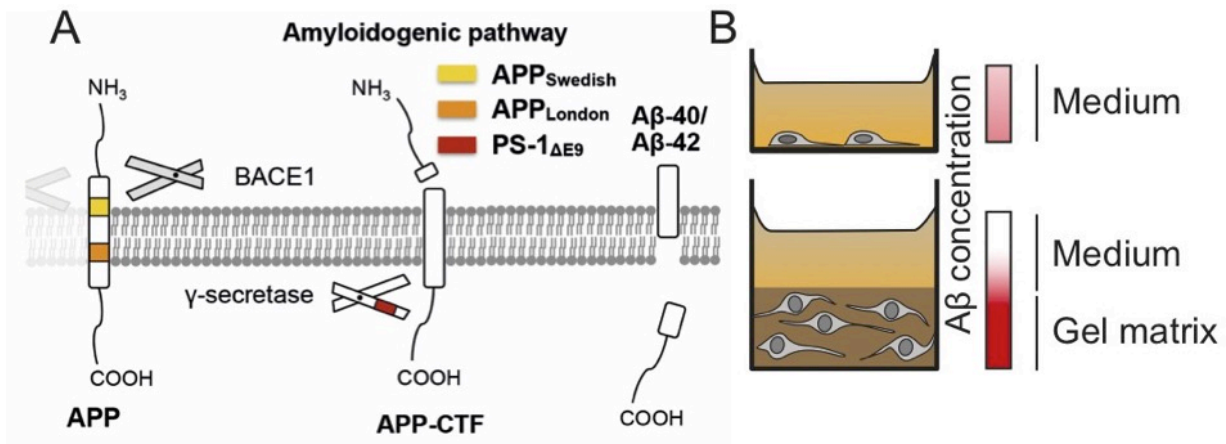
Figure 1.4 Familial AD mutations increase Aβ release and enrichment in 3D cultures
(**A**) Autosomal dominant mutations in the APP and Presenilin-1 genes lead to AD by increasing BACE1 cleavage propensity of the APP peptide and shifting the preferred Aβ isoform from 40 to 42. (**B**) Embedding of neuronal cultures in a 3D matrix prevents Aβ removal during medium change, leading to local enrichment of Aβ in the neuronal vicinity.

Compared to mouse models, cell culture models of AD offer considerable advantages, but also significant drawbacks. First, cell culture models can be established in the human system, avoiding many of the above-mentioned physiological pitfalls. However, the downside is the utter removal of the physiologic environment, i.e. tissue architecture, supporting cells, immune, metabolic and hormonal influences and so on. Still, cell culture models enable picking apart single components of complex systems, one interaction at a time, and offer the option to increase complexity by addition of more system components, such as other cell types. Most *in vitro* cell culture relies on cells adhering to a stiff, flat scaffold with one half of their surface area, while the other half is exposed to media. The technique is straightforward and has served well in uncounted cytological studies since its introduction in the early twentieth century. Cells in 2D culture systems continue their basic metabolic functions, divide, react to stimulants and toxins and so on, but many *in* vivo characteristics remain elusive. For example, neurons exhibit "neuronal" morphology, show electric activity and form synapses, but mature slowly in 2D (Liedmann et al., 2012, Zhang et al., 2016). Astrocytes fail to achieve their typical morphological complexity and express markers of reactive gliosis (East et al., 2009, Placone et al., 2015). Thus, 2D culture environments cannot fully replicate function or

architecture. Even more problematic for disease modeling of extracellular pathologies is the lack of ECM-like structures to capture secreted pathogenic material. Instead, it dilutes into the supernatant and is removed during medium change (Choi et al., 2014). Accordingly, while 2D model systems could successfully recapitulate a subset of AD features (Aβ aggregation, p-tau, degeneration), they miss fully differentiated hallmarks (e.g. large aggregates, neuritic plaques, NFTs) (Mertens et al., 2013).

3D culture techniques aim to circumvent these challenges by providing middle ground between 2D systems and tissue culture. Condensing small clumps of precursor cells until cell-cell contacts form establishes small, self-contained spheroids. So-called aggregate cultures can be subdivided into embryoid bodies, neurospheres and organoids. Embryoid bodies derive from free-floating (or gel-embedded) PSC aggregates and contain differentiated tissues from all germ layers with high variation (Simunovic et al., 2017). Aggregating NSCs or young neurons generates neurospheres (Jensen et al., 2006). Finally, organoids undergo directed differentiation into e.g. the CNS fate, but are then left to self-organize (Lancaster et al., 2015). The typical cellular diversity and complex architecture of tissues is only present in organoids, e.g. inside-out development of cortical layers. In contrast to the methods above, matrix 3D cultures are more reductionist. Still, embedding cells in a gel to form relatively homogenous layers enables authentic cell morphology, cell-cell interactions, and provides a flexible scaffold that can be remodeled or supplemented as needed (Chandrasekaran et al., 2017, Liedmann et al., 2012).

A 3D matrix model of AD has been prominently used to capture major disease hallmarks in 2014 by differentiating immortalized human NSC-like cells (ReN cell VM) while overexpressing $APP_{Swe/Lon}$ and PS1-ΔE9 mutant proteins (Choi et al., 2014). In the RenVM model, Aβ deposits formed within seven weeks and p-tau pathology developed after 17 weeks. The model displayed only minute changes to cell viability, though, and since RenVM cell-derived neurons do not form properly functional synapses, network activity could not be assayed. Nonetheless, Choi and colleagues demonstrated the feasibility of *in vitro* AD modeling and successfully showed the efficacy of Aβ-reducing drugs in preventing both Aβ and p-tau pathology, thus confirming the amyloid cascade hypothesis (Selkoe et al., 2016). Recently, the RenVM model has been employed in a proof-of-concept spheroid-based high-throughput screening platform by aggregating

FAD-transgenic RenVM cells in custom 96-well plates (Jorfi et al., 2018). It has also been used to probe the importance of the $A\beta_{42}:A\beta_{40}$ ratio, a major predictor of $A\beta$ pathogenicity (Kwak et al., 2020.) The modularity of gel matrix cultures also allows for inclusion of e.g. foreign materials like $A\beta$ aggregates to study kinase pathways (Zhang et al., 2014). Conversely, attempts to model AD in 2D cultures were not able to recapitulate plaque-like amyloid deposition and p-tau pathology in a comprehensive fashion, although studies in trisomy 21 iPSC-derived neurons found small-scale amyloid deposition when focusing on clumps of neural cell bodies (Shi et al., 2012). This validates the hypothesis behind creating high-density matrix 3D models for extracellular aggregate pathologies, i.e. secreted proteins, like $A\beta$, accumulate locally and cross the threshold of aggregate formation (D'Avanzo et al., 2015). Examples like these show the adaptability and complementarity of 3D culture systems for basic research, model development and screening setups.

1.3. Human induced pluripotent stem cells
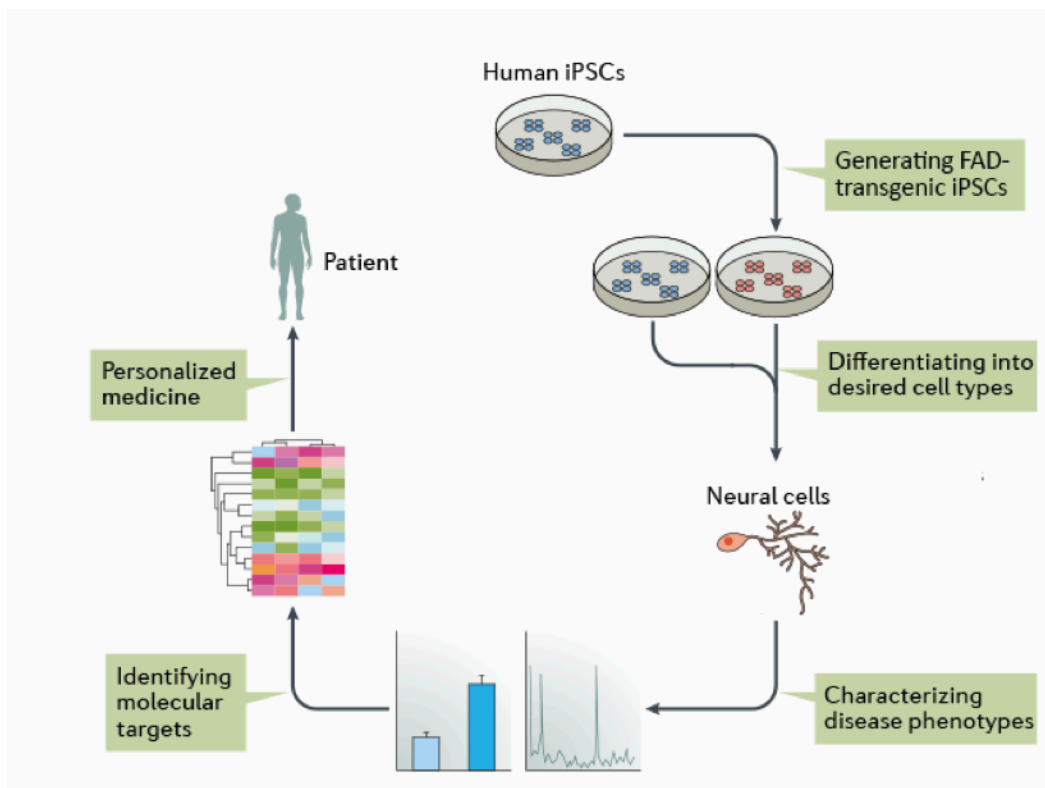
Figure 1.5 iPSCs in Alzheimer's disease modeling and drug target discovery
Induced pluripotent stem cell technology enabled robust access to neural cells from disease-affected and control individuals. Somatic cells can be reprogrammed using the transcription factors OCT4, SOX2, KLF4

and C-MYC. Reprogrammed iPSCs can be genetically modified to express transgenes. Following differentiation into mature neurons, transgene-expressing cells can be compared to non-expressing controls. Phenotypic differences are characterized and used to identify target candidates for drug discovery, ideally culminating in new therapeutic approaches. Modified from Shi et al., 2017.

The advent of reprogramming technology brought about an enormous increase in the usefulness of stem cell-based techniques for disease modeling. Starting from Waddington's epigenetic landscape, the team of Shinya Yamanaka managed to drive adult fibroblasts back to the earliest stages of development by overexpression of the four transcription factors OCT4, KLF4, SOX2 and C-MYC (OKSM) first in mouse and later in human fibroblasts (Takahashi et al., 2007, 2006). The OKSM cocktail serves as pioneering factors that open up heterochromatin and jumpstart the establishment of the central network of self-promoting pluripotency factors NANOG, OCT4 and SOX2 (Chambers et al., 2009). Given appropriate conditions, these cells can be cultured almost indefinitely, similar to human embryonic stem (hES) cells, while expressing a classical set of pluripotency markers like OCT4, NANOG, SSEA3, SSEA4, TRA-1-60 and TRA-1-81 (Yu et al., 2007). The major benefit of the reprogramming approach over hES cell harvesting is twofold. First, the technique can be performed on easily accessible adult donor cells, e.g. fibroblasts, nucleated blood cells, urinary tract epithelial cells, thus no embryos have to be harvested and the associated ethical issues do not come to bear. Second, iPSC technology can specifically address patients. Thus, early or highly penetrant disorders like developmental defects are well-suited for iPSC-based disease modeling (Peitz et al., 2013, Karagiannis et al., 2019). Yet, even without immediately apparent patient-specific phenotypes, iPSCs provide a high-quality resource for differentiation of target cell populations like neural stem cells (NSCs). Furthermore, the clonogenic potential of iPSCs makes them highly useful for genome editing, with the major risk of promoting aberrant clones, so that clone-based quality control of genomic integrity and pluripotency are required (Shi et al., 2017).

1.4. Long-term self-renewing neuroepithelial-like stem (lt-NES) cells

Neural stem cells are an intermediary step during differentiation from pluripotent stem cells to postmitotic neurons. Long-term self-renewing neuroepithelial-like stem (lt-NES) cells are an NSC population derived from human PSCs that match these characteristics (Falk et al., 2012, Koch et al., 2009). Like other tissue stem cell populations, lt-NES cells offer a range of advantages as a starting platform for terminal differentiation compared to PSCs (Elkabetz et al., 2008). First and foremost, any differentiation time used to establish the lt-NES does not need to be spent again for future terminal differentiations since many lt-NES lines can be expanded, quality controlled and banked. Second, a well-defined lt-NES pool is already lineage restricted and less prone to variability in the final cell population, giving rise to a more standardized outcome (Peitz et al., 2013, Sproul et al., 2014).

Lt-NES are restricted to the three major CNS lineages, i.e. neurons, astrocytes and oligodendrocytes, but strongly prefer neuronal differentiation over the other two. When differentiated, approximately 80 % of the cells become neurons, while 20 % turn into astrocytes. Notably, the differentiation dynamic is temporally controlled. Neurons are born almost exclusively during the first two weeks of differentiation; astrocytes later arise from persisting NSCs. For example, radial glia-like cells ($GFAP^+TUBB3^+$) occur sporadically in seven-weeks-old cultures (Gorris et al., 2015). The resulting cells are dominantly GABAergic and glutamatergic and exhibit a mid-hindbrain border identity as shown by the expression of corresponding HOX genes (Koch et al., 2009). Sporadically, serotonergic and dopaminergic neurons are generated. Lt-NES-derived neurons form synapses and reach functional maturity after 6 weeks *in vitro* differentiation (Koch et al., 2011).

1.5. Genome editing

In the early days of mouse genetics, site-directed transgene insertion was achieved by cloning the gene of interest between large overlapping regions flanking the target site and hoping for random double-strand breaks to induce homologous repair mechanisms. Even though this technique can be optimized by positive (e.g. neomycin resistance) and

negative selection (e.g. thymidine kinase cassette) of candidate clones, the overall efficiency is extremely low (Bouabe et al., 2013). Newer techniques like zinc-finger nucleases (ZFNs), transcription activator-like effector nucleases (TALENs) or CRISPR-Cas9 combine targeted DNA binding domains with nucleases to efficiently induce DNA breaks in a site-specific manner and thus dramatically promote homologous recombination events (Jinek et al., 2013, Joung et al., 2013, Urnov et al., 2010). TALENs derive their binding specificity from an array of modular microdomains, each specific to a particular base triplet (Joung et al., 2013). Thus, a TALEN can be cloned to specifically bind almost any DNA sequence. However, causing double-strand breaks using any of the techniques above carries the risk of random genomic changes. Most importantly, the faster and simpler non-homologous end joining (NHEJ) mechanism can supersede homologous recombination. Also, double-strand breaks are occasionally introduced in unintended, so-called off-target sites (Zhang et al., 2015). Recent developments have therefore turned away from nucleases in favor of "nickases", enzymes that only introduce single-strand breaks (Ran et al., 2013). Two single-strand breaks, positioned close together, have been shown to stimulate homologous recombination similar to a double-strand break, but without the risk of NHEJ mutagenesis (Zhang et al., 2015). On top, using two nickases requires targeting two specific DNA sequences, drastically reducing off-target effects.

1.6. Genomic "safe harbor" sites

Transgene insertion is a commonly used and highly relevant technology for expression of foreign proteins or heightened expression of endogenous proteins in cell culture. In contrast to transient transfection approaches, transgene insertion relies on integrating exogenous DNA sequences into the host genome. Evolutionary, viruses have employed this method with great success, so infection with engineered retro- or lentiviruses can reliably insert a sequence of interest into eukaryotic genomes (Vargas et al., 2016). For the purpose of precision genome engineering, this approach comes with two major hurdles: Insertional mutagenesis and transgene silencing. Insertional mutagenesis occurs when the transgene is inserted into a genomic region that already contains protein-coding or otherwise functionally important sequences. Thus, genes can be

disrupted or altered, leading to phenotypic artifacts from the insertion. Transgene silencing, on the other hand, is a eukaryotic defense mechanism against expression of viral transgenes, an effect that is especially pronounced in iPSCs (Hoffmann et al., 2017, Hotta et al., 2008). Silencing is achieved by blocking transcription from the affected region via methylation of the foreign DNA sequence, leaving an inert stretch that can mutate and e.g. form new genes over evolutionary timeframes. Nonetheless, these defenses pose a problem when strong long-term transgene expression is required. Unsurprisingly, a workaround has evolved in viruses as well, most prominently in adeno-associated virus (AAV). Rare regions in the eukaryotic genome are protected from silencing, so-called "safe harbor" sites (Papapetrou et al., 2016). In humans, the most widely used safe-harbor locus is the adeno-associated virus type 2 integration site 1 (AAVS1) (Qian et al., 2014). AAVS1 is located in the PPP1R12C gene, a regulatory subunit of protein phosphatase 1. Although interference with the locus is generally non-pathogenic, as is non-reproductive AAV2 infection, it is strongly protected from methylation (Nault et al., 2016, Owens, 2002). Thus, specific transgene insertion into AAVS1 yields consistent expression over long time periods, especially during neurodifferentiation (Qian et al., 2014). When starting from iPSCs, transgene integration can be screened for in single clones for highly standardized, homogeneous expression.

1.7. Aim of the thesis

It is a well-established view that the full extent of the human AD pathology and its mechanistic underpinnings are very difficult to study using existing AD animal models or transformed human cells. Thus, new models are needed that reflect the features and progression of AD pathology while remaining as close as possible to authentic human physiology. This project aimed to establish an authentic neural 3D-matrix model of Alzheimer's disease based on non-transformed human neurons. Control iPSCs had to be genetically engineered to inducibly express FAD variants of APP and PS-1 from the AAVS1 genomic safe-harbor locus in order to circumvent expression strength and stability issues reported for vector systems with random integration. Then, a neural stem cell population (lt-NES cells) had to be generated to serve as a standardized platform for neuronal differentiation in three-dimensional gel matrix cultures for extended periods to promote pathogenic Aβ accumulation.

The first major aim of this thesis was to analyze Aβ generation and accumulation in matured cultures, and potential aggregates should be compared to published reports of *in vivo* amyloid deposits. To this end, ELISA analyses, immunolabeling, autofluorescence and amyloid dyes should be tested in the 3D culture setting to determine amyloid properties. Second, to confirm the amyloid cascade hypothesis, the potential presence of p-tau pathology had to be determined, and, if possible, characterized. Neurons had to be analyzed for evidence of increased tau phosphorylation and dyslocalization, as well as dystrophy. Finally, metabolic and viability parameters should be illuminated, e.g. mitochondrial health and neuronal degeneration, both key AD features. As all putative phenotypes are hypothesized to be Aβ-dependent, pharmacological inhibition of Aβ generation should be employed to verify that hypothesis.

2. Materials und Methods

2.1. Antibodies

Primary antibodies

Antibody name	Target	Host	Dilution ICC	Dilution WB	Supplier
6E10	Aβ	ms	1:200	1:500	BioLegend
AT8	p-tau	ms	1:1000	1:500	ThermoFisher
cCas3	cCas3	rb	1:300		CellSignaling
Complex IV	Complex IV	ms			Abcam
D54D2	Aβ	rb	1:1000		CellSignaling
DACH1	DACH1	rb	1:500		Protein Tech
GABA	GABA	rb	1:500		Sigma
GFAP	GFAP	rb	1:1000		Millipore
MC-1	p-tau (aggr.)	ms	1:50		Peter Davies
NESTIN	NESTIN	rb	1:100		Novus Biologicals
Neurofilament	Neurofilament	rb	1:1000		Abcam
PAX6	PAX6	rb	1:50		Covance
PLZF	PLZF	ms	1:500		R&D Systems
SOX2	SOX2	ms	1:100		R&D Systems
SSEA4	SSEA4	ms	1:300		DSHB
TOM20	TOM20	ms	1:2000		Abcam
Total OXPHOS Rodent WB antibody cocktail	CI-NDUFB8 CII-30kDa CIII-Core protein 2 CIV subunit I CV α-subunit	ms			Abcam
TRA-1-81	TRA-1-81	ms	1:500		Millipore
TUJ1	TUBB3	ms	1:1000		Covance
ZO-1	ZO-1	rb	1:100		Invitrogen

Secondary antibodies

Antibody	Dye	Host	Dilution ICC	Dilution WB	Supplier
α-rb IgG	Alexa 488	goat	1:1000	-	Life technologies
α-rb IgG	Alexa 647	goat	1:500	-	Life technologies
α-ms IgG	Alexa 488	goat	1:1000	-	Life technologies
α-ms IgG	Alexa 647	goat	1:500	-	Life technologies
α-rb IgG	HRP	goat	-	1:1000	Cell Signaling
α-ms IgG	HRP	goat	-	1:1000	Cell Signaling

2.2. Chemicals

Chemical	Supplier	Registered Office
2-Mercaptoethanol	Life technologies	Carlsbad, USA
Accutase	Stem cell tech	Cologne, Germany
Acetic acid	Roth	Karlsruhe, Germany
Agar	Roth	Karlsruhe, Germany
Agarose	PEQLAB	Erlangen, Germany
Amaxa nucleofector kit V	Lonza	Santa Clara, USA
Ampicillin	Sigma	Deisenhofen, Germany
Ampuwa (sterile water)	Fresenius	Bad Homburg, Germany
AmyTracker 630	Ebba Biotech	Stockholm, Sweden
B-27 supplement	Life technologies	Carlsbad, USA
Bromphenol blue	Sigma	Deisenhofen, Germany
BSA	Sigma	Deisenhofen, Germany
Congo red	Sigma	Deisenhofen, Germany
DAPT	Axon MedChem	Groeningen, Netherlands
Dispase	Sigma	Deisenhofen, Germany
DMEM high glucose	Life technologies	Carlsbad, USA
DMEM/F12 (1:1)	Life technologies	Carlsbad, USA
DMSO	Sigma	Deisenhofen, Germany
DNA ladder (100bp)	New England Biolabs	Frankfurt, Germany
DNA ladder (1kb)	New England Biolabs	Frankfurt, Germany
DNA loading buffer (10x)	New England Biolabs	Frankfurt, Germany
DNase	CellSystems	St. Katharinen, Germany
Doxycycline hyclate	Sigma	Deisenhofen, Germany
EDTA	Sigma	Deisenhofen, Germany
EGF	R&D Systems	Wiesbaden, Germany
EGTA	Roth	Karlsruhe, Germany
Ethanol	Roth	Karlsruhe, Germany
Ethidium bromide	Sigma	Deisenhofen, Germany
FCS	PAN Biotech	Aidenbach, Germany
FGF2	R&D systems	Wiesbaden, Germany
Geltrex	Thermo Scientific	Waltham, MA, USA
Glucose	Sigma	Deisenhofen, Germany
Glycerol	Roth	Karlsruhe, Germany
Insulin	Sigma	Deisenhofen, Germany
Isopropanol	Roth	Karlsruhe, Germany
Knockout-DMEM	Life technologies	Carlsbad, USA
L755507	Sigma	Deisenhofen, Germany
L-Glutamine	Life technologies	Carlsbad, USA
LAAP	Sigma	Deisenhofen, Germany
Laminin	Sigma	Deisenhofen, Germany

Chemical	Supplier	Registered Office
Methanol	Roth	Karlsruhe, Germany
Methoxy-X04	Cayman Chemical	Hamburg, Germany
$MgCl_2$	Life technologies	Carlsbad, USA
Milk powder (low fat)	Roth	Karlsruhe, Germany
Mowiol	Merck	Darmstadt, Germany
N2 supplement	Thermo scientific	Waltham, MA, USA
$NaHCO_3$	Sigma	Deisenhofen, Germany
Non-essential amino acids	Life technologies	Carlsbad, USA
Neurobasal medium	Life technologies	Carlsbad, USA
Paraformaldehyde	Sigma	Deisenhofen, Germany
PBS	Life technologies	Carlsbad, USA
Poly-ornithine	Sigma	Deisenhofen, Germany
Puromycin	Sigma	Deisenhofen, Germany
RO4929097	Selleckchem	Munich, Germany
Serum replacement	Life technologies	Carlsbad, USA
Sodium azide	Sigma	Deisenhofen, Germany
Sodium chloride	Roth	Karlsruhe, Germany
Sodium deoxycholate	Sigma	Deisenhofen, Germany
Sodium dodecyl sulphate	Roth	Karlsruhe, Germany
Sodium pyruvate	Life technologies	Carlsbad, USA
Sodium selenite	Sigma	Deisenhofen, Germany
StemMACS iPS-Brew XF(Stembrew)	Miltenyi Biotec	Bergisch Gladbach, Germany
Streptomycin	Sigma	Deisenhofen, Germany
TGFβ1	PeproTech	Hamburg, Germany
Thioflavin T	Sigma	Deisenhofen, Germany
Transferrin	Sigma	Deisenhofen, Germany
Tris	Merck	Darmstadt, Germany
Triton-X-100	Sigma	Deisenhofen, Germany
Trypan blue	Life technologies	Carlsbad, USA
Trypsin-EDTA (10x)	Life technologies	Carlsbad, USA
Trypsin inhibitor	Thermo scientific	Waltham, MA, USA
Tryptone	Roth	Karlsruhe, Germany
Tween-20	BIO-RAD	Munich, Germany
Xylene cyanol	Sigma	Deisenhofen, Germany
Yeast extract	Roth	Fürth, Germany

2.3. Equipment

Device	Name	Manufacturer	Registered office
Autoclave	D-150	Systec	Wettenberg, Germany
Balance	LA310S BL610 BP2100S	Sartorius	Goettingen, Germany

Device	Name	Manufacturer	Registered office
Block heater	Thermomixer compact	Eppendorf	Hamburg, Germany
Centrifuges and rotors	Megafuge 1.0R Rotor #2704 Rotor BS4402/A	Heraeus	Hanau, Germany
Centrifuges and rotors	RC 26 PLUS RC5B PLUS Rotor SS-34 Rotor SLA-3000	Sorvall	Newtown, USA
Chemiluminescence detection	ChemiDoc XRS	BIO-RAD	Munich, Germany
Confocal microscope	Olympus IX81 FluoView FV1000	Olympus	Hamburg, Germany
Counting chamber	Fuchs-Rosenthal	Faust	Halle, Germany
FACS	FACSCalibur	BD Biosciences	San Jose, USA
Fluorescence microscope	Axiovert 40 CFL	Carl Zeiss	Jena, Germany
Freezer -80°C	Hera freeze	Heraeus	Hanau, Germany
Freezer -150°C	MDF-C2156VAN-PE	Panasonic	Hamburg, Germany
Gel electrophoresis chamber	Agagel	Biometra	Goettingen, Germany
Gel electrophoresis documentation	GelDoc	BIO-RAD	Munich, Germany
High-content fluorescence microscope	IN Cell Analyzer	GE Healthcare	Munich, Germany
Horizontal hood	Hera guard	Hereaus	Hanau, Germany
Incubator	HERAcell 150 OV3	Heraeus Biometra	Hanau, Germany Goettingen, Germany
Incubator shaker	innova 4300 Innova 44	New Brunswick Scientific	Nuertingen, Germany
Inverse light microscope	Axiovert 40C	Carl Zeiss	Jena, Germany
Liquid nitrogen store	MVE 611 K Series Cryostorage System	Chart Industries Taylor-Wharton	Burnsville, USA Husum, Germany
Live cell imaging microscope	Axiovert 200M Camera: Prog Res C14 UV-lamp: Ebq 100	Zeiss Jenoptik Zeiss	Jena, Germany
Magnetic stirrer		Stuart Scientific	Staffordshire, UK

Device	Name	Manufacturer	Registered office
Microwave	Microwave 800	Severin	Sundern, Germany
Nucleofection	Nucleofector IIb	Lonza	Basel, Switzerland
pH-meter	HI 9321	HANNA Instruments	Kehl am Rhein, Germany
Pipette set	Labmate	Abimed	Langenfeld, Germany
Pipetting aid	Accu-Jet	Brand	Wertheim, Germany
Plate reader	Envision 2104	Perkin-Elmer	Krakow, Poland
Power supply electrophoresis	Standard Power Pack P25	Biometra	Goettingen, Germany
Power supply SDS-PAGE	POWER PAC 200	BIO-RAD	Munich, Germany
Refrigerators/ freezers 4°C, -20°C	G 2013 Comfort HERAfreeze	Liebherr Heraeus	Lindau Hanau, Germany
SDS PAGE chamber	Novex Mini-Cell	Life technologies	Carlsbad, USA
Shaker	Roto Shake Genie	Scientific Industries	New York, USA
Stereo microscope	STEMI 2000-C,	Carl Zeiss	Goettingen, Germany
Sterile laminar flow hood	HERAsafe	Heraeus	Hanau, Germany
Table centrifuges	Centrifuge 5415R BIOFUGE pico Galaxy Mini Spectrafuge Mini	Eppendorf Heraeus VWR Labnet	Hamburg, Germany Hanau, Germany Darmstadt, Germany Berkshire, UK
Thermocycler	T3 Thermocycler	Biometra	Goettingen, Germany
Ultracentrifuge	Discovery 90SE Sarespin 630	Sorvall	Newtown, USA
UV table	Syngene GVM 20	Synoptics LTD	Cambridge, UK
Vacuum pump	Vacuubrand PC2004 Vario	Brand	Wertheim, Germany
Vortexer	Vortex Genie 2	Scientific Industries	New York, USA
Waterbath	WB14	Memmert	Schwabach, Germany
Western blot chamber	Mini-PROTEAN 3 Cell	BIO-RAD	Munich, Germany

2.4. Molecular biology reagents

Bacteria

Strain	Usage
E. coli DH5α	Plasmid amplification
E. coli OneShot TOP10	Plasmid amplification

LB medium

Component	Concentration
H_2O	
Tryptone	10 g/l
Yeast extract	5 g/l
NaCl	5 g/l
Procedure: Autoclave and store at 4°C	

LB Agar

Component	Concentration
H_2O	
Tryptone	10 g/l
Yeast extract	5 g/l
NaCl	5 g/l
Agar	10 g/l
Procedure: Autoclave and store at 4°C	

Plasmid preparation

Application	Manufacturer	Registered office
Plasmid Maxi Prep	Macherey-Nagel	Düren, Germany
PureLink Quick Plasmid Mini	Life technologies	Carlsbad, USA

Restriction enzymes

Enzyme	Manufacturer	Registered office
Restriction endonucleases	New England Biolabs	Frankfurt, Germany
Benzonase	Novagen	Darmstadt, Germany

Agarose gel loading dye

Component	Concentration
H_2O	50 %
Glycerol	50 %
Bromophenol blue	1:200
Xylene cyanol	1:200
Storage: 1 year at 4°C	

TAE buffer

Component	Concentration
H_2O	
Tris base	4.85 g/l
Glacial acetic acid	1.15 ml/l
EDTA	1 mM
Storage: 14 days at room temperature	

RIPA base buffer

Component	Concentration
H_2O	
Triton X-100	1 %
Na-deoxycholate	0.5 %
Tris (pH 8)	10 mM
Benzonase	1 %
Storage: 1 year at -20°C; add Benzonase fresh	

RIPA supplement (10x)

Component	Concentration
H_2O	
SDS	20 %
EDTA	50 mM
EGTA	10 mM
Storage: 1 year at -20°C	

TBS-Tween

Component	Concentration
H_2O	
Tris (pH 7.5)	20 mM
NaCl	150 mM
Tween-20	0.1 %
Storage: 3 months at room temperature	

Western transfer buffer

Component	Concentration
H_2O	
Tris base	25 mM
Glycerol	150 mM
Methanol	15 %
Storage: 3 months at 4°C	

Western blocking buffer

Component	Concentration
TBS-T	
Low-fat milk powder	10 %
Storage: Prepare fresh; filter through cell strainer before use	

Western phospho-protein blocking buffer

Component	Concentration
TBS-T	
BSA	5 %
Storage: Prepare fresh; filter through cell strainer before use	

Antibody buffer

Component	Concentration
TBS-T	
Low-fat milk powder	5 %
Storage: Prepare fresh; filter through cell strainer before use	

Detection reagents

Reagent	Manufacturer	Registered office
Luminata Classico Western HRP Substrate	Millipore	Schwalbach, Germany
Luminata Crescendo Western HRP Substrate	Millipore	Schwalbach, Germany
SuperSignal West Femto Maximum Sensitivity Substrate	Thermo Scientific	Waltham, MA, USA

2.5. Primers

Primers were designed using either the primer3 or NEBuilder web applications. Upon arrival, lyophylized primers were reconstituted to 100 μM in H_2O. Unless noted otherwise, PCRs were run with a final primer concentration of 130 nM.

Primer name	Sequence [annealing bases capitalized]
APOE seq fwd	ACTGACCCCGGTGGCGGAGGA
APOE seq rv	CAGGCGTATCTGCTGGGCCTGCTC
AAVS1 site wt seq fwd	TGCTTTCTTTGCCTGGACAC
AAVS1 site wt seq rv	CACCAGGATCAGTGAAACGC
imAP insert fwd	tcctaccctcgtaaagATGCTGCCCGGTTTGGCA
imAP insert rv	caggctagccatatgaCTACTTGTACAGCTCGTCCATGCC
im insert fwd	tcctaccctcgtaaagCCGCCCCTCTCCCTCCCC
im insert rv	caggctagccatatgaTTACTTGTACAGCTCGTCCATGCCG
AAVS1 ins val fwd	ACCAACGCCGACGGTATCAG
AAVS1 ins val rv	CAGACCCTTGCCCTGGTGGT
AAVS1 3' ins val fwd	TACCACCGATTCTATGCCCC
AAVS1 3' ins val rv	AGGATGCAGGACGAGAAACA
imAP lig val fwd	ACCAACTTTCCGTACCACTTC
imAP lig val rv	GCAGGCCAGCATTACCATC
im lig val fwd	GGGCCATTTACCGTAAGTTATGT
im lig val rv	GATGAACTCGCCGTCTTGC

2.6. Software

Purpose	Name	Company / Maintainer	Office
Image processing	Adobe Photoshop CS6	Adobe Systems	Berkeley, USA
	FIJI	Wayne Rasband	
	Grid stitching plugin	Stephan Preibisch	
	NeuronJ plugin	Erik Meijering	
	AxioVision	Carl Zeiss	Jena, Germany
	Olympus Fluoview	Olympus Corporation	Hamburg, Germany
	IN Cell Analyzer	GE Healthcare	Freiburg, Germany

Primer design	primer3	http://primer3.ut.ee/	
	IDT OligoAnalyzer	http://eu.idtdna.com/calc/analyzer	
	RNAfold	http://rna.tbi.univie.ac.at/cgi-bin/RNAWebSuite/RNAfold.cgi	
	NEBuilder	http://nebuilder.neb.com/	
DNA cloning	SerialCloner	Serial Basics	
DNA sequencing	SerialCloner	Serial Basics	
	ApE	U. of Utah, Wayne Davis	Salt Lake City, USA
SNP analysis	Genome Studio	Illumina Inc.	San Diego, USA
Blot documentation	QuantityOne	Bio-Rad	Munich, Germany
Blot quantification	FIJI	Wayne Rasband	
Gel documentation	QuantityOne	Bio-Rad	Munich, Germany
Spectroscopy	NanoDrop 2000 / 2000c	ThermoFisher	Waltham, USA
Figure design	Adobe Illustrator CS6	Adobe Systems	Berkeley, USA
Text processing	Microsoft Word	Microsoft Corporation	Redmond, USA
Table processing	Microsoft Excel	Microsoft Corporation	Redmond, USA
Reference library	Mendeley	Elsevier	Amsterdam, Netherlands
Statistical analysis	R / RStudio	The R project	
Plotting	R / RStudio	The R project	

2.7. Plastic consumables

Consumable	Manufacturer	Registered office
Cellsieve Cell Strainer 40 µm	BD Biosciences	Heidelberg, Germany
Centrifuge tubes	Beckman	Krefeld, Germany
Cryovials 1 ml / 2 ml	Nunc	Wiesbaden, Germany
Millicell culture inserts 24-well 0.4 µm	Millipore	Schwalbach, Germany
Novex Sharp Prestained Protein Standards	Life technologies	Carlsbad, USA
NuPAGE 3-8 % Tris-Acetate gel	Life technologies	Carlsbad, USA
NuPAGE 4-12 % Bis-Tris gel	Life technologies	Carlsbad, USA
PCR Softtubes (0,2 ml)	Biozym Scientific	Oldendorf, Germany
Petri dishes	BD Biosciences	Heidelberg, Germany
PVDF membranes	BIO-RAD	Munich, Germany

Seahorse XF24 culture plate	Agilent	Santa Clara, USA
Serological pipettes	BD Biosciences	Heidelberg, Germany
Stericup filtration unit	Millipore	Schwalbach, Germany
Syringe filter 0.2 µm	PALL	Dreieich, Germany
Syringe filter 0.45 µm	Whatman Schleicher & Schuell	Dassel, Germany
Syringes	BD Biosciences	Heidelberg, Germany
Tissue Culture dishes	Nunc	Wiesbaden, Germany
µClear F-bottom 96-well	Greiner	Monroe, USA

2.8. Cell culture reagents

Glucose stock solution (100x)

Component	Concentration
DMEM/F12	
Glucose	16 g/l

PBS-EDTA

Component	Concentration
D-PBS	
EDTA	0.5 mM

Trypsin

Component	Concentration
D-PBS	90 %
10x Trypsin-EDTA stock	10 %

Geltrex

Component	Concentration
DMEM/F12	
Geltrex	1:90 / 1:30
Incubation: >60 min at room temperature	

5 ml Geltrex stock vials were thawed on ice at 4°C overnight and aliquoted in 200 µl or 600 µl portions in 2 ml cryotubes. The aliquots were stored at -20°C.

To coat plastic dishes and multi-well plates for iPSC cultivation, frozen aliquots were resuspended 1:90 in ice-cold DMEM/F12 medium. Appropriate volumes of the coating solution were distributed onto the dish / plate and incubated at room temperature for at least 30 min. For 2D neural differentiation, Geltrex was diluted 1:30 and the minimum incubation time extended to 1 h. Incubated plates can be used immediately or stored at 4°C for up to two weeks.

Poly-L-ornithine

Component	Concentration
ddH$_2$O	
Poly-L-ornithine	15 µg/ml
Incubation: >60 min at 37°C followed by 2x PBS wash	

Laminin

Component	Concentration
D-PBS	
Laminin	2 µg/ml
Incubation: >60 min at 37°C or over night at 4°C	

E8 base medium

Component	Concentration
DMEM/F12 w/ HEPES	
LAAP	64 µg/ml
Transferrin	10 µg/ml
Na-selenite	14 ng/ml
Insulin	20 µg/ml
Storage: 14 days at 4°C	

E8 medium

Component	Concentration
E8 base medium	
TGF-β1	2 ng/ml
bFGF	100 ng/ml
Storage: 3 days at 4°C	

Stembrew medium

Component	Concentration
StemMACS iPS-Brew XF basal medium	
StemMACS iPS-Brew XF 50x Supplement	1:50
Storage: 14 days at 4°C	

iPSC freezing medium

Component	Concentration
Serum replacement	90 %
DMSO	10 %
Storage: Prepare fresh for freezing; cool to 4°C	

N2 medium

Component	Concentration
DMEM/F12	
N2 supplement	1:100
Glucose stock solution (100x)	1:100
Storage: 14 days at 4°C	

Lt-NES medium

Component	Concentration
N2 medium	
FGF	10 ng/ml
EGF	10 ng/ml
B27	1:1000
Storage: 3 days at 4°C	

Lt-NES freezing medium

Component	Concentration
KO Serum replacement	65 %
N2 medium	25 %
DMSO	10 %
Storage: Prepare fresh for freezing; cool to 4°C	

NGMC

Component	Concentration
N2 medium	50 %
Neurobasal medium	50 %
Glutamine	1 mM
B27	1:50
Storage: 30 days at 4°C	

Antibiotics

Antibiotic	Stock concentration	Solvent
Ampicillin	100 mg/ml	H_2O
Doxycycline	2 mg/ml	H_2O
Puromycin	1 mg/ml	H_2O
Storage: 6 months at -20°C		

2.9. Vector cloning

2.9.1. Generation of construct fragments

Construct fragments were designed *in silico* using the Serial Cloner software suite based on the RefSeq human reference genome sequences. To design and optimize primers for Gibson assembly, we utilized the NEBuilder tool followed by separate validation in IDT OligoAnalyzer and RNAfold (ssDNA parameters, university of Vienna). Primer designs were excluded in cases of substantial heterodimerization tendency or hairpin formation. To standardize primer pipetting, a "primer mix" was prepared in advance containing all primers for the respective reaction at 3.3 µM in H_2O.

PCR protocol

Step	Temperature	Time	Repeat	ΔT
1	98°C	300 s		
2	98°C	30 s		
3	65°C	30 s		
4	72°C	300 s	Go to 2 x5	-1°C
5	98°C	30 s		
6	58°C	30 s		
7	72°C	300 s	Go to 5 x40	
8	4°C	pause		

2.9.2. imAP construct

The imAP construct was generated via amplification of the APPswe/lon-PS1dE9-mCherry cassette from the lentiviral mAP construct (kind gift by Doo Yeon Kim) followed by Gibson assembly into the doxycycline-inducible AAVS1 targeting vector (kind gift by Su-Chun Zhang). Primer set: "imAP insert fwd" + "imAP insert rv". DMSO was included as described in the experiment.

Component	Concentration	Volume [25 µl reaction]
H_2O		15 µl (ad 25)
Phusion GC buffer	5x	5 µl
dNTPs	100 mM	2.5 µl
DMSO	100 %	0.75 / 1.5 / 2.25 µl
Template	100 ng/µl	1 µl
Primer mix	3.3 µM	1 µl
Phusion polymerase		0.25 µl

2.9.3. Component preparation

For plasmid assembly, PCR products of the respective insert cassettes were purified by agarose gel electrophoresis on a 1 % gel in TAE buffer with ethidium bromide after 45 min separation at 100 V. The plasmid backbone was acquired by treating the AAVS1-GFP plasmid with MluI and SalI restriction enzymes (according to manufacturer's instructions) to remove the GFP open reading frame. Then, the backbone was purified by electrophoresis. Separated bands of interest were cut from the gel and purified using a QiaQuick gel extraction kit.

2.9.4. Gibson assembly

Purified plasmid components were mixed with the HiFi DNA assembly Master Mix kit according to the manual and incubated for 1 h at 50°C.

2.9.5. Bacterial transformation and culture

For all bacterial transformation experiments, we used OneShot TOP10 chemically competent bacteria. After thawing on ice for 15 min, plasmid / assembly mix was added with careful stirring at <10 % of total bacteria volume and left to incubate for 30 min on ice. Then, a 45 s, 42°C heat shock was applied by suspending the tube in a waterbath. Next, bacteria were supplemented with 300 µl LB medium at room temperature and incubated on a shaker at 37°C for 1 h. Finally, the bacterial suspensions were either spread out on agar-amp plates or transferred to 5 ml / 200 ml flasks in LB medium with ampicillin for incubation over night at 37°C.

Colonies that formed on plates were marked, transferred to a grid slot of a new agar-amp plate for safekeeping at 4°C and used to inoculate a 5 ml LB tube for mini preparation.

2.9.6. Plasmid purification

Plasmids were purified from bacteria via the Macherey-Nagel Mini and Maxi preparation kits according to the manufacturer's instructions.

2.9.7. Plasmid validation

Serial cloner's "virtual digest" function predicts a specific band pattern based on an input sequence and selected restriction enzymes that can be easily compared to the results of agarose gel electrophoresis. The imAP plasmid could be validated by restriction analysis with AseI. Expected band sizes are 4.5 kb, 3.1 kb, 2.3 kb, 2 kb, 1.5 kb and 60 bp.

2.10. Cell culture

2.10.1. iPSC cultivation

iPSCs were cultured in StemMACS iPS-Brew XF (Stembrew) medium on Geltrex-coated dishes (1:90) in a 37°C incubator at 5 % CO_2. The cells grew as colonies and were allowed to grow until close to confluency with medium replacement every other day. Then, the supernatant was replaced with PBS-EDTA for ca. 4 min or until iPSC colonies exhibited visible "cracking". Careful removal of the PBS-EDTA and vigorous washing with Stembrew resuspended small colonies that were transferred to a fresh Geltrex-coated plate. The splitting ratio is flexible from 1:1 to 1:6 depending on required cell numbers and densities.

iPSCs can be frozen by resuspending EDTA-dislodged cultures in iPSC freezing medium at 4°C and transferring the suspension into cryo tubes. After freezing at -80°C over night, cell stocks were transferred to -150°C for long-term storage.

To thaw, iPSC stocks were liquefied in a 37°C water bath until minimal ice remained. Then, the complete stock was resuspended in room temperature Stembrew medium, transferred to a centrifugation tube and pelleted at 800 g for 3 min. Supernatants were discarded, while the cell pellet was resuspended in Stembrew with 10 µM ROCK inhibitor. The suspension was then seeded onto Geltrex-coated plates. 24 h later, medium was replaced with Stembrew.

2.10.2. DNA extraction, genotyping and sequencing

For sequencing and SNP analysis, ca. 1×10^6 cell were collected after thawing, then pelleted at 5,000 g for 2 min. DNA was extracted using the QiaQuick blood and tissue kit according to the manufacturer's instructions.

For PCR genotyping, puromycin resistant colonies were picked from primary plates under a horizontal flow hood. Ca. 200 – 500 cells were transferred to a prepared PCR tube containing 30 µl of QuickExtract reagent. Afterwards, the PCR tubes were incubated at 65°C for 15 min and inactivated at 98°C for 8 min in a thermo cycler. The resulting lysate could be used immediately as PCR template.

2.10.3.   SNP analysis

Purified DNA was supplied to the Institute of Human Genetics, University of Bonn, for chip-based analysis. Datasets were then evaluated using the Illumina Genome Studio software. All graphs show the logR ratio and b-allele frequency for each chromosome.

2.10.4.   Differentation of iPSCs to lt-NES cells

Lt-NES cells were derived according to the protocol in Roese-Koerner et al., 2016. Briefly, iPSC spheres were patterned towards a neuroectodermal fate using LDN (500 nM) and SB431542 (5 µM) for six days. Next, spheres were plated on PO/fibronectin-coated dishes with FGF for one week. Neural rosettes were dislodged using dispase and seeded on PO/ln-coated dishes.

2.10.5.   Lt-NES cell cultivation

Lt-NES cells were maintained at 37°C and 5 % CO_2. To split, lt-NES medium was replaced with trypsin solution and incubated for 5 min at room temperature. Trypsin inhibitor was used to stop the reaction. Then, cells were rinsed off the dish, pelleted at 800 g for 3 min and resuspended in lt-NES medium to be seeded on a new PO/Ln-coated dish.

Confluent lt-NES cultures could be frozen by resuspending the cell pellet (as described above) in ice-cold freezing medium for storage at either -80°C or -150°C. Thawing was achieved in a 37°C water bath until the medium started to liquefy. Room temperature N2 medium was used to melt the remaining ice. The cells were then pelleted by centrifugation at 800 g for 3 min and resuspended in warm lt-NES medium and seeded onto a PO/ln-coated dish.

2.11. Differentiation of lt-NES cells

2.11.1. 2D cultures

2D differentiation was achieved by distributing $4x10^6$ lt-NES cells on a Geltrex-coated (1:30) 3.5 cm dish (ca. 10 cm^2) as described above. Two days after splitting, lt-NES medium was replaced with NGMC, followed by medium replacement every other day for the remaining culture period. Compounds like doxycycline or DAPT were added to the medium prior to replacement.

2.11.2. 3D matrix cultures

The 3D differentiation protocols were adapted from (Kim et al., 2015). For the gel matrix, Geltrex was thawed on ice and mixed with ice-cold lt-NES medium. Lt-NES cells were dislodged as described above, counted, and an appropriate number for the 3D culture was pelleted at 800 g for 3 min. After removal of the supernatant, the pellets were briefly cooled on ice and resuspended in the ice-cold Geltrex-medium mixture, followed by immediate transfer into the plate(s)/well(s). Thin-layer cultures were generated by embedding $2x10^5$ lt-NES cells per well of a 96-well in 100 µl of a 10 % Geltrex in lt-NES medium suspension. For thick-layer cultures, $4x10^6$ lt-NES cells per 24-well transwell insert were embedded in 200 µl of a 50 % Geltrex in lt-NES medium suspension. After one hour at 37°C, the wells could be filled up with lt-NES medium that was later replaced with NGMC on day 2. From then on, medium was replaced every other day. Compounds like doxycycline (1 µg / ml unless stated otherwise) or DAPT (10 µM) were added to the medium prior to replacement.

2.12.   Generation and validation of targeted iPSC lines

2.12.1.   Nucleofection of iPSCs

Nucleofection mix

Component	Concentration
Amaxa nucleofection buffer	82 %
Amaxa nucleofection supplement	18 %
TALEN L	0.5 µg / 100 µl
TALEN R	0.5 µg / 100 µl
Donor plasmid	4 µg / 100 µl

iPSCs were nucleofected using the Amaxa cell line kit V. Cultures were prepared by addition of 10 µM ROCK inhibitor 1 h before dislodgement by PBS-EDTA as described in above. Centrifugation of $3\text{-}4\times10^6$ cells at 800 g for 3 min enabled complete supernatant removal. The pellet was then resuspended in 100 µl of nucleofection mix, transferred into a nucleofection cuvette and nucleofected using program B-023. Afterwards, the cell suspension was collected from the cuvette and distributed on a Geltrex-coated (1:90) 10 cm dish with Stembrew + 10 µM ROCK inhibitor + 5 µM L755507.

During the first 72 h, medium was replaced daily with Stembrew + 10 µM ROCK inhibitor. Next, 0.3 µg/ml puromycin was added during daily medium changes for 5-14 days, depending on the fraction of resistant cells. Upon formation of colonies containing ca. 300-1000 cells, colonies were partially picked. One half of a colony was transferred to a Geltrex-coated (1:90) 96-well plate, the other half was used for genotyping as described in above. Picked colonies were expanded to 6-well plates, SNP validated and cryopreserved for future use.

2.12.2.   Genotyping PCR

Transgene integration was validated by multiplex PCR in the AAVS1 locus. We designed a primer triplet for amplification of the wild-type AAVS1 sequence and / or part of the puromycin-resistance gene together with part of the AAVS1 locus. PCR products

were separated on a 1 % agarose gel. Expected band sizes are 1.8 kb for wild-type alleles and 2 kb for inserted alleles.

AAVS1 genotyping primer mix

Component	Concentration
H_2O	
AAVS1 ins val fwd	10 µM
AAVS1 ins val rv	5 µM
AAVS1 wt seq rv	5 µM
Storage: Store at -20°C	

AAVS1 genotyping PCR mix

Component	Concentration	Volume [25 µl reaction]
H_2O		9 µl (ad 25)
Q5 buffer	5x	5 µl
dNTPs	100 mM	2.5 µl
Q5 GC enhancer	5x	5 µl
Template (colony lysate)		2 µl
Primer mix	See above	1 µl
Q5 polymerase		0.25 µl

AAVS1 genotyping PCR protocol

Step	Temperature	Time	Repeat	ΔT
1	98°C	300 s		
2	98°C	30 s		
3	65°C	30 s		
4	72°C	120 s	Go to 2 x5	-1°C
5	98°C	30 s		
6	58°C	30 s		
7	72°C	120 s	Go to 5 x40	
8	4°C	pause		

2.13. Immuncytochemistry

2.13.1. General staining protocol

IHC blocking solution

Component	Concentration
D-PBS	
Triton X-100	0.1 %
FCS	10 %
Na-azide	0.001 %

Cultures were fixed by medium removal followed by incubation with 4 % PFA over night at room temperature. After washing 3x 5 min with PBS, IHC blocking solution was applied for 1 h at room temperature. Primary antibodies were incubated in IHC blocking solution over night at 4°C, then cultures were washed 3x 5 min with PBS. Next, secondary antibodies were incubated in IHC blocking solution for 1 h at room temperature followed by 3x 5 min PBS wash. Where indicated, cultures were also stained with DAPI for 1 min at room temperature and washed 3x 5 min with PBS. Cultures were stored in PBS with 0.001 % Na-azide.

Thick-layer cultures were stained analogously, however, primary and secondary antibody incubation was extended to over night at 4°C.

2.13.2. Amyloid dyes

AmyTracker 630

AmyTracker 630 working solution was prepared according to the manufacturers instructions by diluting the dye stock 1:100 in PBS. Fixed cultures were incubated with the solution for 30 min at room temperature, followed by three 5 min washes with PBS.

Alcoholic salt solution

Component	Concentration
Ethanol	80 %
H_2O	20 %
NaCl	saturated
Preparation: Add NaCl while stirring until undissolved salt accumulates, leave solution for 24 h prior to use; salt sediment should remain.	

Congo red stock solution

Component	Concentration
Alcoholic salt solution	
Congo red	1 % (w/v)
Preparation: Congo red does not fully dissolve. Allow settling for 24 h prior to use.	

Alkaline alcohol solution

Component	Concentration
Alcoholic salt solution	
1 % NaOH solution	1 % (v/v)

Congo red working solution

Component	Concentration
Congo red stock solution	
1 % NaOH solution	1 % (v/v)
Preparation: Sterile filter immediately prior to use.	

Amyloid aggregates were stained with Congo red by incubation of PFA-fixed thin-layer cultures with alkaline alcohol solution for 20 min and then with Congo red working solution for 20 min. Excessive Congo red was removed by five rinses with PBS.

Methoxy-X04 100x stock solution

Component	Concentration
H_2O	25 %
Ethanol	25 %
DMSO	50 %
Methoxy-X04	1.5 mM

Methoxy-X04 working solution

Component	Concentration
H_2O	50 %
Ethanol	50 %
Methoxy-X04 100x stock solution	1 %
Preparation: Sterile filter immediately prior to use.	

Methoxy-X04 was incubated with PFA-fixed thin-layer cultures for 30 min at room temperature, and then rinsed twice with 80 % ethanol in H_2O and five times with PBS.

Thioflavin T 1000x stock solution

Component	Concentration
D-PBS	
Thioflavin T	5 mM (15.9 mg in 10 ml)

Thioflavin T 1000x stock solution was prepared by dissolving 15.9 mg of Thioflavin T powder in 10 ml of D-PBS. The solution was filtered through a 0.2 µm sterile filter before storage in the dark at 4°C and before each use, respectively. Thioflavin T solutions were prepared fresh whenever visible precipitation occurred.

Thioflavin T working solution

Component	Concentration
D-PBS	
Thioflavin T 1000x stock solution	1:1000
Preparation: Sterile filter immediately prior to use.	

To stain amyloid fibers (both in Aβ aggregates and in neurofibrillary tangles), fixed samples were incubated with Thioflavin T working solution for 8 min at room temperature and then washed twice for 3 min with 50 % ethanol in distilled water and once for 5 min in PBS.

2.14.   Protein analysis

2.14.1.   ELISA

Supernatant samples for ELISA were collected from differentiated 2D imAP cultures after 4 – 8 weeks of treatment. The crude lysates were cleared by filtration through a 0.4 µm sterile filter unit and subjected to ELISA analysis using the "Human β Amyloid (1-40) ELISA Kit Wako II" and "Human β Amyloid (1-42) ELISA Kit Wako, High Sensitive" according to the manufacturer's instructions. The induced supernatants were diluted 1:10 and 1:100, respectively, prior to measurement. Clara Grezella performed the ELISA analyses.

2.14.2.   Protein extraction

Proteins for western blot analysis were extracted by Kevin J. Washicosky according to the protocol from Kim and colleagues (Kim et al., 2015).

2.14.3.   Western blot

Western blot analysis was performed by Kevin J. Washicosky according to the protocol from Kim and colleagues (Kim et al., 2015).

2.14.4.   SDD-AGE

SDD-AGE was performed by Lea Flitsch as described in (Schoch et al., 2016). The resulting membrane was blocked by incubation in 5 % BSA in TBS-T at room temperature. Then, primary antibodies were incubated in TBS-T overnight at 4°C. After washing 3x 5 min in TBS-T, secondary antibodies were incubated in TBS-T for 1 h at room temperature. After 3x 5 min washing in TBS-T, the membrane was rinsed with H_2O. Chemiluminescence detection was performed using the Classico detection kit in the ChemiDoc XRS+ system.

2.15. Microscopy

2.15.1. Lightsheet microscopy

Thick-layer cultures were prepared by over night fixation in 4 % PFA at room temperature and then subjected to a modified immunofluorescence staining protocol starting from blocking and permeabilization for 24 h. Primary and secondary antibody incubations were extended to 48 h each, with five 1 h washing steps in between. Stained samples were cleared as described before and subjected to light-sheet microscopy (Schwarz et al., 2015).

2.15.2. Area fluorescence measurement

Area fluorescence was determined from the combined pixel intensities of stitched images covering a complete well of a 96-well plate (IN Cell Analyzer, 4x4 grid, 10x objective, no deconvolution). Images were non-overlapping and not adjusted for brightness during stitching. Stitching was done using the Grid / Collection stitching plugin for ImageJ / FIJI (Preibisch et al., 2009).

2.15.3. Neurite tracing

Neurites were traced using the ImageJ / FIJI plugin NeuronJ (Meijering et al., 2004) in single-plane confocal images. Image locations were chosen semi-randomly inside the gel matrix. Only AT8+ cell process segments were traced.

2.15.4. Structure and particle quantification

All particle quantifications were performed based on single-plane confocal images. Image locations were chosen semi-randomly inside the gel matrix. Particles were counted manually.

2.16. Mitochondria assays

2.16.1. Mitochondrial length measurement

Thin-layer 3D cultures were immunolabeled with antibodies against neurofilament (heavy chain), p-tau (AT8) and mitochondria (TOM20). Using confocal z-stacks, single cells were identified and three-dimensionally masked based on the somatic segment of the neurofilament staining. Using this mask, the intracellular mitochondrial network was reconstructed as a three-dimensionally branching tube network. The mitochondrial length is the longest non-branching and non-crossing path that can be traced across each network. Mitochondrial length analysis was performed by Fabio Bertan.

2.16.2. Seahorse measurement

Thin-layer cultures could be set up in Seahorse XF 24-well plates using the standard 96-well protocol. Seahorse measurements were performed after 8 weeks of differentiation in total and 6 weeks of treatment, respectively. Before measurement, the cells were equilibrated to atmospheric CO_2 for 1 h at 37°C in NGMC. Dr. Antonia Piazzesi performed the analysis according to the manufacturer's instructions.

2.17. Statistical analysis

Statistical analysis was done either in the R software (ANOVA, Kruskal-Wallis, Shapiro-Wilk), Graphpad prism (ANOVA) or Microsoft Excel (Student's t-test). Prior to testing, normal distribution of the data was determined using the Shapiro-Wilk test in R. ANOVA indicates a one-way ANOVA with Tukey's post-hoc test. Kruskal-Wallis was employed for non-parametric analysis of non-normally distributed measurements in conjunction with Nemenyi's post-hoc test. Student's t-test was used for hypothesis-driven (i.e. one-tailed) comparisons of unpaired samples unless stated otherwise.

3. Results
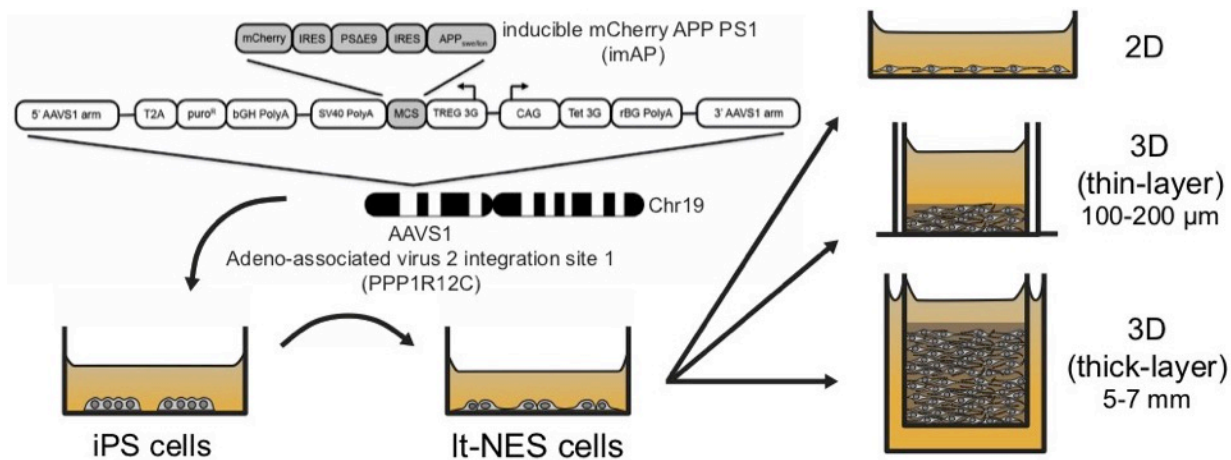
Figure 3.1 3D matrices as a test bed for amyloid deposition in human neural cultures
The inducible AD transgene cassette (imAP) was inserted into human induced pluripotent stem cells (iPSCs) using TALEN-induced homologous recombination. imAP iPSCs were validated and differentiated into neural stem cells (lt-NES), which can be differentiated to neural cultures after embedding in Geltrex matrices. Three dimensional cultivation is expected to promote AD-related phenotypes due to Aβ entrapment. 2D cultures serve as controls. Thin-layer cultures are used for immunofluorescence analysis. Thick-layer 3D cultures provide larger amounts of protein or RNA for biochemical analyses.

This thesis aimed to establish an *in vitro* model system of Alzheimer's disease that recapitulates the major hallmarks of AD in non-transformed human neurons. To this end, induced pluripotent stem cells from a healthy subject were genetically modified by precision genome engineering to inducibly overexpress APP with the Swedish and London mutations (APP$_{Swe/Lon}$) as well as Presenilin-1 without exon 9 (PS-1ΔE9) (Fig. 3.1) (Choi et al., 2014). The transgene cassette consisting of APP$_{Swe/Lon}$, PS-1 ΔE9 and an mCherry reporter connected by IRES sequences (kindly provided by Dr. Doo Yeon Kim, Harvard Medical School) was cloned into a targeting plasmid for the human AAVS1 safe-harbor locus on chromosome 19 (vector backbone kindly provided by Dr. Su-Chun Zhang, University of Wisconsin, Qian et al., 2014). The plasmid contains a puromycin selection cassette and the Tet-On transactivator system to provide an all-in-one donor vector for single-step targeting. Puromycin-resistant clones were validated by PCR genotyping of the AAVS1 locus, pluripotency marker expression analysis and SNP analysis. Validated clones were differentiated into lt-NES cells to provide a stable intermediary population for standardized neural differentiation and then subjected to either 2D, thin-layer or thick-layer 3D culture conditions for further experiments (Kim et al., 2015, Koch et al., 2009).

3.1. Cloning and validation of gene targeting vectors
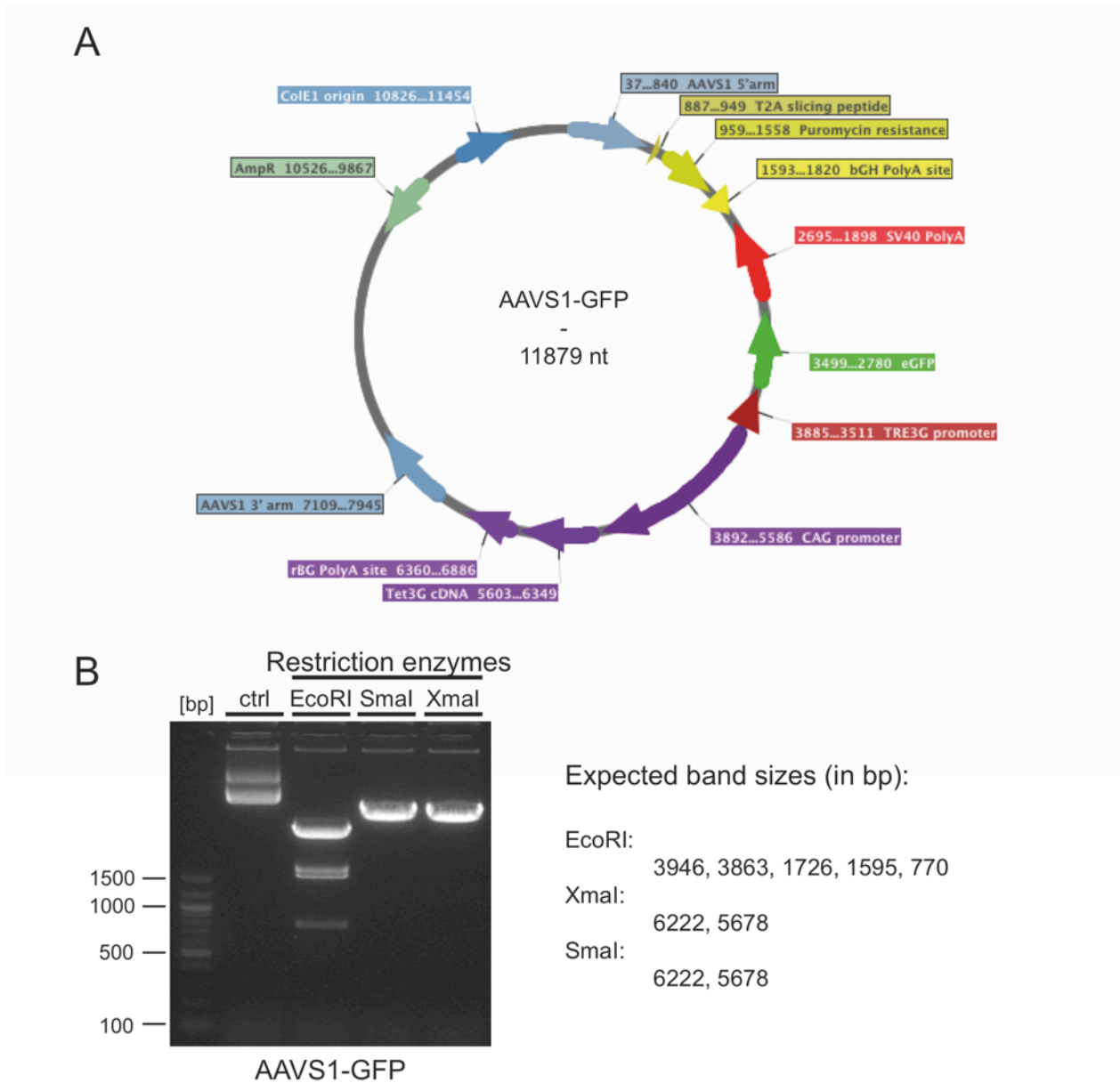
Figure 3.2 AAVS1-GFP plasmid
The AAVS1-GFP plasmid provides the backbone for further cloning. (**A**) The plasmid encodes all relevant components for targeting to the AAVS1 safe-harbor locus, puromycin resistance of correctly integrated cells and the complete Tet-On transactivator system. (**B**) Restriction validation of AAVS1-GFP with EcoRI, SmaI and XmaI enzymes. Uncut plasmid served as control.

Transgene insertion in human cells is a well-established technology. However, long-term expression of transgenes often leads to silencing that can be avoided by targeting the transgene into a safe harbor location (Papapetrou et al., 2016). The AAVS1-GFP targeting plasmid contains three major elements (Fig. 3.2 A). First, it enables puromycin selection of targeted cells by inserting a puromycin resistance cassette into the

PPP1R12C ORF (aka AAVS1). Second, the 3rd generation Tet-On transactivator system and third, a multiple cloning site under a Tet-dependent promoter.

The vector identity was validated by restriction analysis with EcoRI (quintuple cutter), SmaI and XmaI (both double cutters) after preparation of the working stock. All reactions yielded the expected band patterns based on *in silico* predictions, whereas the plasmid-only control showed the typical pattern of a plasmid in relaxed, coiled and supercoiled configuration (Fig. 3.2 B).
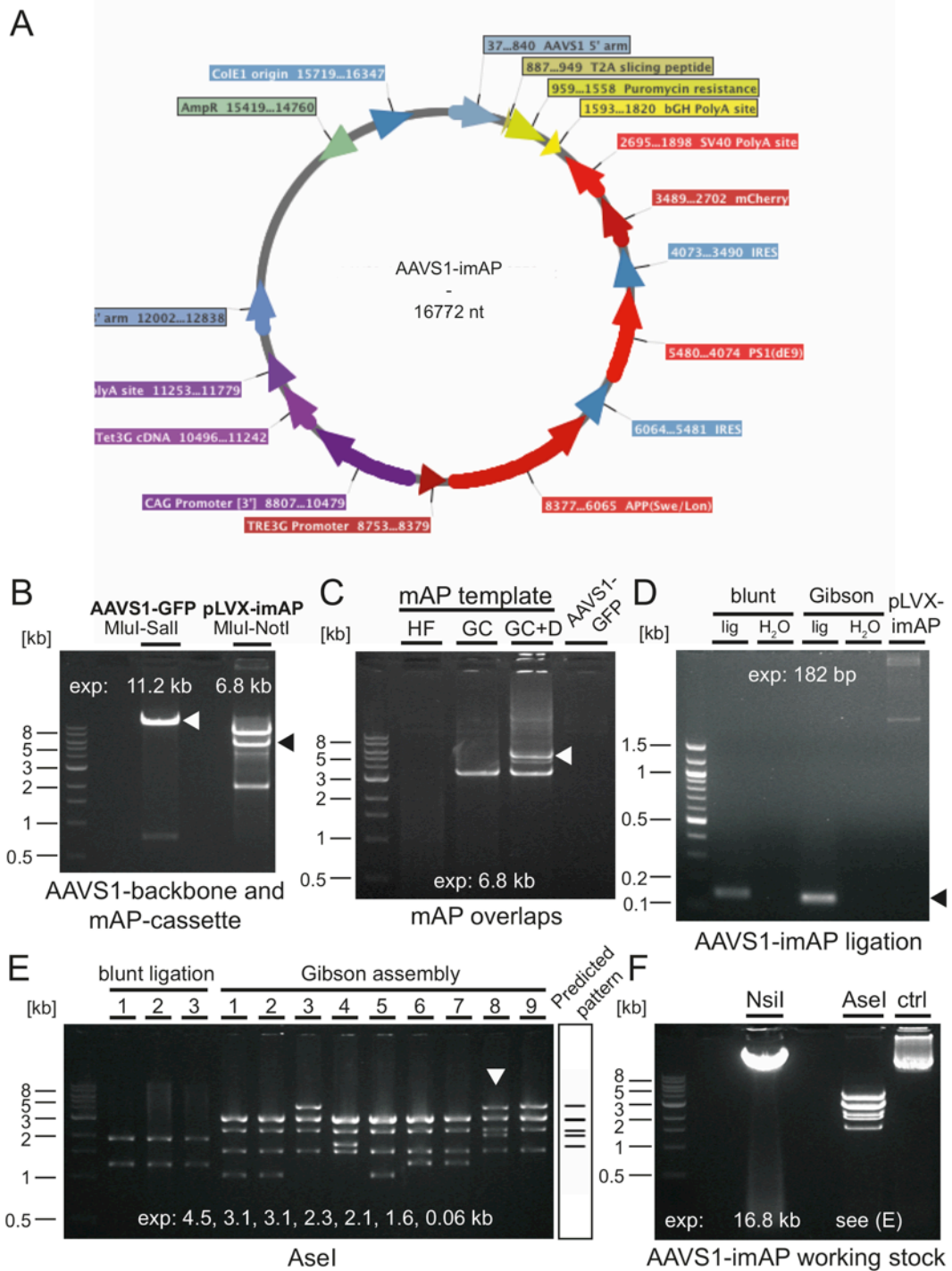
Figure 3.3 AAVS1-imAP plasmid
(**A**) The AAVS1-imAP plasmid replaces the GFP in the AAVS1 targeting backbone with an APPSwe/Lon-PS1ΔE9-mCherry (mAP) cassette. (**B**) Generation of the AAVS1 plasmid backbone and the mAP cassette by restriction of AAVS1-GFP and pLVX-imAP through restriction with MluI+SalI and MluI+NotI, respectively. White arrowhead: AAVS1 plasmid backbone. Black arrowhead: mAP cassette. (**C**) PCR reaction to add short AAVS1 homology arms to the mAP cassette for Gibson assembly. HF: High-fidelity buffer. GC: High-GC buffer. GC+D: High-GC buffer + 3 % DMSO. Arrowhead: mAP + overlaps band. (**D**) PCR reaction after AAVS1-imAP blunt-end ligation and Gibson assembly. Amplicon overlaps the

backbone-insert ligation site. Arrowhead: Expected amplicon size. (**E**) Restriction analysis of blunt-ligated and Gibson-assembled AAVS1-imAP bacterial clones with AseI. Virtual digest denotes the expected band pattern after correct ligation. Arrowhead: Clone used for further experiments. (**F**) Restriction analysis of AAVS1-imAP working stock with NsiI and AseI. White overlays indicate the expected size of the band(s) of interest and were placed over areas without detectable bands. Ctrl: Undigested plasmid.

To generate the targeting plasmid for insertion of the $APP_{Swe/Lon}$-PS-1ΔE9-mCherry (mAP) cassette into the AAVS1 locus of iPSCs, the GFP ORF in the AAVS1-GFP plasmid was replaced with the mAP cassette (Fig. 3.3 A). AAVS1-GFP was digested with MluI and SalI (both single cutters) to remove the GFP ORF from the plasmid backbone. The mAP cassette was liberated from the pLVX-imAP letiviral plasmid by restriction with MluI and NotI (single and double cutter, Fig. 3.3 B). To ligate the AAVS1 backbone and the mAP cassette, overlapping 15 nt stretches were added to the mAP cassette via PCR. The mAP cassette contains several repetitive, GC-rich sequences, so buffer for GC-rich sequences and additional DMSO were added to the reaction (Fig. 3.3 C). Blunt-end ligation and Gibson assembly were performed in parallel. Primers spanning the promoter-cassette ligation site detected intact plasmid resulting from both setups (Fig 3.3 D). However, bacterial transformation yielded fewer clones from the blunt-end ligation. In addition, restriction analysis of the bacterial clones with AseI (septuple cutter) revealed numerous recombination events (Fig. 3.3 E). *In silico* prediction of the correct band pattern of AAVS1-imAP matched one clone that was further validated by restriction analysis with NsiI (single cutter) and AseI after amplification of the bacterial clone Gibson #8 (Fig. 3.3 F).

3.2. Characterization of the recipient iPSC line

Pluripotent stem cells are characterized by their capacity to differentiate into all three germ layers and indefinite self-renewal. iPSC lines can accumulate mutations or genomic damage that provide a proliferative advantage by outcompeting non-aberrant cells. This phenomenon has been extensively described in recent years (Blasco et al., 2011, Oliveira et al., 2014). To ensure the quality of iPSCs, both stem-cell state and genomic integrity have to be validated. The induced pluripotent stem cell clone iLB-C14m-s11 was kindly provided by Julia Fischer after full validation including expression of the stem cell markers alkaline phosphatase, TRA-1-60, TRA-1-81 and SSEA-4,

spontaneous *in vitro* differentiation into all three germ layers (as indicated by immunostaining against AFP, SMA and TUBB3), teratoma formation in mice containing progeny of all three germ layers (represented by glandular tissue, cartilage and pigmented epithelium), and SNP analysis (unpublished data by Julia Fischer).

3.3. AAVS1 locus integrity

AAVS1 locus sequence in C14m s11 iPSCs
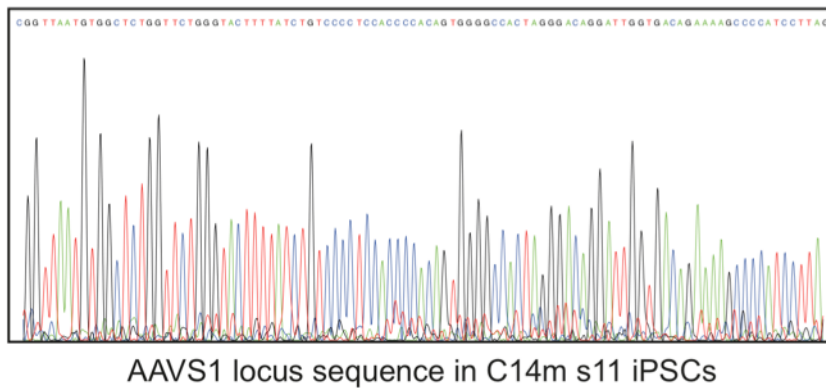
Figure 3.4 Genotyping of the AAVS1 locus sequence
The AAVS1 locus sequence in the iLB-C14m-s11 iPS cell line fully matches the reference genome.

Targeted genome engineering technology requires a precise match between the targeted nucleases and the actual DNA sequence. Since not all genetic backgrounds match the reference genome (refseq), the AAVS1 locus in iLB-C14m-s11 was validated by Sanger sequencing. PCR amplification of a ca. 670 bp amplicon surrounding the TALEN cutting site followed by Sanger sequencing revealed a 100 % refseq match (Fig. 3.4).

3.4. AAVS1 targeting and validation strategy
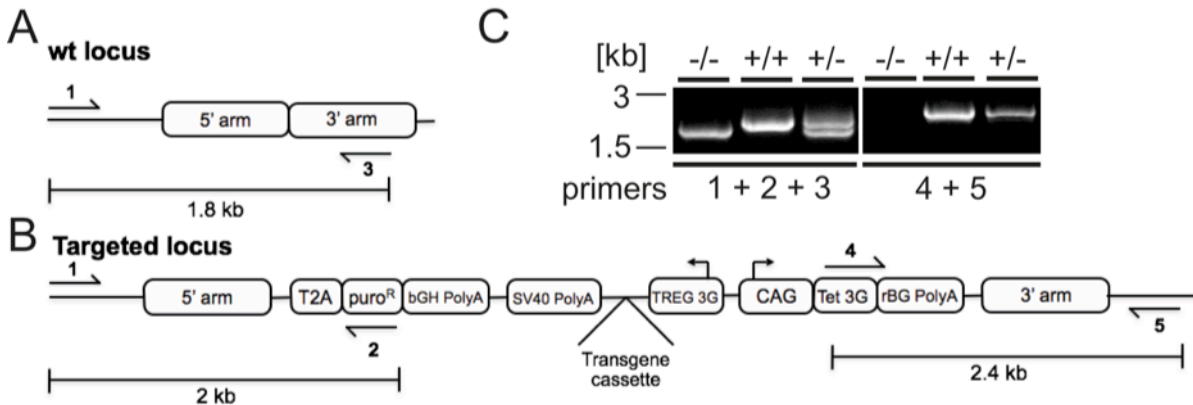
Figure 3.5 AAVS1 genotyping by multiplex PCR detects integration and zygosity
Multiplex PCR strategy using 3 primers for single-reaction analysis of 5' AAVS1 targeting in iPSC colony samples. (**A**) Untargeted alleles yield 1.8 kb products. (**B**) Primer binding outside the target region and inside the puromycin resistance gene yields a 2 kb product, whereas a P1+3 pairing in targeted alleles entails a >10 kb product that is unlikely to occur in the reaction. 3' insertion validation is achieved via P4+5 binding, yielding a 2.4 kb product. (**C**) Exemplary AAVS1-imAP PCR genotyping of puromycin-resistant iPSC clones.

The AAVS1 locus is a silencing-inert region in the human genome and thus a prime target for transgene insertion (Kotin et al., 1992). To simplify clone selection after targeting, the AAVS1-imAP construct was designed around a "gene-trap" strategy, i.e. to convey puromycin resistance to correctly targeted cells only via a splice-acceptor site. However, rare occasions of random in-frame integration into other genes give rise to resistant colonies as well. To demonstrate AAVS1 insertion and, at the same time, determine zygosity, a multiplex PCR protocol was established. Combining a forward primer 5' of the integration site (P1) with two reverse primers for the puromycin resistance cassette (P2) and 3' of the integration site (P3) respectively, potentially yields three products. In wild-type alleles, P1 and P3 give rise to a 1.8 kb product (Fig. 3.5 A). In inserted alleles, P1 and P2 will generate a 2 kb amplicon. A P1 and P3 pairing is theoretically possible – generating a ca. 13 kb product – but has never been observed (Fig. 3.5 B). The 3' end of the transgene can be further validated to exclude partial integration following a break in the plasmid during recombination. To this end, another primer pair (P4 and P5) spans the Tet3G sequence until outside the 3' homology arm to produce a 2.4 kb product from inserted alleles (Fig 3.5 B). Here, no distinction is made between homo- and heterozygous integrations. The PCR strategy yielded the expected band patterns when tested on puromycin-resistant targeted iPSC colonies (Fig. 3.5 C).

3.5. Derivation of genomically intact imAP iPSC clones
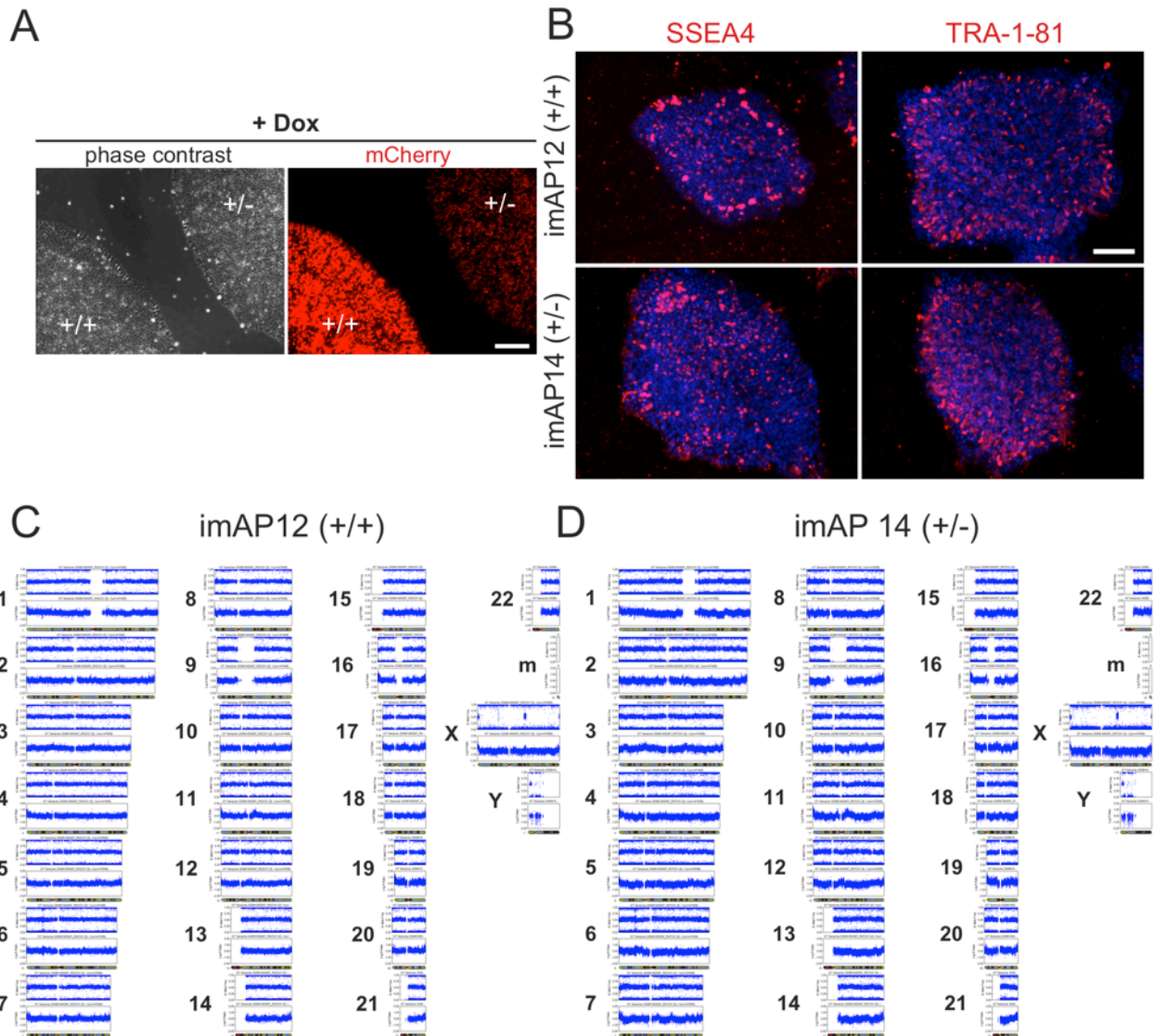
Figure 3.6 AAVS1-targeted iPSC clones show inducible reporter expression, iPSC characteristics and genomic integrity
(**A**) Phase contrast and fluorescence images of *post-hoc* genotyped AAVS1-imAP iPSC clones prior to picking after 72 h of doxycycline induction. mCherry reporter expression in red. Scale bar = 200 μm. (**B**) Immunostaining of iPSC markers SSEA4 and TRA-1-81 (both red) of both a homozygous (imAP12) and a heterozygous (imAP14) iPSC clone. Nuclear stain (DAPI) in blue. Scale bar = 100 μm. (**C+D**) Validation of genomic integrity by SNP analysis of homozygously and heterozygously integrated iPSC clones. Plots represent b-allele frequency and logR ratio for each chromosome.

Genetic engineering of human iPSCs requires the introduction of foreign genetic material. We chose nucleofection as a simple method for efficient transfer of DNA into iPSCs in suspension. 4×10^6 cells were nucleofected with 4 μg AAVS1-imAP and 0.5 μg of each TALEN plasmid. 5 μM DNA ligase IV inhibitor L755507 was added to improve homologous recombination efficiency during the first 24 h. Surviving cells formed

colonies on Geltrex-coated plates. After 72 h of recovery, puromycin selection reduced the number of colonies to 77 that were picked for validation. Taking half of each colony (approx. 200 - 500 cells) for genotyping revealed an AAVS1-insertion frequency of approximately 50 % biallelic integration, 45 % monoallelic integration, and 5 % random integration. Doxycycline induction (1 µg/ml) for 72 h conclusively showed the homogenous and gene-dosage dependent expression of the mCherry reporter in iPSC colonies prior to picking (Fig. 3.6 A, genotyping was performed after the fluorescence imaging). For further work, one biallelic (iLB-C14m-s11 imAP #12, short imAP12) and one monoallelic clone (iLB-C14m-s11 imAP #14, short imAP14) were subjected to iPSC validation. Targeted clones retained iPSC marker expression such as TRA-1-81 and SSEA-4 (Fig. 3.6 B). SNP data did not imply major aberrations in picked clones and confirmed the male identity of the donor iPSC line (Fig. 3.6 C, D).

3.6. Generation and validation of imAP lt-NES cells
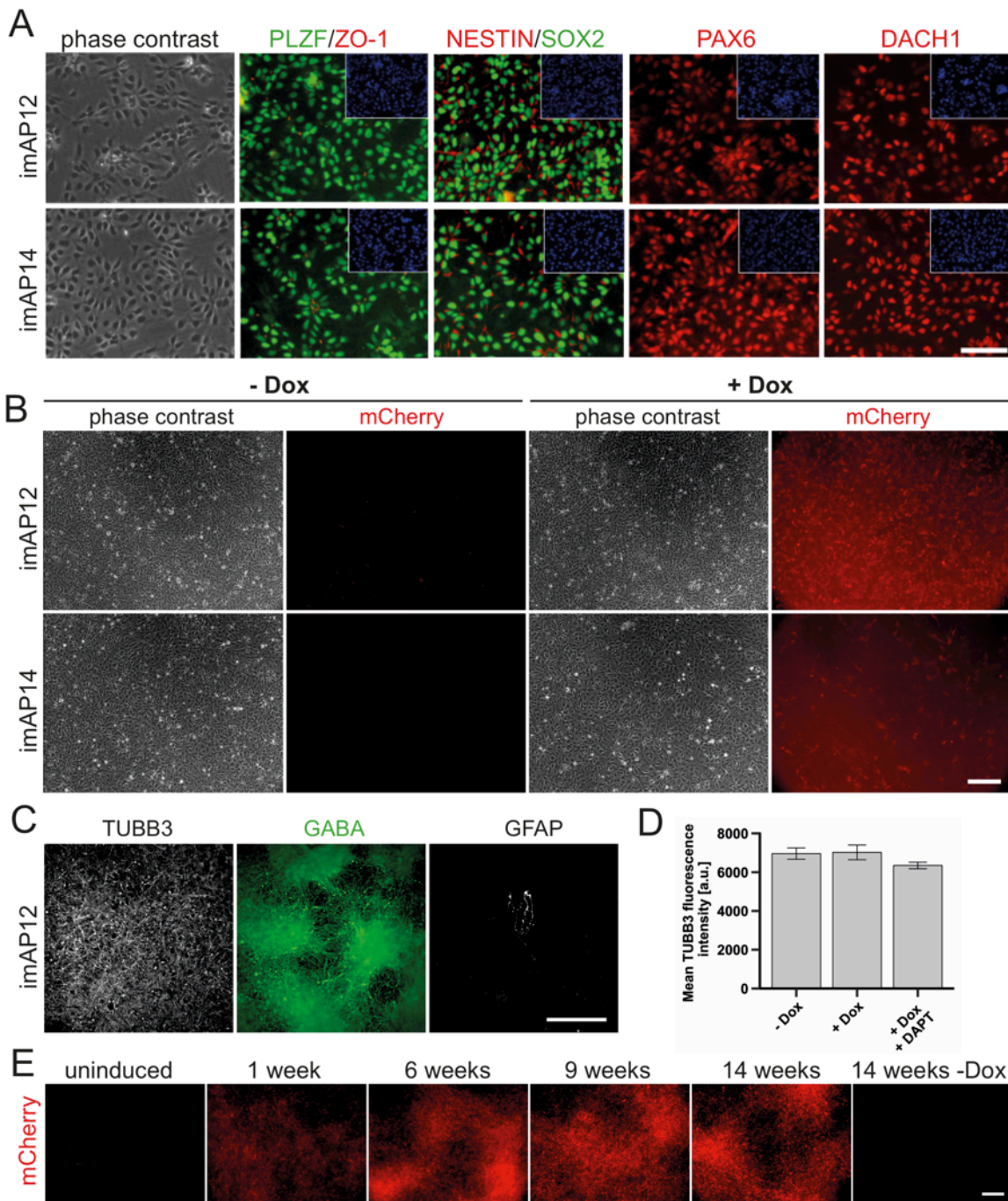
Figure 3.7 AAVS1-imAP iPSCs differentiate into lt-NES cells and neurons
(**A**) Analysis of lt-NES cell rosette type morphology (phase contrast) and neural stem cell markers PLZF, ZO-1, NESTIN, SOX2, PAX6 and DACH1. Scale bar = 100 μm. (**B**) Lt-NES cells derived from imAP12 and imAP14 iPSCs were plated and induced with doxycycline for 7 days. mCherry reporter in red. Scale bar = 200 μm. (**C**) Representative micrographs of high-density thin-layer imAP12 neurons after 6 weeks of differentiation by growth-factor withdrawal. Neural markers TUBB3 (grayscale), GABA (green) and astrocyte marker GFAP (grayscale). Scale bar = 500 μm. (**D**) Quantification of TUBB3 expression under different treatments. Mean TUBB3 staining intensity from whole-well imaging of 3-weeks-treated cultures.

Three independent experiments. Data presented as mean ± SEM. (**E**) ImAP12 transgene induction dynamics upon doxycycline treatment (1 µg/ml, mCherry in red). All images from high-density areas. Scale bar = 200 µm.

The next step after validation of the imAP iPSC clones aimed at the generation of a stable neural stem cell population to serve as a platform for further experiments. Long-term self-renewing neuroepithelial stem (lt-NES) cells provide a stable and expandable platform for standardized neural differentiation (Koch et al., 2009). This neural precursor population exhibits a regional identity similar to the midbrain-hindbrain boundary. Lt-NES cells derived from imAP12 and imAP14 iPSCs were highly proliferative and showed typical rosette morphology and expression of the neural stem cell markers PLZF, ZO-1, NESTIN, SOX2, PAX6 and DACH1 (Fig. 3.7 A). Upon induction with doxycycline, both genotypes expressed the mCherry reporter at the expected levels (Fig. 3.7 B). Since no overt differences could be found between imAP12 and imAP14 iPSCs and lt-NES cells up to this point, further work focused on the imAP12 clone to exploit its putatively stronger Aβ generation.

For the final differentiation step into a neuronal population, imAP lt-NES were subjected to growth-factor withdrawal to allow spontaneous differentiation into neuronal and astroglial fates. ImAP12 lt-NES cells were embedded in a thin-layer 3D culture via resuspension of the cell pellet in a 10 % Geltrex solution prior to seeding. The matrix was left to solidify at 37°C before additional NGMC medium was applied. ImAP12 neurons readily expressed neuronal markers TUBB3 and GABA after 6 weeks of differentiation, and the cultures contained a small fraction of GFAP-positive cells (Fig. 3.7 C). In order to determine the neuronal contribution to the cultures before the onset of major pathology, the different treatment conditions used in this work were analyzed for alterations in cell viability (AD-related neurodegeneration) and differentiation dynamics (DAPT treatment). Notably, culture densities were too high to allow reliable cell counting, so the analysis was based on whole-well measurements of mean TUBB3 immunofluorescence (Borghese et al., 2010). Three-weeks-treated cultures exhibited robust and homogenous TUBB3 expression irrespective of induction state or compound treatment. As expected, mean TUBB3 immunofluorescence was not significantly different between conditions. Due to these findings, all downstream IHC quantifications

were normalized to area rather than cell number (Fig. 3.7 D). To demonstrate the long-term stability of transgene expression in the AAVS1 locus, imAP12 neurons were induced with doxycycline from day 10 in 3D culture for up to 4 months. Expression of mCherry plateaued after approximately 14 days of induction and continued for the remainder of the experiment, whereas no expression was found in uninduced cultures (Fig. 3.7 E).

3.7. imAP12 3D matrix cultures show extracellular Aβ aggregation
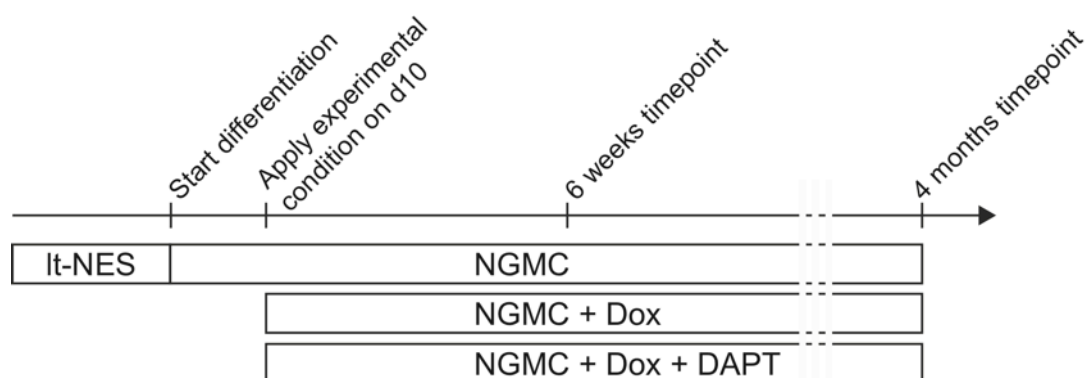
Figure 3.8 Experimental time line
Lt-NES cells are embedded in a matrix and differentiated for 10 days prior to application of the experimental condition to avoid transgene interference with early differentiation. Cultures were analyzed after 6 weeks or 4 months of treatment.

The differentiation paradigm used in this thesis starts at the embedding of lt-NES cells in a 3D matrix or seeding on a coated dish for 2D culture, respectively. Then, growth-factor withdrawal induced differentiation takes place for 10 days. Aβ generation is finally commenced by induction with 1 µg / ml doxycycline, and inhibition of APP processing (via DAPT) serves as a rescue. The respective experimental condition (either NGMC only, NGMC + Dox or NGMC + Dox + DAPT) is applied for the remainder of the experiment (Fig. 3.8).

3.7.1. Highly elevated $A\beta_{42}$ levels in induced neuronal imAP12 cultures
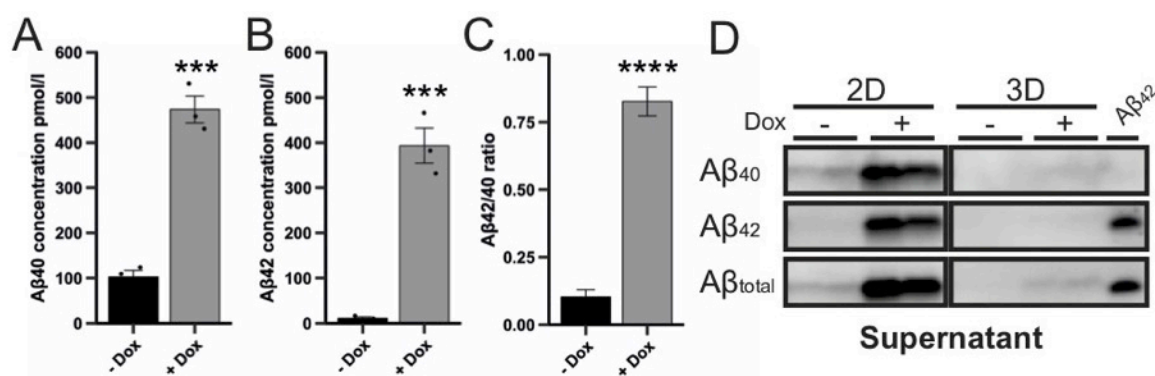
Figure 3.9 Aβ levels are strongly inducible and drastically higher in 2D than in 3D supernatants
(**A**, **B**) ELISA measurements of $A\beta_{40}$ and $A\beta_{42}$ in the supernatants of 4-8 weeks-treated imAP12 cultures in 2D. $2x10^6$ cells per well in 2 ml medium after 24 h of incubation. Three independent experiments. ELISA measurement was performed by Clara Grezella. Values are presented as mean ± SEM. Student's t-test. ***: $p < 0.001$. ****: $p < 0.0001$. (**C**) $A\beta_{42/40}$ ratio calculated from corresponding sample pairs. (**D**) Supernatant samples from 4-weeks-treated imAP12 cultures. $2x10^6$ cells per well in 2 ml medium after 48 h of incubation. Specific detection of $A\beta_{40}$, $A\beta_{42}$ and total $A\beta$. $A\beta_{42}$ lane was loaded with 0.1 ng recombinant $A\beta_{42}$. Two independent experiments. Western blot performed by Kevin J. Washicosky.

Aβ species in the supernatant of 2D imAP12 cultures were analyzed after 4 - 8 weeks of treatment to determine the impact of ectopic $APP_{Swe/Lon}$ and PS-1ΔE9 expression on Aβ secretion. All tested cultures were seeded with $2x10^6$ cells and incubated with 2 ml medium for 24 h before supernatant collection. ELISA measurements demonstrated a 5-fold increase in $A\beta_{40}$ (Fig. 3.9 A) and a 40-fold increase in $A\beta_{42}$ (Fig. 3.9 B). The $A\beta_{42/40}$ ratio – a parameter associated with Aβ toxicity – was increased 8-fold (Fig. 3.9 C).

Entrapment of Aβ is the main reason for using 3D matrix cultures for AD modeling. To test Aβ retention in the gel matrix, supernatants from 4-weeks-treated 2D and 3D cultures were collected after 48 h and compared in western blot analysis with antibodies against $A\beta_{40}$, $A\beta_{42}$, and total Aβ. In the supernatants of 2D cultures, baseline Aβ secretion was detected as faint bands, whereas doxycycline induced cultures showed dominant bands. However, in 3D culture supernatants, Aβ was virtually undetectable by western blot under baseline conditions, and minimally elevated in doxycycline-treated conditions (Fig. 3.9 D). Recombinant $A\beta_{42}$ (0.1 ng) was included in the analysis to demonstrate antibody specificity.

### 3.7.2. Evidence for autofluorescent Aβ precipitates in induced 3D cultures
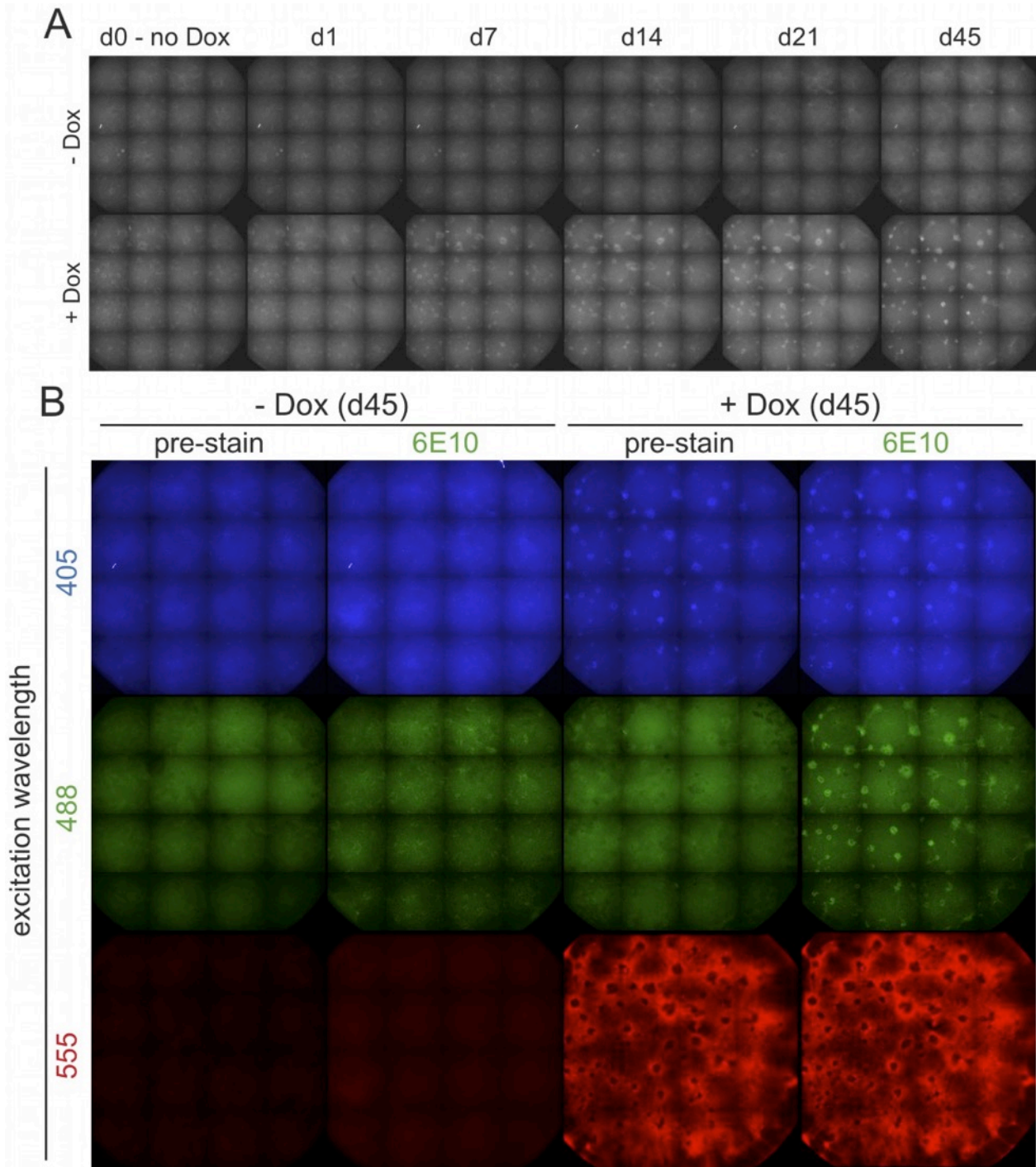
Figure 3.10 Autofluorescent deposits are formed progressively in 3D cultures and can be stained with anti-Aβ antibodies

(**A**) Time series of 405 nm induced autofluorescence in one thin-layer 3D culture with and without induction. Stitched image covers one well of a 96-well plate. (**B**) End-point analysis of (A). Pre-stain: Fluorescence images taken on day 45 of treatment before fixation. 6E10: Fluorescence images taken after fixation and staining with anti-Aβ (6E10, green) antibodies. mCherry reporter was visualized in the red channel. Stitched image covers one well of a 96-well plate.

After detecting robust Aβ secretion by induced imAP12 cultures, Aβ deposition was observed over time. Amyloid deposition has been shown to cause autofluorescence in affected tissues, i.e. amyloid plaques are easily recognizable in AD patient brain samples when excited with UV light or equivalent energy in 2-photon microscopy (Kwan et al., 2009). Imaging-grade culture plates enable time-lapse autofluorescence imaging of thin-layer 3D cultures over at least six weeks. The plates were automatically imaged with an excitation wavelength of 405 nm. While no difference was detected between the induction states at the start of the experiment and 24 h later, 405 nm-induced fluorescence increased in induced cultures starting from 7 days of induction. Induced cultures accumulated increasing amounts of autofluorescent material in diffuse regions (diameter 50-300 µm). Notably, the size, number, and position of these regions remained constant during the experiment (Fig. 3.10 A). Accumulation plateaued at approximately 21 days of induction.

End-point analysis was performed to determine the nature of the autofluorescent deposits (Fig. 3.10 B) after fixation. Fluorescence upon excitation with 405, 488 and 555 nm revealed specific autofluorescence in the 405, but not in the 488 nm channel. Furthermore, induced cells fluoresced in the mCherry channel, yet no red signal was found to co-localize with the deposits. The effect was exclusive to induced cultures; no specific 405 nm fluorescence was found in uninduced cultures. Next, the cultures were stained with antibodies against Aβ (6E10) in the green channel to explore Aβ contribution to the deposits. Antibody reactivity co-localized with the autofluorescent deposits in induced cultures, whereas only background signal was observed in uninduced cultures.

3.7.3. Amyloid dyes stain aggregates in 3D cultures
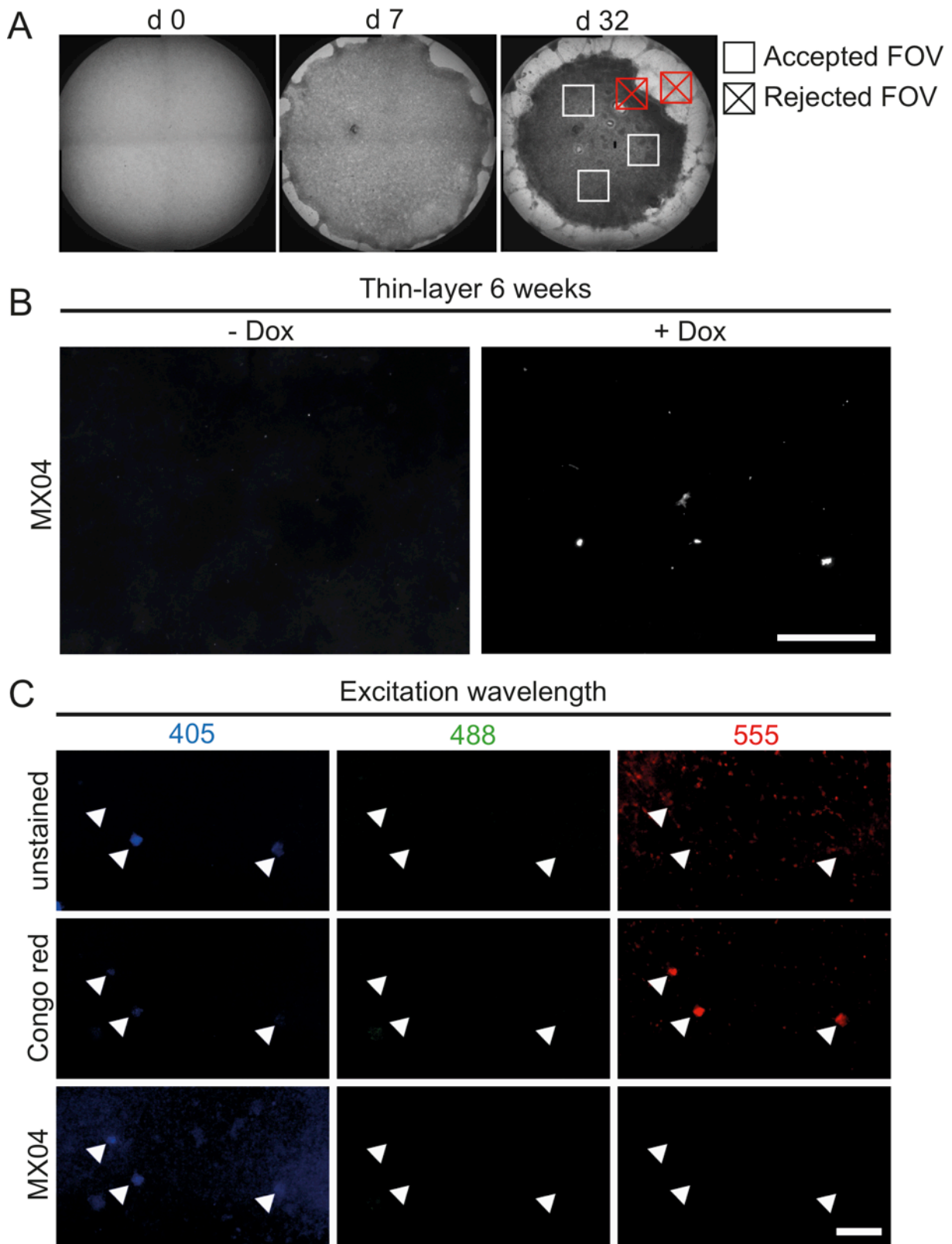
Figure 3.11 Aβ aggregates are stained by classical amyloid fibril dyes

(**A**) Whole-well micrographs of 96-well format thin-layer cultures illustrating matrix shrinkage during six weeks of differentiation. For high-magnification imaging, only random fields of view (FOV) were analyzed that showed a fully intact 3D matrix structure or otherwise excluded. The imaging plane was the arithmetic mean of the top- and bottommost cell-containing focal planes at the imaging location. (**B**) Low magnification fluorescence micrographs showing MX04 staining of 6-weeks-old thin-layer cultures with and without doxycycline induction. Observed in three independent experiments. Scale bar = 200 µm. (**C**) Sequential fluorescence imaging and staining of a 6-weeks-induced thin-layer 3D culture. Fluorescence elicited by 405 nm illumination presented in blue, 488 nm in green and 555 nm in red. All three aggregates (arrowheads) react to Congo red and MX04, but only two out of three are autofluorescent. Congo red fluorescence is lost during MX04 staining. No unspecific green fluorescence was detected. Unstained: Imaging after fixation. Congo red: Imaging after staining with Congo red. MX04: Imaging after staining Congo red and MX04. All images from high-density areas. One experiment. Scale bar = 100 µm.

Upon extended cultivation, the Geltrex matrix of 3D cultures is slowly degraded, leading to inhomogeneity of culture thickness and detachment of the gel from the border of the well (Fig. 3.11 A). To compensate for these effects, all high-magnification images were taken at random locations in the well and if the field of view was not completely within the 3D matrix, the picture was discarded and a new imaging location was randomly chosen. For confocal imaging, microphotographs were taken at the midpoint between top- and bottommost cells at a given location. To further confirm the amyloid aggregate identity of autofluorescent deposits in the 3D cultures, the classical amyloid fibril dyes Congo red and the derivative Methoxy-X04 (MX04), which align to amyloid fibrils in a similar fashion, were employed. The dyes are distinctly fluorescent since MX04 encompasses a smaller delocalized electron system that yields fluorescence in the UV channel. For overview images, 6-weeks-treated thin-layer cultures were stained with MX04. At low magnification, approximately 10-50 plaque-like structures per well of a 96-well plate became apparent in induced cultures only (Fig. 3.11 B). Notably, the stained structures appeared smaller and denser than the autofluorescent deposits shown above. To compare binding specificity, fixed 6-weeks-induced thin-layer 3D cultures were imaged for fluorescence elicited by UV (405 nm), blue (488 nm) and green (555 nm) light and sequentially stained with Congo red and MX04. Prior to any staining, the culture showed bright UV-induced fluorescence from two aggregate structures (Fig. 3.11 C, upper row). 488 nm light induced no fluorescence, whereas 555 nm revealed weak mCherry fluorescence from induced cells. After staining with Congo red in alcoholic solution, three aggregate structures became brightly fluorescent in the red channel, while blue fluorescence was diminished and no green fluorescence could be detected (Fig. 3.11 C, middle row). Finally, MX04 staining in alcoholic solution marked the three

aggregates in the blue channel, although with high background. Additionally, MX04 staining completely removed the Congo red signal from the three aggregates. No signal was detected in the green channel (Fig. 3.11 C, lower row).
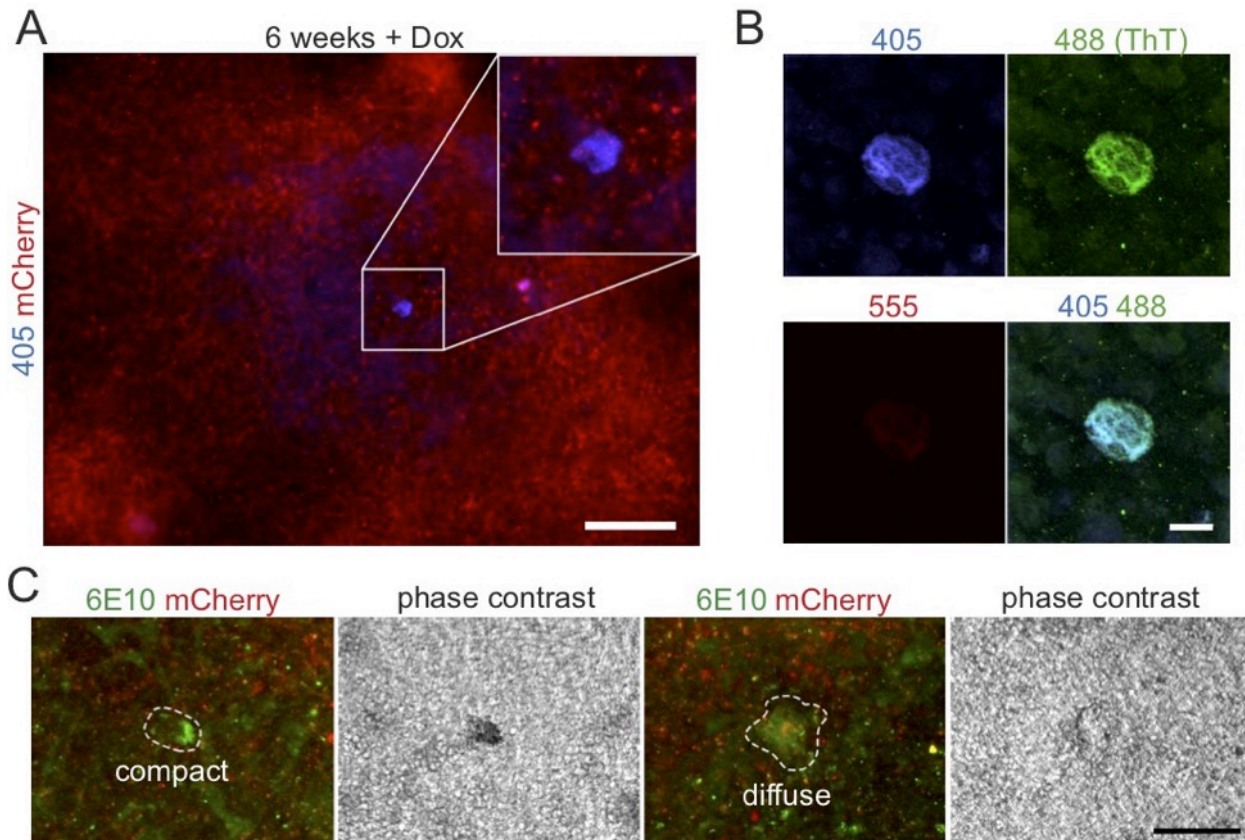

Figure 3.12 Dense autofluorescent deposits are stained by Thioflavin T and anti-Aβ antibodies
(**A**) Fluorescence image of a 6-weeks-treated thin-layer 3D culture. Deposit autofluorescence upon excitation with 405 nm light (emission in blue) and mCherry reporter (red) was observed in every experiment (n>10). Scale bar = 200 µm. (**B**) Dense autofluorescent deposit stained with ThT. Four independent experiments. Scale bar = 10 µm. (**C**) Anti-Aβ antibodies (6E10, green), mCherry reporter (red) and phase contrast images of different Aβ deposit types. All images were taken from high-density areas. One experiment. Scale bar = 100 µm.

In contrast to the large (>100 µm) and diffuse deposits visible in UV-induced autofluorescence, amyloid plaques are usually small (ca. 20 - 50 µm) and dense structures when observed in AD patient or transgenic mouse brains (Liebmann et al., 2016). Induced thin-layer cultures contained small, structured deposits ranging from 5 - 100 µm diameter (Fig. 3.12 A). While no considerable autofluorescence was detected in the GFP or mCherry channels, the fibril dye Thioflavin T stained the dense deposits, indicating the presence of β-sheet structures (Fig. 3.12 B). *In vivo*, amyloid plaques

appear as either small and dense, or larger and diffuse structures. The diffuse type contains fewer higher-order aggregates, and is thus hardly stained by amyloid dyes (Serrano-Pozo et al., 2011). Further characterization of the deposits with anti-Aβ antibodies (6E10) showed specific reactivity not only in the small, dense structures, but also in larger, diffuse deposits. ThT did not stain diffuse Aβ deposits. Also, while compact deposits were easily visible in phase-contrast imaging, the diffuse type was not (Fig. 3.12 C).

3.7.4. ThT-positive deposits show compact and fibrillar morphology
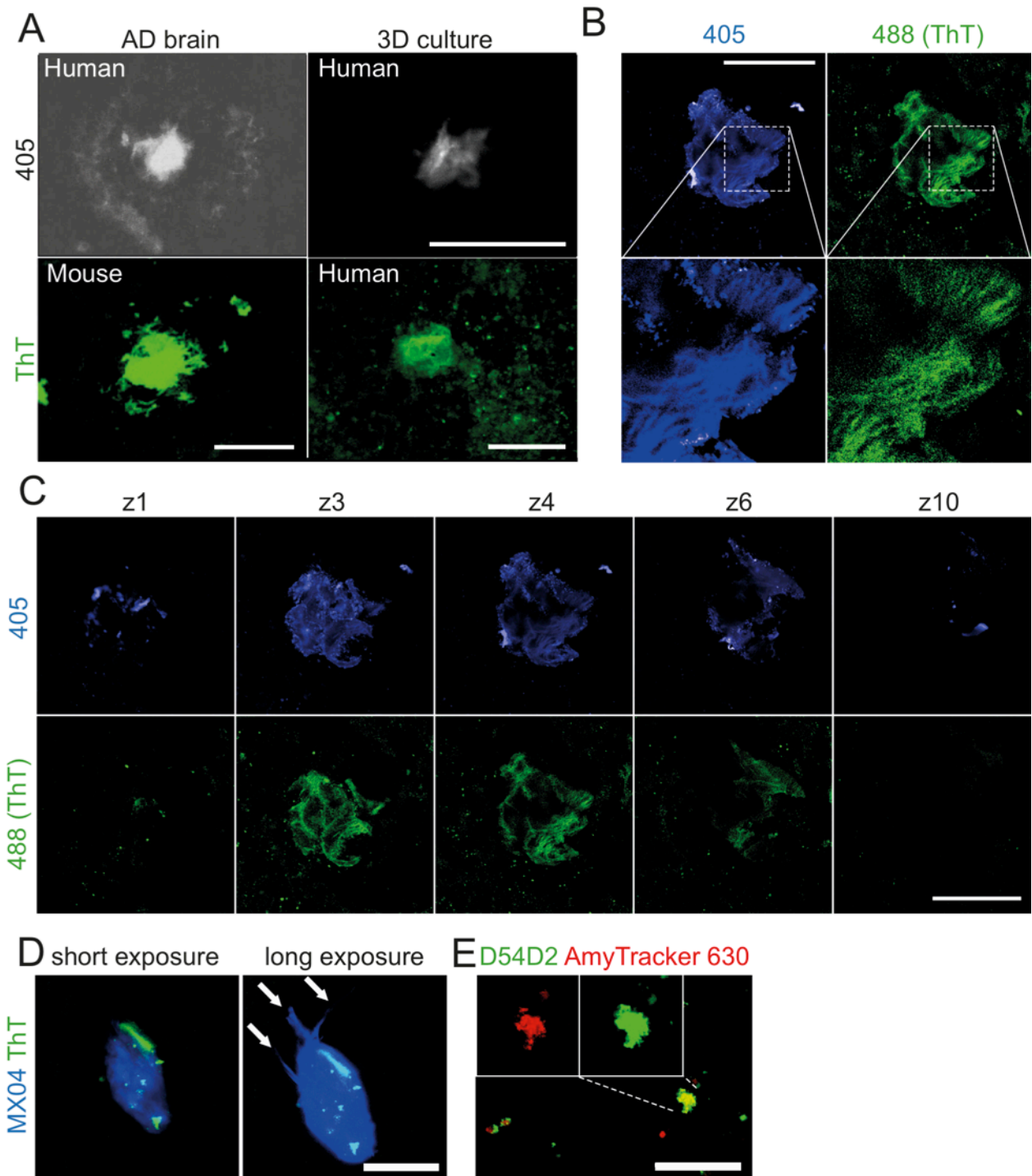
Figure 3.13 Amyloid aggregates in 3D cultures resemble human and transgenic mouse brain plaques

Amyloid aggregates in induced 3D cultures share several key features of amyloid plaques in the AD patient brain and commonly used mouse models. Amyloid plaques from brain tissue and amyloid aggregates in a 6-weeks-treated thin-layer 3D culture. Autofluorescence elicited by 405 nm (grayscale), and 488 nm (emission in green) light after PFA fixation and staining with ThT. AD patient cortical plaques (**A, upper left**, no scale, modified from Dowson et al., 1981) are autofluorescent in UV light in a similar

fashion to aggregates in 3D cultures (**A, upper right**, scale bar = 50 μm) Furthermore, amyloid plaques (**A, lower left**, Thioflavin S in a mouse brain section, scale bar = 50 μm, modified from Busièrre et al., 2004) are stained by amyloid fibril dyes like Thioflavin T in the same way as aggregates from 3D cultures (**A, lower right**, Thioflavin T, scale bar = 50 μm). Similar autofluorescent structures were observed in every experiment (n > 10) and at least one ThT-positive structure was observed in all ThT stainings (n = 3). (**B**) Confocal image of the aggregate from (A, lower panel). Scale bar = 50 μm. (**C**) Selected planes from a confocal z-stack image of the aggregate from (A). Scale bar = 50 μm. Z step = 2.2 μm. (**D**) Co-staining of amyloid aggregate dyes Methoxy-X04 and ThT. Longer exposure (right) with tendril-like protrusions from the main aggregate (arrows). One experiment. Scale bar = 20 μm. (**E**) Co-staining of amyloid aggregates with an anti-Aβ antibody (D54D2) and an amyloid aggregate dye (AmyTracker 630). Scale bar = 50 μm. One experiment. All images from high-density areas.

Amyloid aggregates in thin-layer 3D cultures shared many morphological characteristics with amyloid plaques in human and transgenic mouse brain tissue, such as specific autofluorescence and fibrous structures (Fig. 3.13 A). Based on the observations of delicate structural features in the amyloid aggregates, high-magnification confocal imaging was performed to further assess the internal aggregate makeup. Thioflavin T staining of autofluorescent deposits in 6-weeks-differentiated thin-layer 3D cultures routinely uncovered delicate structural features that did not fully co-localize with autofluorescence inside larger (> 20 μm) deposits. ThT also stained many smaller structures. Notably, these punctae did not display such fibrous features. In contrast, larger aggregates appeared to consist of fibrous bundles that bend and weave in three dimensions (Fig. 3.13 B). In addition, it should be noted that the autofluorescence and the ThT stain did not overlap completely. ThT did not stain the majority of amorphous, spherical autofluorescent particles along the rim of the aggregate, whereas both fluorescent readouts labeled the fibrillar components (Fig. 3.13 B zoom-in). This internal makeup was consistent across various planes within the aggregate as shown in selected planes from an image z-stack taken in 2.2 μm increments (Fig. 3.13 C). The larger aggregates mostly appeared ellipsoid in fixed cultures with the major axis aligned with the cell culture plate. Large, strongly ThT-positive aggregates presented as compact with clear borders. However, aggregates with weak ThT reactivity could be stained by Methoxy-X04 to reveal tendril-like extensions from the aggregate proper upon longer exposure (Fig. 3.13 D). To prove that the amyloid dye-reactive structures are in fact Aβ aggregates, 6-weeks-differentiated induced cultures were co-stained with the Aβ-specific antibody D54D2 and the amyloid dye AmyTracker 630, revealing co-reactive aggregates (Fig. 3.13 E).

### 3.7.5. Evidence for TBS- and SDS-insoluble Aβ in in thick-layer 3D cultures
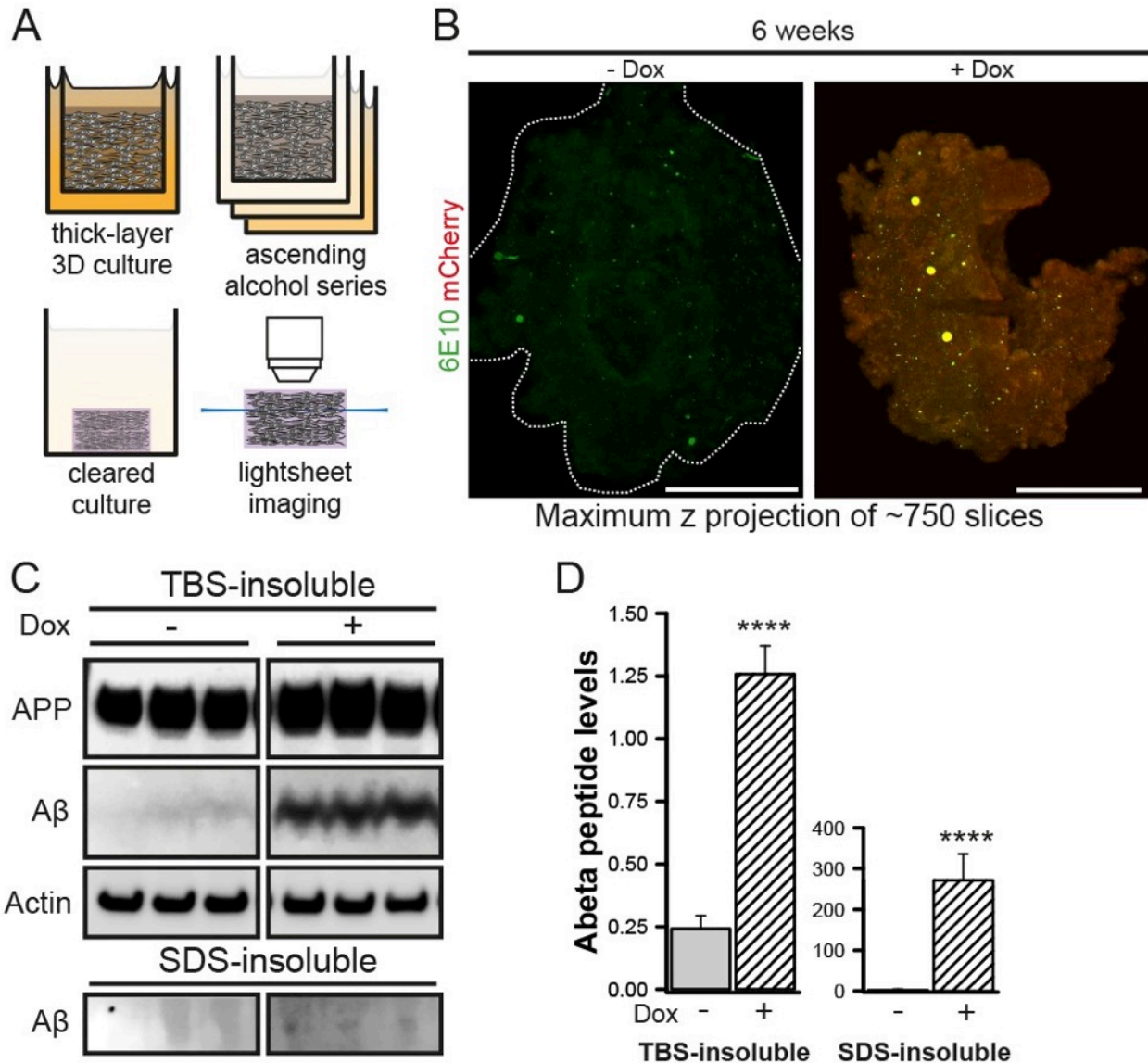
Figure 3.14 Thick-layer 3D cultures contain numerous Aβ aggregates and insoluble Aβ
(**A**) Thick-layer cultures were cleared for light-sheet imaging via an ascending alcohol series and incubation with a clearing reagent. Cleared cultures could be imaged several millimeters deep. (**B**) Light-sheet imaging of thick-layer cultures after 6 weeks of dox treatment. Imaging of Aβ (6E10, green) and mCherry (red). Sample preparation and image acquisition in collaboration with Andreas Elanzew. Maximum z projection of approx. 750 optical slices with 1.3 μm step size. One experiment. Scale bar = 500 μm. (**C**) Western blot analysis (performed by Kevin J. Washicosky, Harvard Medical School) and (**D**) quantification of 4-months-treated thick-layer 3D cultures. ****: p < 0.001. Data presented as mean ± SEM. Three independent experiments. Student's t-test.

The insolubility of amyloid deposits is another hallmark of human AD that does not occur in AD mouse models. To probe Aβ solubility in protein biochemical analyses, thick-layer 3D cultures were set up in analogy to thin-layer cultures, but with 4×10^6 lt-NES cells in 2

ml medium volume to supply more cell mass for protein harvesting. The cultures are cylindrical and, due to a higher gel concentration during seeding, more homogeneous along the z-axis. However, at 5 – 7 mm thickness, thick-layer cultures are not suitable for conventional imaging.

To illuminate Aβ aggregate formation inside thick-layer cultures, we adapted a clearing protocol for intact mouse brains (Schwarz et al., 2015) to fixed thick-layer cultures. The objective was to remove optical index differences between different cellular and tissue components that cause diffraction and dispersion during light microscopy. Here, fixed cultures were stained for 72 h each with primary and secondary antibodies against Aβ (6E10). Then the cultures were dehydrated by exposure to increasing concentrations of alcohol and finally embedded in a benzyl-alcohol / benzyl-benzoate (BABB) mixture for light-sheet fluorescence microscopy (LSFM) (Fig. 3.14 A). Induced thick-layer 3D cultures contained many Aβ-positive structures of various sizes after 6 weeks of doxycycline treatment in addition to mCherry fluorescence from induced cells. In comparison, uninduced cultures showed spotty background reactivity and occasional bubble-like larger reactive structures potentially resulting from dehydration artifacts (Fig. 3.14 B). The state of Aβ aggregation can be analyzed by solubility fractionation in aqueous buffers with increasingly more stringent solubilizing supplements. Most commonly, TBS (tris-buffered saline), SDS (sodium dodecyl sulfate) and FA (formic acid) buffers are used. The detergent-free TBS buffer dissolves soluble proteins, i.e. monomeric Aβ and is afterwards referred to as the TBS fraction. Insoluble material is removed via centrifugation and resuspended in SDS buffer, which is supposed to dissolve oligomers and lower order fibrils, termed the TBS-insoluble fraction. Remaining material is dissolved in FA buffer, i.e. mature fibrils, known as the SDS-insoluble fraction. Western blot analysis of the TBS- and SDS-insoluble fraction revealed a strong Aβ accumulation in TBS-insoluble fractions from induced cultures, while full-length APP was just moderately elevated. Furthermore, Aβ levels were significantly elevated in the SDS-insoluble fraction as well (Fig. 3.14 C). Densitometric quantification of Aβ band intensity from three independent experiments revealed a highly significant increase in TBS- and SDS-insoluble fractions upon doxycycline induction, even though the Aβ signal in the SDS-insoluble fraction was very faint (Fig. 3.14 D).

### 3.7.6. Application of a γ-secretase inhibitor prevents Aβ particle formation
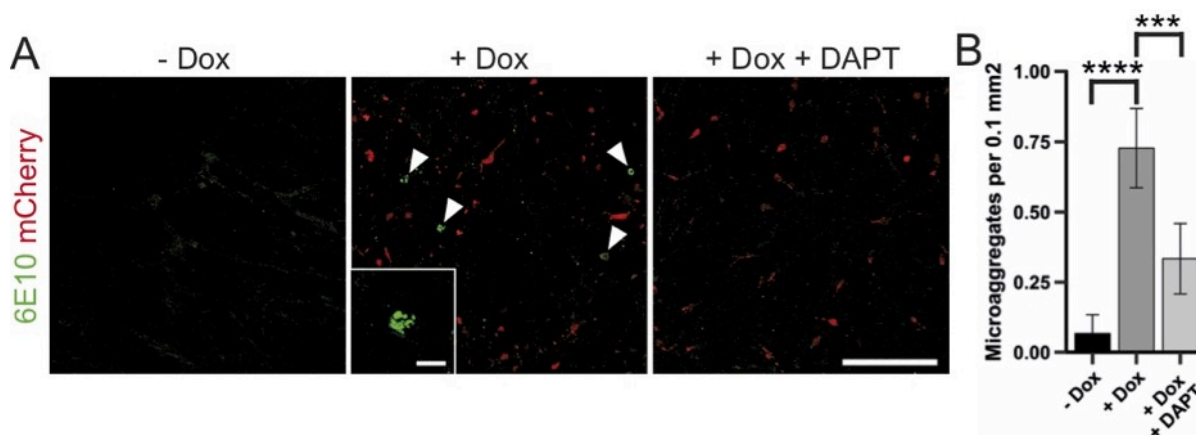
Figure 3.15 γ-secretase inhibition suppresses small Aβ particle formation
(**A**) Confocal images of thin-layer 3D cultures. -Dox cultures were cultivated without dox. +Dox cultures were induced for 6 weeks. +Dox+DAPT cultures were treated with doxycycline and 10 μM DAPT for 6 weeks. Detection of anti-Aβ antibodies (6E10, green) and the mCherry reporter (red). Scale bar = 100 μm, zoom-in: 10 μm. (**B**) Quantification of microaggregates (2-10 μm diameter) in 6-weeks-treated cultures. All analyzed images were taken in high-density areas. ****: $p < 0.001$, ***: $p < 0.01$. Three independent experiments. Data presented as mean ± SEM. One-way ANOVA with Tukey's post-hoc test.

Aβ aggregation occurs in a wide range of sizes at different frequencies. While larger structures (>20 μm) were rare, smaller, dense Aβ-positive particles (2 - 10 μm) were detected frequently (up to 10 per mm^2). To analyze the contribution of Aβ production to particle formation, a fraction of induced cultures was treated with 10 μM of the γ-secretase inhibitor DAPT that should block APP processing by γ-secretase and subsequently prevent Aβ release. DAPT was added together with doxycycline after 10 days of differentiation. After 6 weeks, induced cultures contained numerous small Aβ-positive particles (Fig. 3.15 A). On the other hand, uninduced cultures contained virtually no such structures. Additional DAPT treatment significantly lowered the particle count compared to induced cultures. Quantification from three independent experiments showed that induced cultures had approximately 17-fold, but DAPT-treated cultures only five-fold higher particle counts than uninduced cultures (Fig. 3.15 B).

3.8. Phospho-tau pathology in induced 3D cultures

### 3.8.1. Progressive accumulation of p-tau in induced 3D cultures
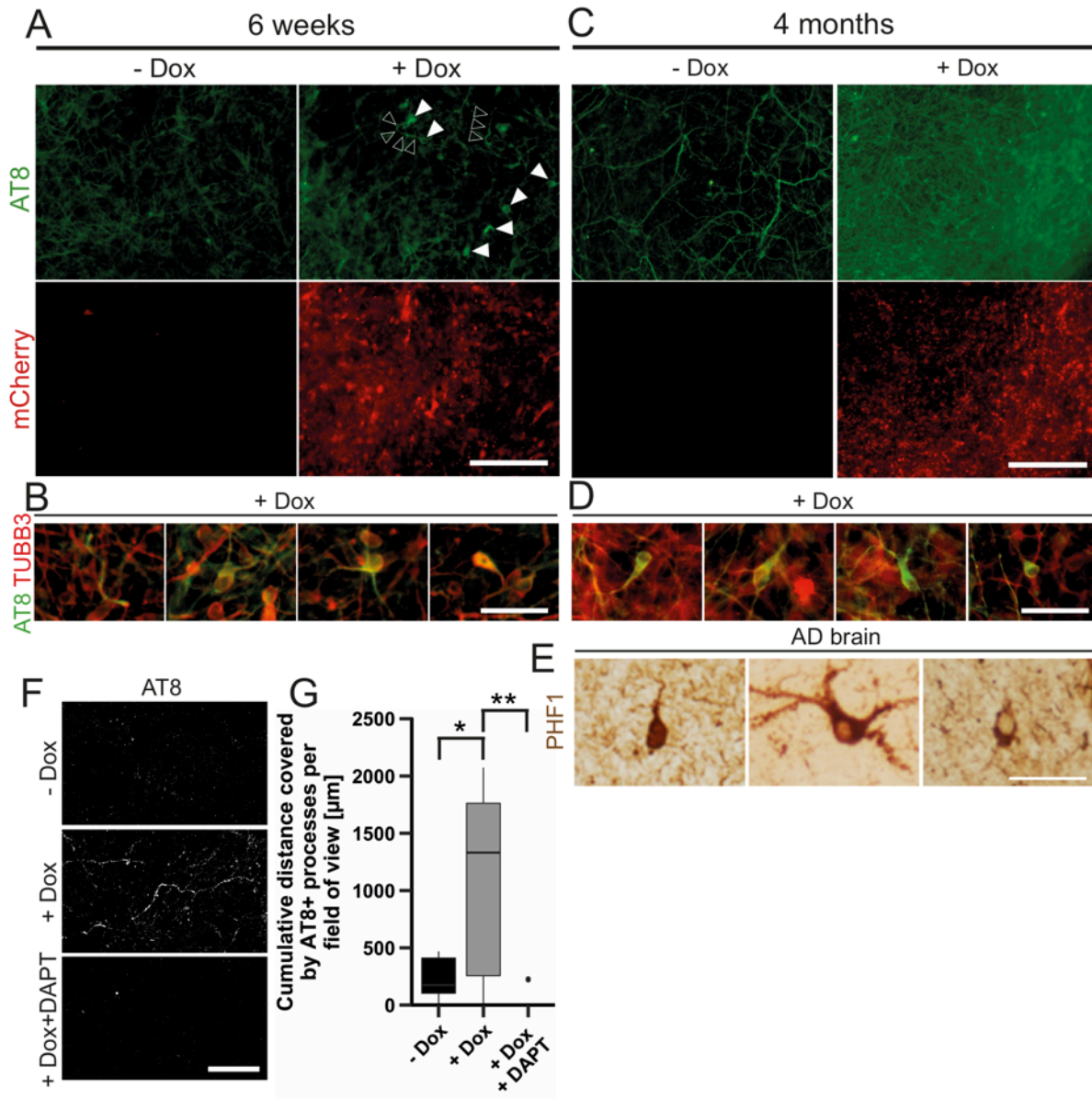
Figure 3.16 Progressive phospho-tau pathology in 6-weeks and 4-months-treated cultures presents increasingly dysmorphic neurons
(**A**) 6-weeks-treated cultures stained against phospho-tau (AT8, green) and mCherry (red). Arrowheads indicate intracellular accumulation of p-tau, particularly in the somatodendritic segment and in neurites. Scale bar = 200 µm. (**B**) High-magnification images of single neurons showing p-tau accumulation in neuritic or somatodendritic segments with minor morphological alterations. Scale bar = 25 µm. (**C**) P-tau detection as in (A) in 4-months-treated cultures. Scale bar = 200 µm. (**D**) High-magnification images of single 4-months-treated neurons with p-tau accumulation and morphological alterations similar to neurofibrillary tangles. All images from high-density areas. Scale bar = 25 µm. (**E**) Images of p-tau-positive (PHF1, brown) neurons from human AD brain immunohistochemical stainings for comparison. Several morphological types are represented, such as flame-shaped, ramified and perinuclear. AD brain

micrographs modified from Blazquez-Llorca et al., 2010. Scale bar = 50 µm. (**F**) Representative images used for tracing of strongly p-tau positive (AT8, grayscale) cellular processes in 6-weeks-treated cultures. Processes were measured using the NeuronJ FIJI plugin. Image shows AT8 antibody staining in confocal images. Scale bar = 100 µm. (**G**) Quantification of the total distance covered by strongly p-tau positive cellular processes per field of view. Three independent experiments with three images per experiment and condition. One-way ANOVA with Tukey's post-hoc test. *: $p < 0.05$, **: $p < 0.01$.

Apart from amyloid build-up, intracellular accumulation and aggregation of hyperphosphorylated tau protein is the second major hallmark of Alzheimer's disease. Here, first indications of accumulated tau phosphorylation on serine 202 and threonine 205 (AT8 antibody) could be detected in 6-weeks-induced neurons (Fig. 3.16 A). Local enrichment was observed in perinuclear and somatodendritic compartments, as well as in sharply defined neurite segments (Fig. 3.16 B). After treatment for 4 months, tau pathology was strongly increased in induced cultures, demonstrating high AT8 immunoreactivity in virtually all neurons. However, uninduced cultures also exhibited signs of increased tau phosphorylation in single cells, resembling a homogenous cytoplasmic stain (Fig. 3.16 C). Aggregated p-tau has been shown to induce particular changes to neuronal morphology, i.e. asymmetric displacement of the nucleus within a flame-shaped soma, complex ramification of a strongly p-tau-positive soma or the formation of dense and sharply defined perinuclear aggregates (Blazquez-Llorca, 2010). 4-months-induced cultures displayed these typical signs of p-tau pathology in single dysmorphic neurons (Fig. 3.16 D). Comparisons to published images of AD patient cortical tissue revealed matching dysmorphic soma shapes (Fig. 3.16 E, Blazquez-Llorca, 2010). P-tau pathology was quantified in 6-weeks-treated cultures by measuring the length and number of strongly p-tau positive cellular processes in confocal images of AT8-stained cultures using the NeuronJ FIJI plugin (Fig. 3.16 F). In uninduced conditions, each field of view contained strongly p-tau positive processes with an average total length of 230 µm (range 0 – 470 µm). In contrast, the average total length was increased 4-fold to 1020 µm (range 0 – 2070 µm) in induced cultures. In DAPT-treated cultures, an average length of 50 µm was measured (range 0 – 230 µm)(Fig. 3.16 G).

### 3.8.2. P-tau positive neurons present dystrophic features
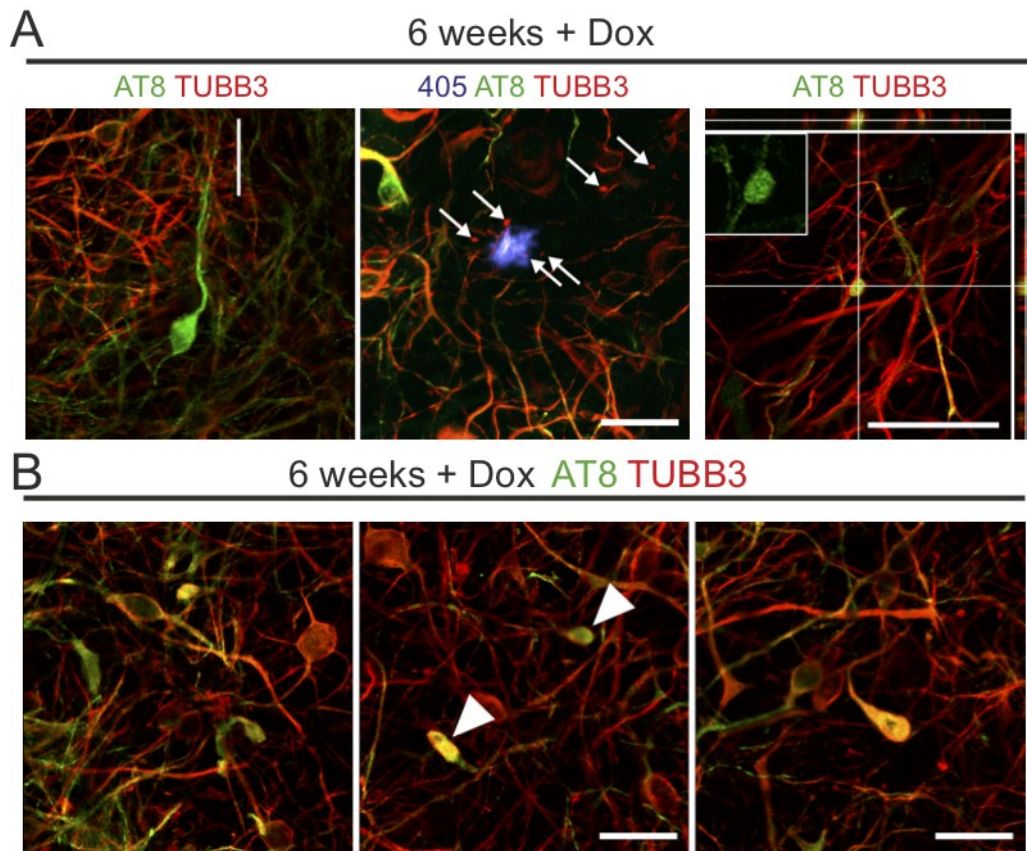
Figure 3.17 Dystrophic neuronal structures can be detected in 6-weeks-induced 3D cultures
6-weeks-treated cultures stained against p-tau (AT8, green) and neurons (TUBB3, infrared, presented as red). (**A**) Representative images of various typical stages of neuronal dystrophy in 6-weeks-induced thin-layer cultures. P-tau-positive „remnants"(left), bloated neurites in the vicinity of an autofluorescent aggregate (excitation with 405 nm, arrows, middle) and p-tau positive axonal swellings (z-stack, right). Similar structures were observed in three independent experiments, and only in induced cultures. Scale bars = 50 μm. (**B**) Swollen, p-tau-positive neurites in various stages of swelling. All images from high-density areas. Similar structures were observed in three independent experiments. Scale bar = 50 μm.

6-weeks-induced thin-layer cultures displayed further specific hallmarks of tau pathology and neuronal dystrophy, while uninduced cultures did not. Single neuronal "remnants", i.e. strongly p-tau positive structures that do not co-stain with other neuronal markers like TUBB3, were found. The density of neuritic terminals was reduced in close proximity to autofluorescent deposits, together with bloating of neuritic terminals. Furthermore, a subset of cellular processes exhibited bulbous distensions that stained strongly for phospho-tau inside a TUBB3-positive envelope (Fig. 3.17 A). Numerous neuritic terminals localized distant from deposits displayed bottle-shaped bloating. The bloated

terminals were strongly stained with phospho-tau antibodies (AT8) and enveloped by TUBB3 staining (Fig. 3.17 B).

3.8.3. Induced 3D cultures show evidence for high-molecular weight forms of p-tau
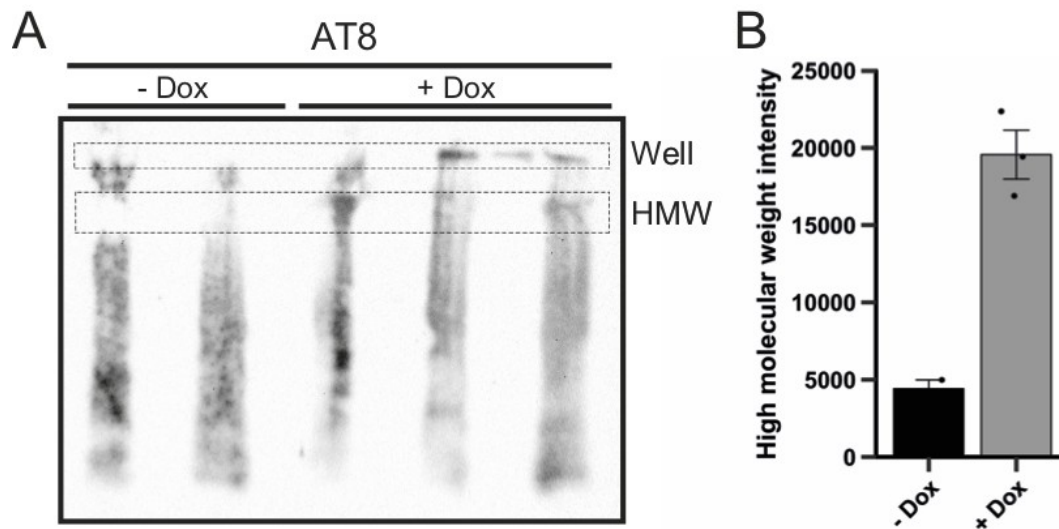
**Figure 3.18 6-weeks-induced 3D cultures contain aggregated p-tau**
(**A**) SDD-AGE of 6-weeks-treated thick-layer 3D cultures was detected with anti-p-tau antibodies (AT8). Well: Location of the gel pocket bottom prior to blotting. HMW: High-molecular weight range. Two and three independent experiments for -Dox and +Dox, respectively. n=1. (**B**) Quantification of the high-molecular weight range by densitometric analysis. Data presented as mean ± SEM. SDD-AGE was performed by Lea Flitsch.

Strong p-tau accumulation in induced cultures suggested the presence of aggregated tau. To determine the different aggregation states of p-tau in 6-weeks-induced we performed Semi-Denaturing Detergent Agarose Gel Electrophoresis (SDD-AGE) followed by western blot analysis of raw culture lysates (in collaboration with Lea Flitsch). P-tau aggregation is a staged process that encompasses various oligo- and multimeric intermediates, as well as fibers of varying length. In contrast to SDS-PAGE, protein complexes and aggregates are not fully denatured in SDD-AGE, thus requiring large-pored agarose gels.

Uninduced cultures presented a well-defined gap in the high-molecular weight (HMW) range of the smear and had no phospho-tau immunoreactivity at the well site (Fig. 3.18 A). Contrarily, smears from induced cultures continued across the HMW range and, in

two out of three cases, displayed a strong signal at the former well site. Quantification of the HMW range showed a clear increase between induced and uninduced conditions (Fig. 3.18 B).

### 3.8.4. Neurofibrillary tangle formation and aggregated p-tau
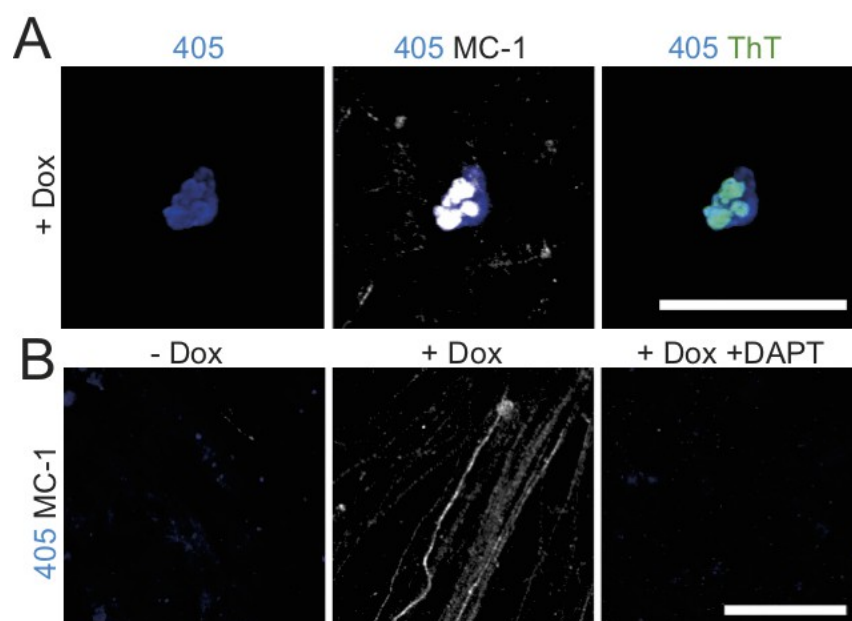
Figure 3.19 Aggregated p-tau localizes to dystrophic neurites
(**A**) Aggregated p-tau in the "paperclip" conformation is a hallmark of tau pathology and neurofibrillary tangles. Confocal micrograph of an amyloid aggregate from a doxycycline-treated culture. Detection of amyloid autofluorescence (blue), "paperclip" tau (MC-1 antibody, grayscale) and Thioflavin T (green) in 4-months-treated thin-layer 3D cultures. All images from high-density areas. One experiment. Scale bar = 50 µm. (**B**) Representative confocal micrographs of "paperclip" tau in 4-months-treated thin-layer 3D cultures. Detection of amyloid autofluorescence (blue) and "paperclip" tau (MC-1 antibody, grayscale). All images from high-density areas. One experiment. Scale bar = 50 µm.

Aggregation of hyperphosphorylated tau is accompanied by particular conformational changes. During the formation of tau fibrils, tau proteins adopt a "paperclip" conformation that can be recognized as a discontinuous epitope by specific antibodies, such as MC-1. To determine whether typical pathological changes occur to tau conformation in induced 3D cultures, 4-months-induced cultures were compared to uninduced and DAPT-treated induced controls. MC-1-positive neurites were detected in induced cultures. Surprisingly, such neurites routinely ended in blotch-like terminals on, or inside of larger autofluorescent aggregates (three out of three observed large aggregates were associated with MC-1 reactivity) (Fig. 3.19 A). The aggregates themselves also exhibited weak and diffuse MC-1 reactivity (Fig. 3.19 A). To confirm the

aggregated nature of p-tau stained by MC-1, Thioflavin T was added and strong co-labeling with MC-1 was observed. Similar to the six-week stage, no UV-induced autofluorescence or MC-1 immunofluorescence was detected in uninduced cultures. (Fig. 3.19 B). Induced cultures displayed autofluorescent aggregate structures similar in size and number to earlier observations (Figs. 3.11 & 3.12). Beyond the immediate vicinity of autofluorescent aggregates, single highly MC-1-reactive cells could be found, often as part of neurite bundles. In DAPT-treated cultures, neither aggregate-like autofluorescence nor MC-1 reactivity could be detected (Fig. 3.19 B).

3.9. Disturbed mitochondrial network architecture and energy metabolism
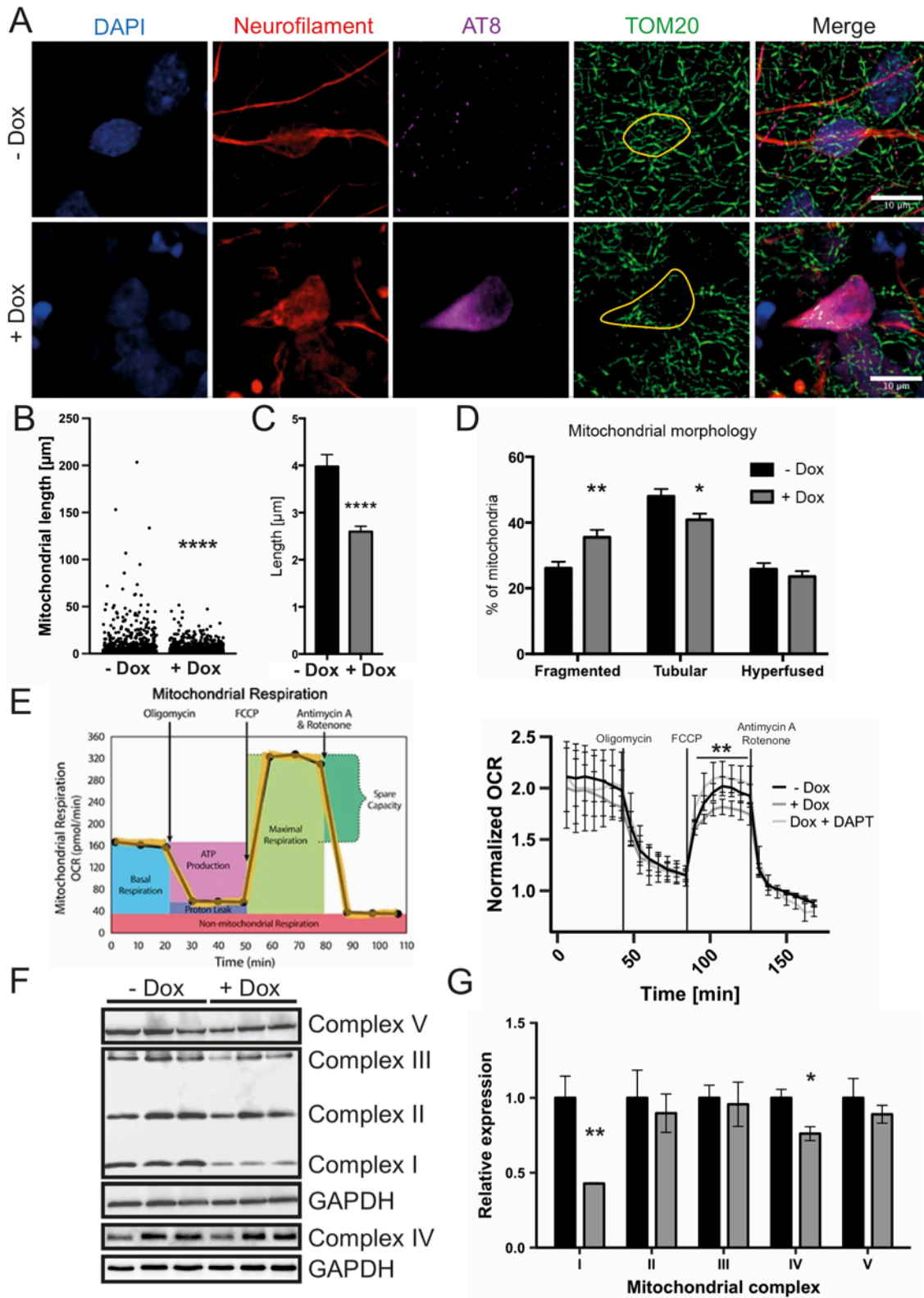
Figure 3.20 Mitochondria in induced 3D cultures are subject to fragmentation and reduced respiratory capacity
(**A**) Maximum-z projections of representative cells for mitochondrial morphology quantification. Nuclear stain (DAPI, blue), neuronal soma shape (neurofilament, red), p-tau (AT8, violet) and mitochondria (TOM20, green). Neurofilament stain was used to calculate a 3D mask from each z-stack representing a single neuronal soma. Yellow overlay in TOM20 staining illustrates masking. Mitochondria inside the mask were quantified by calculation of a 3D tubular reconstruction of each mitochondrial network and determination of the longest non-branching and non-crossing path across such network (mitochondrial length). All images from high-density areas. (**B**) Mitochondrial length distribution. ****: $p < 0.001$. Measurements from 14 individual cells from one culture per condition. (**C**) Data from (B) presented as mean ± SEM. (**D**) Data from (B) stratified into large mitochondrial networks (hyperfused), elongated tubes (tubular) and spheroid/ellipsoid (fragmented). Data presented as mean ± SEM. **: $p < 0.01$, *: $p < 0.05$. Stainings and quantification were performed by Fabio Bertan. (**E**) Left: Schematic overview of Seahorse oxygen consumption rate measurement. Image from agilent.com/en/products/cell-analysis/mitochondrial-respiration-xf-cell-mito-stress-test. Right: Normalized oxygen consumption rate (OCR) of 6-weeks-old thin-layer cultures in basal conditions (6 - 42 min), 2 µM oligomycin (48 - 84 min), 2 µM FCCP (90 - 126 min) and 1 µM antimycin & rotenone (132 - 168 min). Three independent experiments. Data presented as mean ± SEM. ANOVA. **: $p < 0.01$. Seahorse analysis was performed by Dr. Antonia Piazzesi. (**F**) Western blot analysis of mitochondrial complex proteins from 6-weeks-treated thin-layer cultures. Three independent experiments. (**G**) Densitometric quantification of mitochondrial complex proteins relative to GAPDH. Quantities were normalized to the mean of the respective uninduced group. Three independent experiments. Data presented as mean ± SEM. Student's t-test. **: $p < 0.01$. *: $p < 0.05$. Western blot analysis performed by Dr. Antonia Piazzesi.

Alzheimer's disease is strongly associated with mitochondrial impairment, especially by fragmentation of the mitochondrial network (Bonda et al., 2011). Interestingly, supporting mitochondrial integrity in AD mouse models promotes neuronal survival and cognitive capacity (Wang et al., 2017). To analyze mitochondrial impairment in this model, mitochondria were characterized in collaboration with Dr. Daniele Bano's group at the German Center for Neurodegenerative Diseases (DZNE) in Bonn. As a first step, fusion and fission dynamics can be measured based on mitochondrial length, an abstract value representing the longest non-branching and non-crossing path across a mitochondrial network. To determine mitochondrial length, 6-weeks-treated thin-layer cultures were immunostained with antibodies against neurofilament, p-tau and the mitochondrial membrane marker TOM20 (in collaboration with Fabio Bertan). Images were acquired as z-stacks for three-dimensional mitochondrial network reconstruction (Fig. 3.20 A). Following simplification of the reconstructed networks into a tube model (i.e. connected geometric lines tracing the network), cell soma boundaries were determined by three-dimensional masking with the neurofilament signal (Fig. 3.20 A, yellow overlay). Finally, mitochondrial length was automatically calculated. Comparisons between randomly selected cells in induced and uninduced cultures did not yield statistically significant differences (data not shown). Maximum mitochondrial length was reduced from 200 µm

to 50 μm specifically in AT8-positive cells from induced cultures compared to uninduced cultures. Similarly, average mitochondrial length was reduced by approximately 30 % in AT8-positive neurons (Fig. 3.20 B + C). It is currently thought that during mitochondrial fragmentation smaller structures bud off from large networks to remove irreparably damaged segments (Wang et al., 2017). Therefore, mitochondria were stratified into fragmented, tubular and hyperfused groups, depending on the respective length measurement. Here, induced cultures showed an increase in fragmented and a decrease in tubular mitochondria, while the overall number of larger networks remained unchanged (Fig 3.20 D). To cumulatively measure mitochondrial functionality in thin-layer cultures, 6-weeks-old cultures were subjected to Seahorse analysis (Fig. 3.20 E, left). First, oxygen consumption rate (OCR) was measured in homeostasis. In the second step, oligomycin inhibits the ATP synthase. Next, FCCP forms proton-permeable pores in the mitochondrial membrane, unlocking the maximal OCR. Finally, a combination of antimycin and rotenone collapses the mitochondrial membrane proton gradient by inhibiting the electron transport chain, reducing mitochondrial respiration to zero so that only non-mitochondrial respiration is detectable. Three-dimensional cultures were readily adapted to the Seahorse platform in 24-well format. Notably, each condition had to be applied twice as long as for 2D cultures to ensure steady-state OCRs. Measured OCR values were normalized to the mean value of the last analysis segment (antimycin + rotenone; no mitochondrial respiration) for each condition to remove the influence of different cell numbers. Uninduced cultures displayed a typical OCR profile in response to the compounds (Fig. 3.20 E, right). In contrast, induced cultures demonstrated reduced maximum OCR ($p<0.05$) comapred to uninduced cultures, while γ-secretase treatment prevented the reduction ($p<0.01$) compared to induced cultures. To determine whether the alterations result from defects in the electron transport chain, western blot analysis was used to quantify marker proteins for the major respiratory chanin complexes. Analysis of 6-weeks-treated thin-layer cultures demonstrated significant reductions in subunits of complexes I and IV by 60 % ($p < 0.01$) and 25 % ($p < 0.05$), respectively. These two complexes together establish the mitochondrial proton gradient. In contrast, complexes II, III and V were unaltered (Fig. 3.20 F + G).
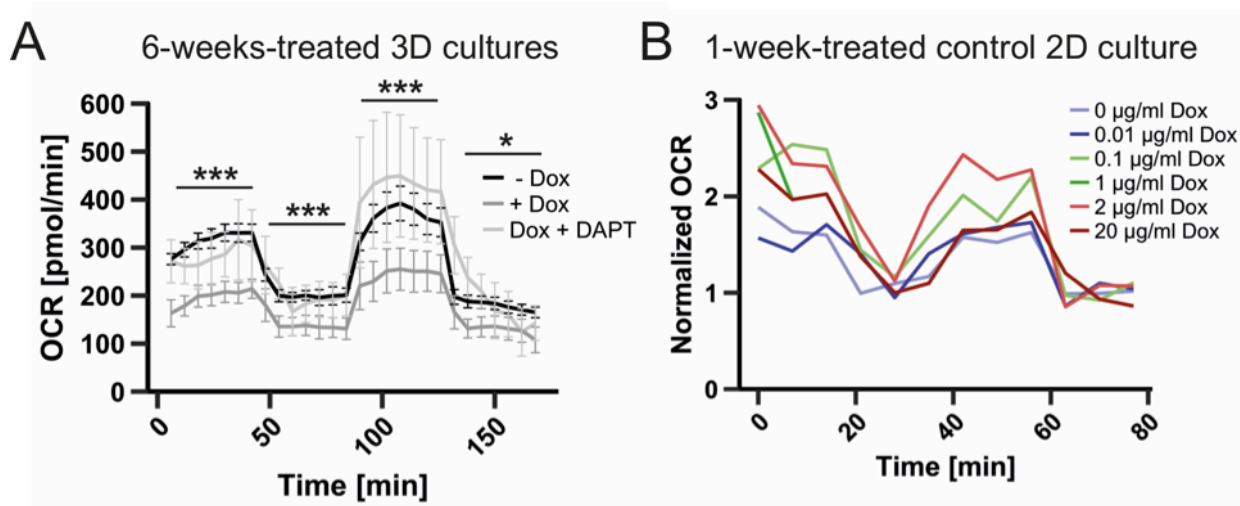
Figure 3.21 Doxycycline treatment does not impair mitochondrial respiration
(**A**) Non-normalized plot of Seahorse measurements shown in Fig. 3.20 (6 weeks of treatment). Oxygen consumption rate (OCR) of 6-weeks-old thin-layer cultures in basal conditions (6 - 42 min), 2 µM oligomycin (48 - 84 min), 2 µM FCCP (90 - 126 min) and 1 µM antimycin & rotenone (132 - 168 min). Three independent experiments. Data presented as mean ± SEM. ANOVA. ***: $p < 0.001$, *: $p < 0.05$. Seahorse analysis was performed by Dr. Antonia Piazzesi. (**B**) Normalized OCR of 1-week-treated non-transgenic neurons in basal conditions (0 - 14 min), 2 µM oligomycin (21 - 35 min), 2 µM FCCP (42 - 56 min) and 1 µM antimycin & rotenone (63 - 77 min). Data presented as mean. One experiment. Seahorse analysis was performed by Dr. Antonia Piazzesi.

The antibiotic doxycycline has been shown to impair mitochondrial respiration in several cell lines *in vitro* (Chatzispyrou et al., 2015). In order to exclude doxycycline as a potential confounder of the mitochondrial pathology detected in induced 3D cultures, the OCR measurements of 6-weeks-treated 3D cultures (Fig. 3.20) were reanalyzed in a non-normalized plot (Fig. 3.21 A). Notably, the OCR curve of dox-treated cultures was shifted downwards in a highly significant fashion ($p < 0.001$ for basal, oligomycin and FCCP conditions, $p < 0.05$ for antimycin + rotenone). However, the downward shift did not occur in cultures that were additionally treated with 10 µM DAPT. Next, we analyzed whether doxycycline had a dose-dependent effect on maximum OCR. To this end, non-transgenic lt-NES-derived neurons were cultivated for one week in 2D culture. During cultivation, the cells were treated with six different doxycycline concentrations ranging from 0 to 20 µg / ml. Maximum OCR in these cultures was ranked from low to high in the following conditions: 0 µg, 0.01 µg, 1 µg, 20 µg, 0.1 µg, 2 µg doxycycline (Fig. 3.21 B).

## 3.10. Cell stress in 3D induced cultures depends on γ-secretase activity
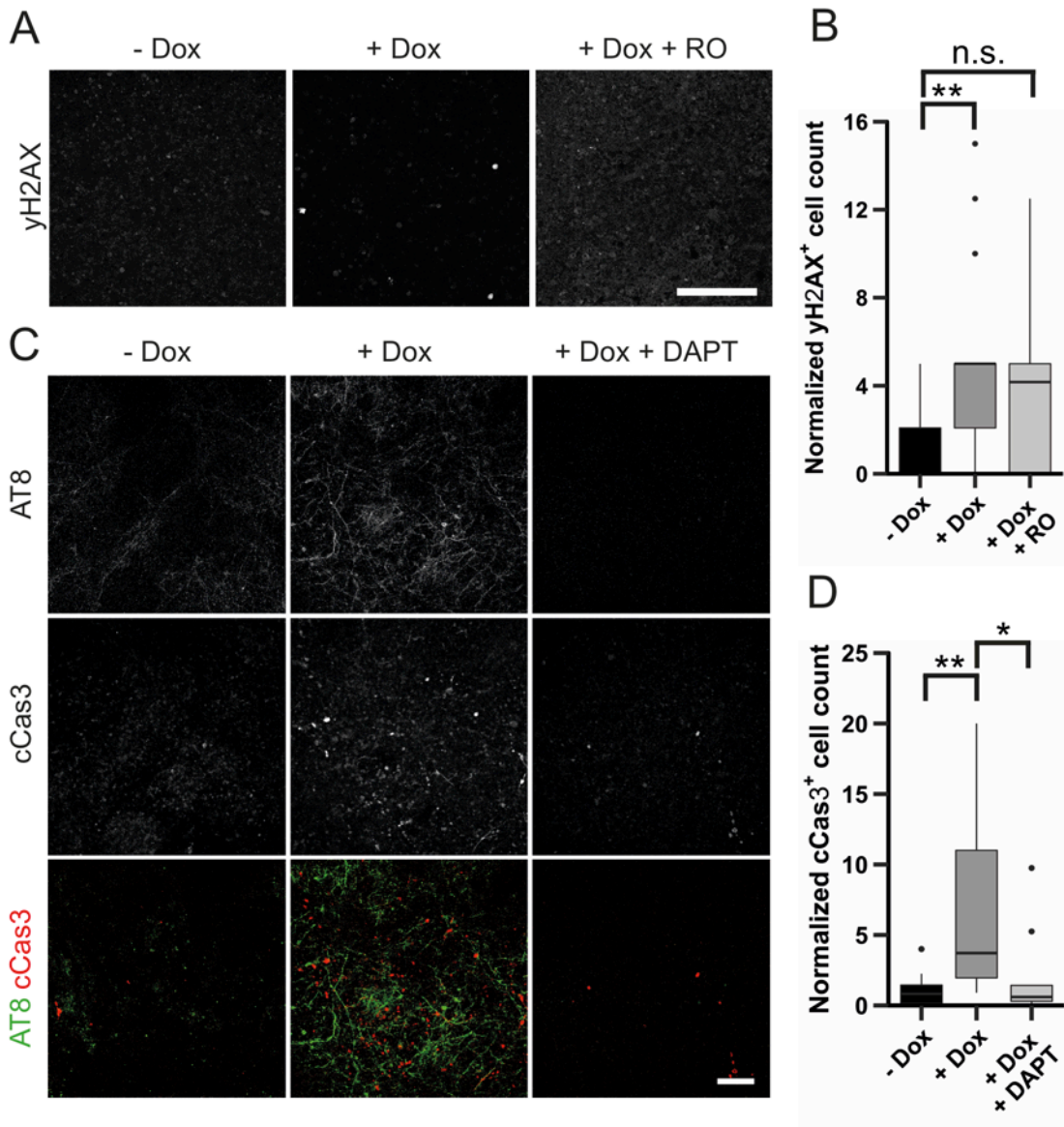
Figure 3.22 Elevated cell stress and apoptosis rate in induced 3D cultures can be reduced by γ-secretase inhibition
(**A**) Confocal micrographs of 6-weeks-treated thin-layer 3D cultures stained with antibodies against the DNA double-strand marker gamma-phosphorylated histone 2A (γH2AX). All images from high-density areas. Scale bar = 50 μm. (**B**) Quantification of γH2AX-positive cells. **: $p < 0.01$. Three independent experiments. Kruskal-Wallis with Nimenyi's post-hoc test. (**C**) Confocal micrographs of 6-weeks-treated thin-layer 3D cultures stained with antibodies against p-tau (AT8) and the apoptosis marker cleaved-caspase 3 (cCas3). All images from high-density areas. Scale bar = 100 μm. (**D**) Quantification of cCas3-positive cells. **: $p < 0.01$, *: $p < 0.05$. Three to four independent experiments. Kruskal-Wallis with Nimenyi's post-hoc test. All quantifications were normalized to the arithmetic mean of the -Dox condition within each independent experiment.

Late stages of Alzheimer's disease are characterized by pronounced brain shrinkage due to progressive neuronal degeneration. To assess Aβ-driven cell stress and apoptosis, we analyzed markers of cellular degeneration in three-dimensional cultures. First, DNA damage was analyzed via immunostaining for phosphorylated histone 2A (γH2AX), a marker of DNA double-strand breaks and, in cases of strong nuclear reactivity, apoptosis (Fig. 3.22 A). Notably, overall positive cell counts varied between independent experiments. Therefore, all data points, i.e. counts from single images, were normalized to the arithmetic mean of the -Dox condition within each independent experiment to correct inter-experimental variability. Dox-treated cultures displayed significantly more nuclei that were highly positive for DNA double-strand breaks than untreated cultures ($p < 0.01$, Fig. 3.22 B), while γ-secretase inhibition via a small-molecule inhibitor of γ-secretase, RO4929097, (100 nM) reduced γH2AX immunoreactivity and abolished significance. To confirm whether the cells entered apoptosis, the apoptosis marker cleaved (activated) caspase 3 (cCas3) was immunostained in 6-weeks-treated cultures. Cas3 serves as an effector caspase for both the intrinsic and the extrinsic apoptotic pathway, and therefore is a surrogate marker for apoptotic processes in general. Induced cultures presented considerable p-tau signal intensity in somatic and neuritic compartments (as shown earlier, Fig. 3.16) and a strongly elevated number of cCas3-positive cells (Fig. 3.22 C). However, the distribution of cCas3-positive cells varied from 0 to 24 per field of view between images from the same culture. Quantification revealed a significant five-fold increase of cCas3-positive cells in induced over uninduced cultures (Fig. 3.22 D). Notably, strong AT8 staining did not overlap with cCas3-staining and vice versa. Uninduced thin-layer cultures showed no accumulated p-tau, similar to earlier experiments. Analogously, cCas3 reactivity was detected sporadically, in isolated cells. According to the amyloid cascade hypothesis, eliminating Aβ production should reduce downstream pathologies like p-tau accumulation and cell death irrespective of APP$_{Swe/Lon}$ or PS-1ΔE9 overexpression. Adding 10 µM DAPT to induced cultures was attempted to minimize Aβ generation through γ-secretase inhibition. DAPT-treated cultures displayed no AT8 immuno-reactivity and 3-fold lower cCas3-positive cells than induced cultures, whereas no significant difference was found between uninduced and DAPT-treated cultures.

4. Discussion

Alzheimer's disease is the most common neurodegenerative disorder and the leading cause of dementia in the elderly. Despite extensive research into the disease, current knowledge has proven insufficient for effective therapeutic interventions. One major hurdle is the lack of suitable model systems for basic research and drug development, since mouse models have consistently failed to deliver predictive value for human treatments, while human brain samples are generally not available for extensive longitudinal studies. This project aimed to establish a highly standardized human iPSC-derived model of AD in authentic neurons that recapitulates all major disease hallmarks in an Aβ-driven manner.
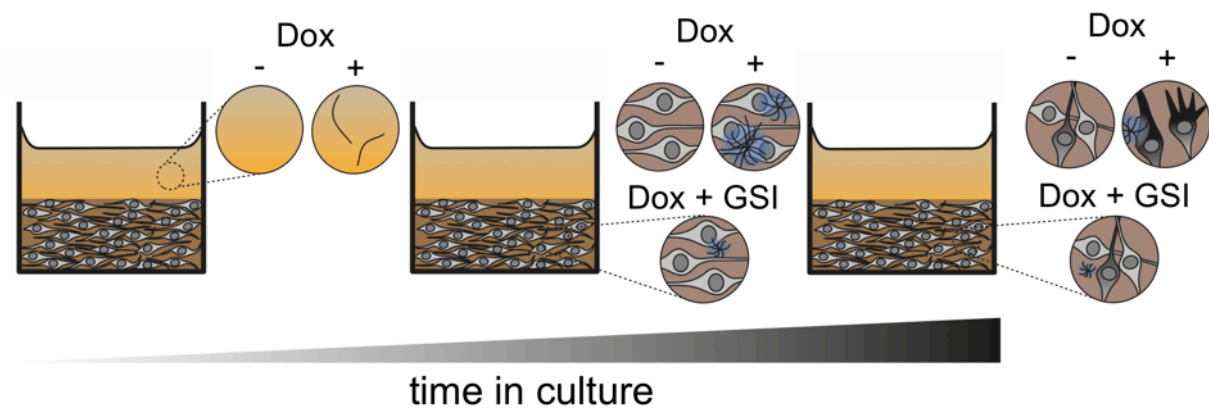
Figure 4.1 Progressive development of Alzheimer's disease pathology in 3D cultures
The AD model developed in this thesis recapitulates the pathology development as predicted by the amyloid cascade hypothesis. Induction of Aβ generation causes progressive accumulation and aggregation of amyloid-β in the culture supernatant of 3D cultures, the formation of amyloid plaques and, later on, p-tau pathology. Induced cultures display altered mitochondrial morphology, impaired respiratory capacity and elevated levels of apoptosis. Blocking Aβ generation via γ-secretase inhibition prevents amyloid deposition, p-tau pathology and normalizes cell stress.

4.1. iPSCs from a healthy donor retain stem cell characteristics and genomic integrity after transgene targeting into the human AAVS1 safe-harbor locus

In order to create a standardized and controllable model, a doxycycline-inducible transgene cassette consisting of APPSwe/Lon, PS1ΔE9 and an mCherry reporter should be inserted into a silencing-exempt genomic safe harbor. The AAVS1 safe-

harbor site was selected to host the transgene cassette for inducible Aβ generation since it is largely inert to silencing in the human neuronal lineage (Qian et al., 2014). Preliminary attempts to introduce the mAP cassette into human iPSCs via lentiviral transduction led to virtually complete transgene silencing within 1-3 weeks (data not shown), underscoring the importance of transgene stability. The iPSCs used for this project had undergone extensive quality control, including pluripotency marker expression, differentiation into all three germ layers and genomic integrity. Prior to imAP insertion, Sanger sequencing confirmed the integrity of the AAVS1 locus. Sequencing of the genotype-determining region of APOE, the most relevant AD risk factor, revealed an ε3/ε4 genotype that is associated with a moderate increase of AD risk (Huang et al., 2017, Michaelson, 2014). However, even a high-dosage treatment with APOE 4 *in vitro* merely caused only a 1.5 – 2-fold increase in endogenous APP expression in a recent study (10 µg/ml APOE ε4 vs. APOE ε3, Huang et al., 2017). Accordingly, even unphysiologically high APOE 4 levels exert only mild influence on APP expression, so that the APOE genotype is expected to have a minor impact on the model. The clone used for this thesis was additionally subjected to SNP analysis to validate genomic integrity. SNP analysis relies on genotyping a large number (i.e. 100,000) of common variants in the human genome, enabling a genomic integrity check at superior resolution compared to classical karyotyping, such as G-banding. However, since the imAP clone-derived cultures differ only in doxycycline and secretase inhibitor treatment, higher resolution genomic analysis such as exome or whole-genome sequencing is likely not necessary.

Upon nucleofection of the donor plasmid and two TALEN plasmids into iPSCs sufficient numbers of colonies formed after puromycin selection with an efficiency range of one resistant colony per 10,000 seeded cells. The rather low number of insertion events might be enhanced by optimizing the nucleofection protocol and using improved hardware, such as the 4D nucleofector. Furthermore, replacing the TALENs with more efficient CRISPR-Cas9, either as plasmids or as preloaded ribonucleoprotein (Cas9 protein + gRNA, "RNP") complexes might boost homologous recombination.

Validation and genotyping of AAVS1-targeted iPSC clones aimed to determine three key parameters: Transgene integration into the AAVS1 locus, insertion zygosity and cassette integrity. To this end, a multiplex PCR strategy for single-reaction determination of

integration and zygosity was devised. It combines a puromycin resistance-specific primer with two primers up- and downstream of the AAVS1 insertion site (Akajima et al., 2009). The reaction generates a 2 kb product for inserted, and a 1.8 kb product for wild-type alleles that are easily distinguished in agarose gel electrophoresis. Heterozygous clones yield two bands of equal signal intensity, whereas mixed clones often display one strong and one weak band. To a degree, this enables screening for average insertion frequency in polyclonal approaches by collecting bulk DNA. To guide genome repair mechanisms towards homologous recombination, the DNA ligase IV inhibitor L755507 was added to the cells for the first 24 h as it has been reported to increase recombination efficiency (Yu et al., 2015). The homologous recombination method used here carries a risk of failure leading to vector breakage and partial transgene insertion (Mizuno et al., 2009). To exclude partial integrations, an additional conventional PCR reaction was established to analyze the cassette at the 3' end. Since the PCR-based strategy successfully determined all relevant insertion parameters, no additional genotyping assays such as Southern blot analysis using multiple probes, or whole-genome sequencing, were employed.

In contrast to insertion frequency, faithful safe-harbor targeting in puromycin-resistant clones proved to be exceptionally high (95 %), distributed evenly among homo- and heterozygous insertions, and surpassing previously reported outcomes in terms of resistant colonies (200 / 10^7 cells vs. reported 30 / 10^7 cells) and integration efficiency (95 % vs. reported 70 %) (Qian et al., 2014). AAVS1-imAP iPSC clones of the two possible genotypes (mono- and biallelic insertion) were inducible and the validity of the genotyping PCR was reflected by lower mCherry fluorescence intensity in clones carrying only one copy. Dox-controlled systems enable temporal control over transgene expression, with two major downsides. First, upon induction, it takes several days for mCherry fluorescence to accumulate to measurable levels. This is expected since construct expression is not instantaneous, but ramps up over several days before reaching a plateau phase (Qian et al., 2014). This phenomenon is especially relevant for ORFs downstream of IRES sequences due to their lower translation efficiency (Mizuguchi et al., 2000). Given the long timeframe of the presented experiments, the ramp-up phase is likely insignificant as long as the plateau phase remains stable. Second, in the Tet-On system, construct expression occurs even in uninduced

conditions ("leakiness"), albeit at very low level (<1 % of maximal expression) (Stieger et al., 2009). Leak expression of FAD proteins might theoretically cause cellular impairment, but only to a low degree. A comparison between non-transgenic and uninduced imAP neurons using a high-sensitivity method to measure secreted Aβ, such as ELISA, would help to determine the magnitude of leak expression.

AAVS1-imAP iPSC clones were validated for expression of the pluripotency markers TRA-1-81 and SSEA4 (Thomson et al., 1998). Ectoderm differentiation capacity was sufficient for the purposes of this thesis, therefore differentiation into meso- and endoderm were not tested again, since the parental line was fully validated. Differentiation potential in all germ layers can be tested by undirected differentiation and staining of germ layer-specific markers (e.g. TUBB3, SMA, AFP), teratoma formation in immunosuppressed mice, or via transcriptome profiling methods like Scorecard or Pluritest (Müller et al., 2011, Tsankov et al., 2016). Due to the subcloning of inserted cells and microevolution effects during iPSC cultivation, enrichment of genomically aberrant cells is an inherent risk for cell lines including pluripotent stem cells (Blasco et al., 2011, Oliveira et al., 2014, Rebuzzini et al., 2015). Therefore, AAVS1-imAP iPSC clones used for further work were validated for genomic integrity by SNP analysis, and aberrant clones were discarded. SNP analysis determines the copy number of common single-nucleotide variants to infer the presence of, duplications, deletions and loss of heterozygosity at a resolution greater than G-banding, but cannot detect balanced chromosomal rearrangements (Pfeifer et al., 2006). In conclusion, the AAVS1-imAP iPSC clones used in this study were validated according to current standards and successful targeting of the imAP cassette into both alleles of the AAVS1 site could be shown.

4.2. AD-transgenic neural stem cells give rise to authentic neurons with inducible transgene expression

When Choi and colleagues first established a 3D model of human AD, they employed immortalized NPCs carrying the V-MYC oncogene to promote extensive passaging and prevent cell death (ReN cell VM). Problematically, MYC transcription factors influence about 15 % of all human genes, and in a non-linear manner (i.e. weakly expressed

genes are moderately upregulated, highly expressed genes are strongly upregulated) (McMahon, 2010). Taken together, V-MYC overexpression might skew AD-related pathophenotypes through unphysiologically gene expression profiles, abnormal stress tolerance and prevention of neurodegeneration. Authentic non-transformed human cells, such as iPSC-derived NPCs clear the way for a physiologically more relevant model that is not impeded by oncogene expression. The first step towards exploiting this option is to look at neurons, the most affected cell type in AD. Today, there is a wide range of protocols to generate different neuronal subtypes, i.e. general cortical, cortical excitatory, cortical inhibitory, mid-hindbrain or cerebellar (Koch et al., 2009, Muguruma et al., 2015, Shi et al., 2012, Yang et al., 2017, Zhang et al., 2013). However, an extensive body of literature addresses contributions from astrocytes, microglia or macrophages to AD as well (Gate et al., 2010, Grathwohl et al., 2009, Söllvander et al., 2016).

For this study, AAVS1-imAP iPSCs were differentiated into long-term self-renewing neuroepithelial-like stem (lt-NES) cells with mid-hindbrain regional identity (Koch et al., 2009). This stable intermediary population provides standardized starting conditions for further differentiation and displays rosette morphology indicative of a late neuro-ectodermal stage in development with pronounced cell polarization and apical tight-junction formation (Elkabetz et al., 2008).

Upon growth-factor withdrawal, lt-NES cells differentiated as expected into both GABAergic neurons and glial cells as previously described (Falk et al., 2012, Koch et al., 2009). During 3D differentiation at very high density, the medium acidification rate remained constant over time and between treatment conditions, indicating good cell viability similar to descriptions of RenVM-based 3D cultures (Choi et al., 2014, Kim et al., 2015). Notably, using cell count per area introduces a major caveat: Nuclear or immunostainings for e.g. neuronal markers do not yield reliable results due to the very high cell density. Therefore, quantifications of micrographs were normalized to area rather than cell count since data in this thesis shows that cultures were very homogenous and stable in terms of neuronal marker expression (TUBB3). Nonetheless, future studies should explore alternative methods for normalization, such as stereological approaches established for quantifications in tissue slices. When induced with doxycycline, mCherry fluorescence accumulated over approximately two weeks.

Since mCherry is situated two IRES sequences downstream of the APP start codon, lower expression strength compared to cap-dependent translation and increased time-till-plateau was expected (Mizuguchi et al., 2000). Preliminary dot blot experiments on 2D cultures indicated a plateau in Aβ release 24 - 48 h after doxycycline exposure (data not shown). Accordingly, Aβ is efficiently generated in three-dimensional cultures from the first week of induction through the full cultivation period. Thus, matching earlier reports, differentiation along the neural lineage did not cause silencing of the imAP-cassette, and cellular morphology was unaltered. A time-course analysis of Aβ secretion, e.g. by ELISA, might help to explore the Aβ generation dynamics in greater detail. The Tet-On system is known to exhibit low-level transcription even in the absence of doxycycline. This effect was not visible in fluorescence imaging, but might be detectable in western blotting. Thus, a comparison between non-transgenic and imAP12 cultures from the same donor background could yield more precise measurements of relative Aβ release.

In summary, neural precursor cells generated from imAP iPSCs were compatible with the 3D matrix culture, differentiated readily into neurons and astrocytes, and could be induced to release elevated Aβ levels upon doxycycline treatment.

4.3. 3D matrix cultures entrap Aβ and enable aggregate formation

Elevated Aβ production in transgenic neural cells and entrapment of Aβ in the gel matrix are the central premises of three-dimensional gel cultures. In 2D cultures, doxycycline induction increased $A\beta_{40}$ levels in the supernatant 5-fold and $A\beta_{42}$ levels 40-fold with an overall 8-fold increase of the $A\beta_{42/40}$ ratio (from 0.1 to 0.8). An increased $A\beta_{42/40}$ ratio is associated with a drastic increase in pathogenicity (Choi et al., 2014, Selkoe et al., 2016, Shi et al., 2012, Kwak et al., 2020). When comparing the ratio of Aβ generation in control and transgene expressing cells between this and the 2014 study, the increase in $A\beta_{40}$ generation was twofold less than previously reported using the same transgenic cassette, but the $A\beta_{42}$ increase strongly surpassed earlier results approximately fourfold (Choi et al., 2014). As different normalization methods were used, the absolute values are not directly comparable. The most recent study from the Kim lab employing clonal

immortalized FAD-transgenic cells analyzed downstream pathology in response to $A\beta_{42/40}$ ratios from 0.05 to 1.4 (Kwak et al., 2020). The authors found that the $A\beta_{42/40}$ ratio is the strongest determinant of tau pathology and cytotoxicity, whereas total $A\beta$ did not correlate closely. Thus, the presented system with an $A\beta_{42/40}$ ratio of about 0.8, a value well inside the tested range (0.05 to 1.4), is expected to induce moderate downstream pathology. Due to putative Tet-On leakiness, the increase of the $A\beta_{42/40}$ ratio might be even larger when compared to non-transgenic instead of uninduced controls. At the same time, construct expression from the safe harbor is highly standardized due to the clonal nature of the line with exactly two transgene copies per cell and more stable due to the safe-harbor localization of the transgene cassette. Thus, the presented system provides a robust and more standardized experimental platform than high-expressing RenVM cells that require repeated enrichment by FACSorting every few passages, and is easier to shield from genomic aberrations from extensive subcloning (Kim et al., 2015, Kwak et al., 2020). Comparing $A\beta$ levels in the supernatant of 2D and 3D cultures via western blotting and ELISA showed that induction massively elevated $A\beta$ levels in 2D supernatants. Since no such increase was detected in 3D culture supernatants with the same cell count, medium volume and incubation time, this suggests that $A\beta$ most likely gets entrapped in the gel.

Indeed, $A\beta$ precipitation in the gel matrix was discovered by autofluorescence from amyloid deposits, in analogy to how amyloid plaques and vascular amyloidosis can be detected by fluorescence microscopy (Kwan et al., 2009). $A\beta$ autofluorescence is specifically excited by UV light in the 360 – 430 nm range with a broad emission peak around 525 nm. Thin-layer 3D cultures are amenable to autofluorescence measurements during the cultivation period by automated whole-well imaging, and autofluorescent material could be readily detected in induced cultures, although the nature of the deposited material is not clear. Surprisingly, the depositions became noticeable after only one week of induction, plateaued after approximately three weeks and remained unchanged for the remainder of the experiment. Anti-$A\beta$ staining at six weeks of treatment specifically labeled the most autofluorescent regions. In addition, highly autofluorescent regions were free of mCherry reporter fluorescence, suggesting that these areas are cell-free. In the light of earlier experiments that showed robust $A\beta$ generation in imAP12 neurons upon induction and efficient $A\beta$ entrapment in the gel

matrix, the autofluorescence and immunoreactivity to Aβ-specific antibodies indicate Aβ deposition. Considering the timeline, it seems likely that these are oligomeric or protofibrillar species. Either immunostaining with oligomer-specific antibodies or non-denaturing western blot analysis could be used to validate this assumption. However, it is unclear why depositions occur in particular locations. In retrospect, the deposition sites can be identified prior to induction via autofluorescence and do occur in uninduced cultures as well, yet without any deposition within the experimental time frame. These structures might be matrix inhomogeneities resulting from the gel matrix itself, or sites of particular matrix composition. Using different matrix materials might shed light on the required chemical or structural features for amyloid entrapment, and could thus be helpful towards i.e. blocking sites of Aβ precipitation to promote clearance. For example, defined hydrogels like PuraMatrix are biocompatible, yet very reductionist. Such a matrix could be used as a test scaffold for various ECM proteins to elucidate their effect on amyloid deposition. For example, heparansulfate proteoglycans (HSPGs) have been implicated in amyloid formation in mouse models of AD (Liedmann et al., 2012, Liu et al., 2016, Thonhoff et al., 2008). In brief, induction of imAP12 cultures for six weeks increased Aβ-related pathogenic parameters like total $A\beta_{40}$ and $A\beta_{42}$ and the $A\beta_{42/40}$ ratio, while 3D cultivation enabled efficient Aβ entrapment visualized by deposit formation.

4.4. Aβ-generating cultures form SDS-insoluble Aβ aggregates

After detecting extensive Aβ accumulations in induced 3D matrix cultures, the nature of these accumulations was further probed using β-sheet-specific chemical dyes and Aβ-specific antibodies. Traditional dye stains, for example Congo red, are still commonly employed for neuropathological diagnosis of AD. Congo red integrates into a longitudinal groove on mature amyloid fibrils. After staining, plaques show a characteristic pink color in bright field images, and "apple-green" birefringence when viewed with two orthogonal polarizing filters. However, this detection method was optimized for 5 - 10 μm paraffin sections, whereas thin-layer 3D cultures are 100 – 200 μm thick. In the latter case, stained structures appear black before and after staining due to their high optical density. Problematically, the typical fibrous microstructure is not

visible and it is impossible to judge whether specific staining was achieved. This issue was circumvented by relying on Congo red fluorescence upon excitation with 555 nm light (Clement et al., 2014). Sequential staining of autofluorescent amyloid aggregates with Congo red and its derivative Methoxy-X04 clearly demonstrated specific binding and fluorescence in optically dense aggregate structures that was not present prior to staining and exclusive to the fluorescence channel associated with the respective dye. Further examination of induced thin-layer 3D cultures after six weeks of treatment revealed numerous tightly packed, fibrous, specifically autofluorescent and ThT-reactive structures in the 5 – 100 µm size range, therefore matching typical criteria for the identification of extracellular Aβ aggregates (Serrano-Pozo et al., 2011). This was further confirmed by co-staining of the aggregate structures with Aβ-specific antibodies and amyloid dyes. Notably, the listed conditions applied to dense aggregates that were also visible in phase contrast. However, other diffuse structures were detectable in Aβ immunostainings, but not in Thioflavin T-stainings or in phase contrast. Thus, the first type resembles "dense" or "cored" plaques, while the second appears as diffuse Aβ aggregates in induced imAP12 3D cultures (Serrano-Pozo et al., 2011).

In high-magnification confocal images, structurally distinct zones inside β-sheet aggregates became apparent. Central regions contained fibrous material, whereas the periphery was rich in globular structures, a feature that has been described in numerous publications (Blazquez-Llorca, 2010, Kwan et al., 2009, Serrano-Pozo et al., 2011). Imaging of UV-induced autofluorescence together with Thioflavin T staining clearly demonstrates a near-perfect overlap in fibrillar areas in the core of the aggregate, whereas no ThT staining is found in globular or amorphous peripheral regions of the aggregate that are, nonetheless, autofluorescent. This result is of two-fold importance. First, it demonstrates the high affinity of ThT to amyloid fibrils in contrast to amorphous aggregates. Second, different aggregation stages coexisting confirm the model of local hyperaccumulation leading to sequential and progressive formation of larger aggregate structures (Finder et al., 2007). The outer edges of *in vivo* plaques in mouse models frequently spread tendril-like extensions into the surrounding tissue (Bussière et al., 2004). Most amyloid aggregates detected in this model did not display tendril formation and resembled the "burned-out" morphology, i.e. small, dense and asymmetrically structured plaques without a surrounding corona of cobweb-like fibrils. However, in few

cases unipolar tendril formation was observed in MX04-stained aggregates after long exposures. Plaques often display similarly dense and irregular morphologies. For future experiments, analyzing the contribution of different matrix materials and cell seeding patterns on the localization, growth pattern and final shape of aggregates in this model might help to uncover why plaque formation occurs specifically in some brain regions.

Thick-layer 3D cultures were employed to study the biochemical features of the deposited Aβ. Local Aβ accumulations were detected just like in thin-layer cultures. To visualize the 3D deposit distribution, we adapted an existing protocol for tissue clearance for whole mouse brains to thick-layer matrix cultures (Schwarz et al., 2015). Acquisition of a whole thick-layer culture in light-sheet imaging demonstrated a homogeneous distribution of numerous small and few large Aβ-positive structures. Protein samples from 4-months-old thick-layer cultures contained elevated Aβ levels in TBS- and SDS-insoluble fractions, indicating strongly aggregated amyloid material. SDS-insoluble Aβ is a specific feature of human AD (Kalback et al., 2002, Kuo et al., 2001). For future studies, analyzing various chemical parameters of Aβ peptides and aggregates in 3D cultures might reveal how insolubility in 3D cultures can be mechanistically explained, especially concerning degradation of the Aβ peptide termini and posttranslational modifications. In AD patients, plaques contain only little, if any, full-length $A\beta_{40}$ and $A\beta_{42}$. Instead, the peptides are N-terminally truncated and pyroglutamylated, likely from partial degradation (Kuo et al., 2001). To get a better understanding of the composition and ultrastructural configuration of the aggregates in the presented cultures, further analyses, such as electron microscopy for the morphological features and purification of the aggregates followed by mass spectrometry to analyze the chemical composition might prove worthwhile.

In the present system, AD-associated pathogenic variants of APP and Presenilin-1, both functionally relevant proteins in neurons, are highly expressed to boost Aβ generation. To confirm that any phenotype is a consequence of excessive Aβ generation, APP processing to Aβ was blocked in induced cultures via γ-secretase inhibition. As expected, induced cultures formed numerous Aβ particles, but blocking Aβ generation prevented particle formation almost completely. These data match the results of our previous study (Choi et al., 2014). It should be noted that the most common strategy to block APP processing – application of γ-secretase inhibitors – is fraught with unspecific

side effects on vital neuronal signaling pathways, especially Notch (Borghese et al., 2010). Therefore, DAPT-treated cultures exhibit a different cellular composition compared to non-DAPT-treated controls, such as a lower fraction of glial cells. Interestingly, γ-secretase inhibition was associated with reduced stability of the gel matrix. DAPT-treated cultures more often detached from the well wall and contracted into a spheroid-like shape. As contracted cultures were subject to different conditions than non-contracted cultures, they were excluded from all analyses. Surprisingly, addition of murine astrocytes prevented culture contraction completely (Christian van 't Hekke, internship report). Therefore, astrocytes might play a vital role in culture integrity, and, accordingly, compounds that modulate the APP processing of γ-secretase instead of blocking all of its activity (SGSM41, RO4929097), or β-secretase inhibitors might prove useful as more specific tools in future experiments.

To summarize, induced 3D cultures contained structures resembling plaques with respect to morphology, autofluorescence and specific dye reactivity. But more importantly, the presence of SDS insoluble Aβ indicates that 3D matrices not only entrap Aβ monomers, but also promote Aβ aggregation. This suggests that induced 3D cultures might contain large reservoirs of toxic Aβ oligomers and protofibrils.

4.5. Aβ-dependent progressive tau phosphorylation culminates in tau aggregate deposition

Tauopathy is the second major hallmark of Alzheimer's disease and typically appears after the onset of amyloidosis. Afflicted neurons undergo a progressive phosphorylation of the microtubule-associated protein tau at a variety of epitopes, referred to as "hyperphosphorylation". The additional negative charges detach hyperphosphorylated tau proteins from the microtubule network, which seems to lead to p-tau enrichment in the somatodendritic segment. One current hypothesis assumes that tau is phosphorylated in response to postsynaptic calcium elevation via Aβ oligomer binding to the prion protein receptor (PrPc) and activation of the downstream tyrosine kinase Fyn (Crews et al., 2010, Kaufman et al., 2015). Another states that tau hyperphosphorylation is a cellular response to Aβ toxicity, with p-tau being an integral component of stress-granule formation (Ash et al., 2014). RNA stress granules contain high concentrations of

hyperphosphorylated tau that is thought to carry a stochastic risk of forming a p-tau aggregate seed that can later spread (Apicco et al., 2018, Vanderweyde et al., 2016).

In the present study, first indications of elevated tau phosphorylation could be detected after six weeks of dox treatment. P-tau accumulation progressed with longer cultivation and affected most neurons in 4-months-treated cultures. Since increasing tau content is not only a sign of neuronal pathology, but also a feature of normal neuronal maturation, overall culture reactivity to tau or p-tau antibodies is not a specific parameter for pathogenic changes (reviewed in Bodea et al., 2016). In contrast, pathologic p-tau is well known to translocate from the axon to the somatodendritic compartment, or to accumulate in short stretches of cellular processes (Perl, 2010). Interestingly, in our model only dox-induced cultures displayed somatic or somatodendritic p-tau accumulation. High-resolution imaging uncovered dysmorphic, strongly p-tau positive segments of processes as well as neurons with characteristically misshapen cell bodies, matching histopathological findings in AD patient brains (Blazquez-Llorca, 2010). Since soma shape was highly variable, only strongly p-tau positive cellular processes could be quantified to reveal a five-fold increase of p-tau positive segment length in induced over uninduced cultures. Additionally, treatment with a γ-secretase inhibitor prevented the appearance of p-tau positive processes almost completely, suggesting that p-tau pathology strongly depends on Aβ accumulation. The same pattern applied to the number of strongly p-tau positive process segments.

Further markers of neuronal dystrophy in Alzheimer's disease include p-tau "husks", dystrophic neurites, and axonal swellings. Together, they indicate progression from amyloidosis to the onset of neurodegeneration. Husks are p-tau leftovers from perished neurons that outline the shape of the original cell. Although rare, several husks were detected in 3D cultures as early as after six weeks of dox treatment. Classically, dystrophic neurites are characterized by bulbous end-terminals in close proximity to amyloid plaques. In induced cultures, areas of reduced neurite density occasionally surrounded autofluorescent deposits. Neurites in these areas appeared dystrophic and swollen. Notably, these neurites were negative for p-tau. In addition, however, numerous neurite terminals without close deposits were enlarged and stained strongly for p-tau, similar to p-tau positive cells in the brain interstitium.

Tauopathy is associated with impairments in various cellular functions, among others in trafficking of proteins and metabolites (Bodea et al., 2016). Axons in induced cultures showed single, swollen distensions that were stained strongly by p-tau antibodies similar to a previous report of *in vitro* tauopathy that employed overexpression of an aggregation-prone pseudo-hyperphosphorylated tau mutant (Mertens et al., 2013). These swellings likely result from material build-up due to transport defects. To follow up, scrutinizing microtubule integrity in the vicinity of the swellings might reveal whether cytoskeleton degradation is involved. Alternatively, measuring mitochondrial motility in live cultures might probe the axonal transport impairment.

Apart from localization, the defining parameter of neurofibrillary tangles is the aggregated state of p-tau culminating in fibril formation. To address this issue, we first analyzed the size distribution of p-tau aggregates using semi-denaturing gel electrophoresis of protein samples from 6-weeks-treated cultures and found that p-tau formed larger aggregates in induced cultures, similar to findings in a mouse model of human tauopathy (Schoch et al., 2016). In the majority of induced cultures, SDD-AGE showed signals at the site of the pocket, hinting at very large aggregated species. It should be noted that SDD-AGE does not result in clean band patterns, but rather in high-molecular weight smears that extend further up the more aggregated the target protein has been. Still, immunohistochemical staining against the fibril-specific "paperclip conformation" epitope of p-tau (MC-1) did not yield visible reactivity in 6-weeks-old cultures (data not shown), suggesting that p-tau aggregates, but no mature fibrils are present at this time point. To confirm this finding, electron microscopy might provide further insights into the structure of the well-bound p-tau aggregates. For this purpose, cell lysates are sequentially fractionated to yield sarkosyl-insoluble material that is then immunostained against tau with gold-labeled antibodies. This way, the typical paired helical filament (PHF) structure of mature p-tau fibrils can be visualized. In contrast, the same procedure in intact cells could show the presence of highly ordered, longitudinally aligned fibrils in neuronal somata. It would also be interesting to determine the splice isoforms of tau that are generated and aggregated in induced and uninduced cultures, because different isoforms are associated with characteristic aggregation patterns and diseases like AD or Pick's disease (Bussiere et al., 2000). Since the adult human brain contains similar levels of shorter (3R) and longer (4R) isoforms, whereas fetal brains

almost exclusively show 3R, specific antibody stainings, western blot analysis or qPCR could help to better understand the maturity of the cultures and to characterize tau composition. It has recently been reported that splicing of the 4R tau isoform can be enforced and is highly toxic to mouse neurons (Schoch et al., 2016). The same method could be applied to human cells in this model to explore the contributions of various tau isoforms on pathology initiation and progression.

Taken together, induced 3D imAP12 cultures develop progressive p-tau pathology between six weeks and four months of dox treatment, starting with immunoreactivity against phosphorylated tau epitopes, and culminating in accumulation of high-molecular weight aggregates, and neuronal dystrophy. Chemical inhibition of γ-secretase prevents these phenotypes which suggests that the p-tau pathology in this model is Aβ-driven.

4.6. P-tau in induced cultures recapitulates mature fibril pathology *in vitro*

To elucidate whether longer cultivation promotes the formation of more mature p-tau aggregates cultures were treated with dox for up to four months. Strikingly, various autofluorescent deposits were surrounded by dystrophic neurites that stained positive for aggregated p-tau in a fibril-specific conformation. The MC-1 antibody-reactive structures encompassed both swollen and regularly shaped neurites, partly overlapped with autofluorescent deposits and were strongly Thioflavin T-reactive. Beyond the immediate vicinity of deposits, a fraction of neurons displayed MC-1 immunoreactivity in the somatic and neuritic compartments. As described in previous studies in AD brain slices, strongly MC-1-positive cells typically occurred one at a time, surrounded by negative cells, although occasionally strands of axons were slightly MC-1-reactive as well (Blazquez-Llorca, 2010). The absence of MC-1 immunoreactivity from the DAPT-treated condition strongly suggests the dependence of the p-tau pathology on Aβ generation. Taken together, these results establish that both amyloid and p-tau pathologies match the human *in vivo* situation in numerous key parameters and can be elicited by elevated Aβ secretion alone. Additionally, the presented model supports the amyloid cascade hypothesis insofar as both major AD hallmarks occur sequentially and progressively and that inhibiting γ-secretase can effectively prevent both phenotypes (Selkoe et al., 2016).

4.7. High Aβ levels lead to mitochondria pathology including impaired respiratory capacity

The severe p-tau pathology prompted further investigation of functional impairments in dox-treated cultures, such as mitochondrial metabolism. Mitochondrial impairment is a key factor in the development and progression of various neurologic disorders including AD, yet it has been largely ignored in existing *in vitro* models of AD (Borger et al., 2011, Choi et al., 2014, Lin et al., 2006, Shi et al., 2012). Neurons have to satisfy the substantial energy demands of their physiological functions mostly relying on oxidative phosphorylation, such as establishment and maintenance of the membrane potential and the large and complex neuronal architecture itself (Bélanger et al., 2011, Hall et al., 2012). Accordingly, mitochondrial impairment can severely affect neuronal function and survival. Since mitochondria depend on the efficient import of cytoplasmic proteins and metabolites, this organelle is highly sensitive to changes in cellular proteostasis and any interference with transport mechanisms across the mitochondrial membrane as well as mitochondrial localization, i.e. along the axon (López-Crisosto et al., 2015, Paasch et al., 2018).

A p-tau-positive subset of neurons in dox-induced 3D cultures demonstrated a fragmented mitochondrial phenotype with reduced average network size and an increased number of singular mitochondria. It should be noted that the overall number of large networks was unaltered in dox-induced cultures. These data support the idea that accumulated mitochondrial damage forces increased shedding of defective mitochondria (Ni et al., 2015). However, the effect was only detectable in cells with robust p-tau staining in the somatodendritic segment. This finding points to two important conclusions. First, only a small subset of cells is affected by strong changes to mitochondrial morphology, pending further analysis to detect more subtle morphological differences. While there is no indication whether the relationship between tau and mitochondria is causal or correlational, future research might pick this thread up for further mechanistic exploration. For example, some reports claim that Aβ can directly interact with mitochondrial membrane pore complexes and intra-mitochondrial proteins, triggering mitochondrial proteome imbalances (Cenini et al., 2016, Devi et al., 2010). Analyzing mitochondrial import in our AD model might help to validate this hypothesis.

Second, our model could serve as a testbed for therapeutic interventions aimed at mitochondria, for example via pharmacological inhibition of mitochondrial fragmentation. This strategy has been shown to rescue neurotoxicity in a mouse model of AD, and would be an ideal candidate to be validated in a human model (Wang et al., 2017).

Since mitochondrial fragmentation is an indicator of functional decline, we performed a Seahorse analysis to measure respiratory capacity (Borger et al., 2011, Lin et al., 2006). This inquiry revealed that after normalization to non-mitochondrial respiration dox-induced cultures demonstrated similar respiration compared to controls under baseline conditions, but the maximum respiratory rate was significantly reduced. This means that mitochondria in induced cultures cannot provide as much energy, e.g. during neuronal activity. Finally, permanent inhibition of Aβ generation normalizes the maximum respiratory rate even in the presence of doxycycline, showing that neither doxycycline nor the overexpression of fAD transgenes is likely to be responsible for the pathophenotype. As shown above, mitochondrial fragmentation affected only a small subset of neurons, suggesting that functional impairment precedes network degradation. To find out whether the altered morphology and respiration reflect changes in protein expression, key respiratory chain proteins were assessed in dox-induced cultures compared to uninduced controls and Dox+DAPT-treated cultures. Notably, all of those proteins are encoded in the nucleus and do not depend on mitochondrial translation machinery. Therefore, they are likely unaffected by the doxycycline treatment. The complex I component NDUFB8 was reduced by approximately 60 % and complex IV subunit I by 25 %. Complexes I and IV generate the proton gradient across the inner mitochondrial membrane, accordingly this finding might explain the reduction in respiratory capacity measured before (Kühlbrandt, 2015). A reduction in the proton gradient directly affects ATP generation by complex V. Since mitochondrial respiration is the major neuronal energy source, the impairment cannot be compensated easily and might cause various downstream problems, such as collapse of energy-dependent mechanisms (membrane potential, transport, etc.) or increased oxidative stress. The complex I deficit described here can be interpreted twofold, as there are numerous and conflicting results from previous rodent and human studies. Rats have shown improved mitochondrial respiration when complex I functionality was supplemented with the small compound idebenone in a study from the Fujita lab, yet the Trushina group

demonstrated the improved cognition in AD mouse models by mild inhibition of complex I (Sugiyama et al., 1985, Zhang et al., 2015). On the contrary, the Choi group found an acceleration of amyloid toxicity upon complex I inhibition in mice (Joh et al., 2017). Incidentally, the replacement strategy via idebenone has failed to show any effect in AD patients (Thal et al., 2003).

Doxycycline has been reported to affect the mitochondrial translation at concentrations from 0.5 to 20 µg/ml (1 µg/ml was used in this study), an effect that could seriously obscure mitochondrial measurements (Chatzispyrou et al., 2015). Yet, while dox-treated cultures displayed significantly lower non-normalized OCR than controls at all time points, Dox+DAPT-treated cultures and controls were statistically indistinguishable, indicating that the mitochondrial pathology is Aβ- but not Dox-driven. Additionally, the maximum OCR of 2D-cultivated lt-NES-derived neurons showed no dose-response relationship when the cells were treated with doxycycline concentrations ranging from 0 to 20 µg/ml for one week. These findings demonstrate that doxycycline did not confound the mitochondrial phenotype shown here in a detectable fashion. Thus, the reduced oxygen consumption curve in dox-treated cultures is likely a reflection of the cytotoxic Aβ and p-tau pathologies. The analyses shown here accounted for different cell numbers in different conditions by comparing normalized OCR curves. Future experiments should take cell numbers and viability at the time of Seahorse analysis into consideration, e.g. via post-hoc assessment of DNA content in each well. Other potential confounders, such as changes to the neuron-glia ratio, altered neuronal subtype composition, cell size, complexity, maturity, or synapse count were not addressed. Ideally, the analyzed cultures should be characterized at cellular level, either by panels of immunostainings and FACS analysis, or by single cell RNA sequencing to determine the exact identities and developmental trajectories of the cells.

The fragmentation of the mitochondrial network, the impaired respiratory chain protein balance and the reduced maximum respiratory rate might be complex but powerful readouts to illuminate the relationship of Aβ, p-tau and mitochondria in this AD model as proposed earlier. Therefore, further exploration of this mitochondrial dysfunction phenotype is a promising goal for future use of the model system, especially in the context of conflicting data from rodent models and AD patients.

4.8. Elevated Aβ levels increase cellular stress

Induced three-dimensional cultures display significantly elevated levels of markers for DNA damage and apoptosis, compared to uninduced or DAPT-treated cultures. The mitochondrial pathology might be a link between the Aβ and DNA damage due to calcium release and generation of reactive oxygen species (ROS) in dysfunctional mitochondria (Bonda et al., 2011). ROS accumulation can drive both DNA damage and, further downstream, apoptosis (Mukherjee et al., 1995). To confirm this pathway, ROS production should be evaluated, for example using ROS-sensing dyes like MitoSOX or CellROX. If increased ROS production is found, the DNA damage and apoptosis might be averted by antioxidant treatment, e.g. trolox (Forrest et al., 1994). The final stage of Alzheimer's disease features extensive neuronal loss and cognitive decline. Up to this point, Aβ-based mouse models have consistently failed to recapitulate widespread neurodegeneration, while studies involving particular humanized tau isoforms showed tremendous neurotoxicity (Sasaguri et al., 2017, Schoch et al., 2016). These reports make clear that mouse physiology is unsuitable to comprehensively model AD, although mouse models have undeniable merits to elucidate particular subsets of the pathology. *In vitro* models, on the other hand, suffer from artificial cell populations being highly resistant to cell death due to oncogene expression or insufficiently strong pathology for late-stage disease modeling (Choi et al., 2014, Shi et al., 2012). Immortalized neural cells that have been used in a previous study did not show substantial cell death, likely due to V-MYC overexpression, which means that the new iPSC-based model is a considerable step forward towards modeling neurodegeneration in AD. Most importantly, it can be concluded that the cell death phenotype is purely Aβ-dependent, similar to the Aβ and p-tau aggregation phenotypes. Interestingly, markers of tauopathy and apoptosis were generally not co-stained in the same cells. This observation seems counterintuitive at first sight, yet it is a matter of intense debate whether apoptosis actually is the major mode of neuronal decline in AD. While cell death was classically divided into apoptosis and necrosis, more recent research untangled further subdivisions such as necroptosis or pyroptosis (Kroemer et al., 2009, Tait et al., 2014). All of those have specific roles that are often associated with innate immune defense, and might play a role in a variety of neurodegenerative disorders (Richards et al., 2016). Accordingly, in-detail analyses of

the cell death mechanisms involved in the present AD model could help to determine the particular subtype(s) of cell death being recapitulated, their respective relationships to other elements of the AD pathology such as amyloid plaques or p-tau accumulation, as well as to dissect the involvement of other cell types like astrocytes, oligodendrocytes or microglia on neuronal decline. For example, necroptosis could be detected via immunostaining against phosphorylated (activated) mixed lineage kinase domain like pseudokinase (MLKL), whereas pyroptosis can be detected by measuring cleaved gasdermin D in western blot analysis (Cai et al., 2013, He et al., 2015).

In the present model, the authenticity of the neurons and the purely Aβ-dependent cascading phenotype development enable progressive neurotoxic effects. Cellular stress as indicated by DNA damage and apoptosis in induced imAP12 cultures is directly linked to Aβ generation and can be prevented by inhibition of γ-secretase, although the effect on other pathways of neuronal degeneration remains to be explored.

5. Outlook

Due to its amyloid-β-driven pathogenic cascade, this new model can serve as a platform to scrutinize the mechanistic connection between amyloid and tau pathology. For example, amyloid deposition and p-tau pathology do not overlap well in AD patients. Establishing a series of connected 3D cultures might enable analyses of amyloid seeding effects on distal populations and tau pathology. Due to the inducible nature of the new model, the amyloid pathology can be triggered in relatively mature neurons, thus avoiding developmental confounders. This is useful to study e.g. synaptic maintenance and long-term potentiation, electrical activity in neurons and astrocytes, and influence of the Aβ dose on pathology progression. Currently, all cells in the model generate Aβ, but future iterations could spike in non-transgenic cells to specifically focus on non-cell autonomous effects. Furthermore, since the transgene can be switched off again, time-course analyses could shed light on the ability of neural tissue and single cells to recover from Aβ-induced damage. For example, will amyloid plaques dissolve once Aβ generation is ended? Is a p-tau-positive cell irrevocably lost, or can it recover? Does network activity normalize again? These questions are highly relevant for therapy development. If there is a "point of no return" in AD, therapeutic approaches that

suppress pathology development were bound to fail in diagnosed patients. Moving forward, the model is an interesting candidate for revalidating drugs that succeeded in mouse trials, but failed in humans. It can be used to shed light on the physiological differences between the two species with regard to neurodegeneration and might clarify the limits of animal models. Since p-tau pathology develops without tau-impacting transgenes, it will allow compound discovery to target the link between the amyloid and p-tau pathology in order to find drugs that previous, amyloid-focused screenings might have missed.

In its current state, the inducible 3D model might be too reductionist to address questions of damage repair and regeneration that rely on additional cell types like microglia and oligodendrocytes. Microglia are vital to brain homeostasis and neuroinflammation, but, since they are derived from a non-neural lineage, they have to be added separately. Oligodendrocytes typically protect axons from unwarranted microglial toxicity, but are not efficiently generated in lt-NES-derived cultures. However, the modularity of the 3D gels allows virtually limitless control over cellular composition. Microglia have been shown to invade comparable gel systems, and it might be possible to include oligodendrocyte precursor cells when casting the gel matrix. Neuronal and astrocytic populations could be tailored using forward programming techniques, i.e. forced expression of fate-determining transcription factors to rapidly generate a target cell population from stem cells, to achieve a particular excitatory to inhibitory ratio. This way, the model can be adapted to the required degree of complexity for analyses of network activity (spontaneous activity, degree of connectivity, synchronicity, calcium waves).

The mode and degree of amyloid aggregation has been shown to depend on the extracellular matrix composition. During human aging, ECM composition changes and stiffness increases. While it is unclear whether these alterations promote brain pathology, this human 3D model could be modified to use alternative hydrogel matrices to explore the impact of matrix components (e.g. heparansulphate proteoglycans) or physical parameters (stiffness, porosity) on amyloid deposition. Using materials that are less prone to degradation might help to prevent the problem of culture contraction. Also, replacing Matrigel/Geltrex with a xeno-free synthetic matrix would further improve standardization and reproducibility.

Finally, introducing this model system into an *in vivo* environment, e.g. via transplantation of matrix-cell mixtures into mouse brains, might provide several benefits. The physiological environment would enable longer cultivation paradigms and likely promote maturation and functionalization of the transplanted cells. The phenotype in the transplant could also be modified by implantation into e.g. FAD or mutant tau overexpressing mouse strains. In addition, the transplant would be localized behind a functional blood-brain barrier for e.g. drug testing or metabolic studies.

6. Summary

Alzheimer's disease (AD) is the most prevalent neurodegenerative disease that is poised to affect an increasing part of the population as life expectancies are on the rise. AD leads to extracellular deposits of amyloid β (Aβ plaques) in the brain, followed by hyperphosphorylated tau (p-tau) in neurons, and eventually neurodegeneration. The "amyloid hypothesis" states that aggregation-prone Aβ species like $A\beta_{42}$ trigger all downstream pathology. This project aimed to establish a non-transformed human neuron-based 3D model of extracellular amyloid pathology and to analyze the resulting molecular and cellular phenotypes. To elevate Aβ secretion, human induced pluripotent stem cells (iPSCs) were engineered to overexpress the amyloid precursor protein (APP) carrying two AD-promoting mutations, and a pathogenic presenilin-1 (PS-1) variant lacking exon 9 (PS-1ΔE9). To ensure control over gene dosage, the cassette is expressed from the AAVS1 genomic safe harbor locus upon induction with doxycycline. A clone with biallelic integration (imAP12) was validated by multiplex PCR genotyping, pluripotency marker expression and SNP genotyping. This clone was then differentiated to long-term self-renewing neuroepithelial-like stem (lt-NES) cells. These imAP12 lt-NES cells were differentiated into neurons and astroglia in thin- and thick-layer 3D gel matrix cultures by growth-factor withdrawal.

Doxycycline-induced neuronal cultures exhibited constant transgene expression for at least 4 months as judged by an mCherry reporter and released 40-fold more $A\beta_{42}$ and 5-fold more $A\beta_{40}$ ($A\beta_{42/40}$ ratio = 0.8) than cultures without doxycycline as determined by ELISA measurements. After 6 weeks of induction, western blot analyses of 2D and 3D culture supernatants indicated that Aβ is quantitatively entrapped in the 3D matrix.

Indeed, UV-induced autofluorescence, a feature of Aβ aggregates, accumulated progressively between the first and sixth week in induced cultures. End-point immunostaining revealed strong colocalization with Aβ deposition. In addition, amyloid dyes like Thioflavin T, Congo red or Methoxy-X04, Amytracker 630 and Aβ-specific antibodies (D54D2) labeled deposits (10 – 100 μm) with filamentous internal structure and characteristic DAPI autofluorescence in induced 3D cultures. 4-months-old induced 3D cultures showed robust accumulation of TBS- and SDS-insoluble Aβ in western blot analyses. Finally, Aβ deposition could be fully prevented by blocking Aβ generation via γ-secretase inhibition.

In parallel, six weeks-treated cultures showed early signs of tau pathology, another major AD hallmark. Induced 3D cultures showed robust and progressive intracellular accumulation of hyperphosphorylated tau (p-tau; antibody AT8) between weeks 6 and 16. Recapitulating typical AD features, p-tau appeared dyslocalized in single neurons as shown by distinct dystrophic morphology including flame-shaped and irregular somata, axonal swellings, degenerated processes and dystrophic terminals. P-tau was present in induced 3D cultures from week 6 as well, and fibrillar tau epitopes (detected with the "paperclip" conformation-specific MC-1 antibody) could be detected after 16 weeks. As expected, p-tau pathology did not develop in the presence of γ-secretase inhibitors.

Cellular energy metabolism was impaired in induced cultures as p-tau-positive neurons displayed hallmarks of mitochondrial fragmentation and lowered respiratory capacity, alongside an overall reduction in essential respiratory chain complexes. This is the first time that these phenotypes have been detected in an endogenous Aβ-based *in vitro* model. Moreover, the presented model recapitulates features of neurodegeneration such as markers of increased stress like DNA double strand breaks and caspase 3 activation. The latter was increased 5-fold in induced cultures and could be fully alleviated via γ-secretase inhibition. These data strongly support the view that the presented model faithfully recapitulates a progressing AD pathology including major disease hallmarks mainly driven by controllable Aβ generation.

7. List of figures

8. References

Akajima ON, Kiyama HA, Eshima RT. Real-Time Polymerase Chain Reaction Method for Detecting Contamination of Beef by Material from Genetically Engineered Cattle. Biol Pharm Bull 2009; 32: 1313–1316

Apicco DJ, Ash PEA, Maziuk B, Leblang C, Medalla M, … Wolozin B. Reducing the RNA binding protein TIA1 protects against tau-mediated neurodegeneration in vivo Daniel. Nat Neurosci 2018; 21(January): 72–80

Arber C, Toombs J, Lovejoy C, Ryan NS, Paterson RW, … Wray S. Familial Alzheimer's disease patient-derived neurons reveal distinct mutation-specific effects on amyloid beta. Mol Psychiatry 2019

Ash PEA, Vanderweyde TE, Youmans KL, Apicco DJ, Wolozin B. Pathological stress granules in Alzheimer's disease. Brain Res 2014; 1584: 52–58

Atagi Y, Liu C-C, Painter MM, Chen X-F, Verbeeck C, … Bu G. Apolipoprotein E Is a Ligand for Triggering Receptor Expressed on Myeloid Cells 2 (TREM2). J Biol Chem 2015; 290(43): 26043–26050

Bailey CC, Devaux LB, Farzan M. The triggering receptor expressed on myeloid cells 2 binds apolipoprotein E. J Biol Chem 2015; 290(43): 26033–26042

Bélanger M, Allaman I, Magistretti PJ. Brain energy metabolism: Focus on Astrocyte-neuron metabolic cooperation. Cell Metab 2011; 14(6): 724–738

Benilova I, Karran E, De Strooper B. The toxic Aβ oligomer and Alzheimer's disease: an emperor in need of clothes. Nat Neurosci 2012; 15(3): 349–357

Blasco MA, Serrano M, Fernandez-Capetillo O. Genomic instability in iPS: Time for a break. EMBO J 2011; 30(6): 991–993

Blazquez-Llorca L. Pericellular innervation of neurons expressing abnormally hyperphosphorylated tau in the hippocampal formation of Alzheimer's disease patients. Front Neuroanat 2010; 4(June): 1–23

Bodea L-G, Eckert A, Ittner LM, Piguet O, Götz J. Tau physiology and pathomechanisms in frontotemporal lobar degeneration. J Neurochem 2016; 138: 71–94

Bonda DJ, Smith M a, Perry G, Lee H, Wang X, Zhu X. The mitochondrial dynamics of AD. Curr Pharm Des 2011; 17(31): 3374–3380

Borger E, Aitken L, Muirhead KEA, Allen ZE, Ainge JA, … Gunn-Moore FJ. Mitochondrial β-amyloid in Alzheimer's disease. Biochem Soc Trans 2011; 39(4): 868 LP-873

Borghese L, Dolezalova D, Opitz T, Haupt S, Leinhaas A, … Brüstle O. Inhibition of notch signaling in human embryonic stem cell-derived neural stem cells delays G1/S phase transition and accelerates neuronal differentiation in vitro and in vivo. Stem Cells

2010; 28(5): 955–964

Bouabe H, Okkenhaug K. Gene Targeting in Mice: a Review. Methods Mol Biol 2013; 1064: 315–336

Bouvier DS, Jones E V., Quesseveur G, Davoli MA, Ferreira TA, … Murai KK. High Resolution Dissection of Reactive Glial Nets in Alzheimer's Disease. Sci Rep 2016; 6(April): 1–15

Bullock R, Borrie M, Ch B, Hager K, Andreasen N, … Siemers E. Trial of Solanezumab for Mild Dementia Due to Alzheimer's Disease. N Engl J Med 2018; 378(4): 321–330

Bush AI, Tanzi RE. The galvanization of b-amyloid in Alzheimer's disease. PNAS 2002; 99(11): 7317–7319

Bussière T, Bard F, Barbour R, Grajeda H, Guido T, … Buttini M. Morphological Characterization of Thioflavin-S-Positive Amyloid Plaques in Transgenic Alzheimer Mice and Effect of Passive Aβ Immunotherapy on Their Clearance. Am J Pathol 2004; 165(3): 987–995

Bussiere T, Buee L, Hof PR. Tau protein isoforms, phosphorylation and role in neurodegenerative disorders 1. Brain Res Rev 2000; 33: 95–130

Cai Z, Jitkaew S, Zhao J, Chiang H-C, Choksi S, … Liu Z-G. Plasma membrane translocation of trimerized MLKL protein is required for TNF-induced necroptosis. Nat Cell Biol 2013; 16: 55

Caillet-Boudin M-L, Buée L, Sergeant N, Lefebvre B. Regulation of human MAPT gene expression. Mol Neurodegener 2015; 10(28): 1–14

Cenini G, Rub C, Bruderek M, Voos W. Amyloid-peptides interfere with mitochondrial preprotein import competence by a coaggregation process. Mol Biol Cell 2016; 27(21): 3257–3272

Chambers I, Tomlinson SR. The transcriptional foundation of pluripotency. Development 2009; 136(14): 2311–2322

Chan G, White. Modulation of TREM2 by CD33: a protein QTL study integrates Alzheimer loci in human monocytes. 2015; 18(11): 1556–1558

Chandrasekaran A, Avci HX, Ochalek A, Rösingh LN, Molnár K, … Dinnyés A. Comparison of 2D and 3D neural induction methods for the generation of neural progenitor cells from human induced pluripotent stem cells. Stem Cell Res 2017; 25: 139–151

Chatzispyrou IA, Held NM, Mouchiroud L, Auwerx J, Houtkooper RH. Tetracycline antibiotics impair mitochondrial function and its experimental use confounds research Iliana. Cancer Res 2015; 75(21): 4446–4449

Chen K, Wells JL, Otero MC, Lwi SJ, Haase CM, … States U. Well-Being in Caregivers.

2018; 44: 245–255

Choi S, Yh K, M H, C S, S L, … Dy K. A three-dimensional human neural cell culture model of Alzheimer's disease. Nature 2014; 515(7526): 274–278

Choi SH, Kim YH, Hebisch M, Sliwinski C, Lee S, … Kim DY. A three-dimensional human neural cell culture model of Alzheimer's disease. Nature 2014; 515(November 2014): 274–278

Clement CG, Truong LD. An evaluation of Congo red fluorescence for the diagnosis of amyloidosis. Hum Pathol 2014; 45(8): 1766–1772

Cohen AD, Ikonomovic MD, Abrahamson EE, Paljug WR, DeKosky ST, … Klunk WE. Anti-Amyloid Effects of Small Molecule Aβ-Binding Agents in PS1/APP Mice. Lett Drug Des Discov 2009; 6(6): 437

Corder EH, Saunders AM, Strittmatter WJ, Schmechel DE, Gaskell PC, … Pericak-Vance MA. Gene dose of apolipoprotein E type 4 allele and the risk of Alzheimer's disease in late onset families. Science (80-) 1993; 261(5123): 921–923

Crews L, Masliah E. Molecular mechanisms of neurodegeneration in Alzheimer's disease. Hum Mol Genet 2010; 19(R1): 12–20

Cummings J, Lee G, Mortsdorf T, Ritter A, Zhong K. Alzheimer's disease drug development pipeline: 2017. Alzheimer's Dement Transl Res Clin Interv 2017; 3(3): 367–384

Cummings JL, Morstorf T, Zhong K. Alzheimer's disease drug-development pipeline: Few candidates, frequent failures. Alzheimer's Res Ther 2014; 6(4): 1–7

D'Avanzo C, Aronson J, Kim YH, Choi SH, Tanzi RE, Kim DY. Alzheimer's in 3D culture: Challenges and perspectives. BioEssays 2015: n/a-n/a

Dallérac G, Chever O, Rouach N. How do astrocytes shape synaptic transmission? Insights from electrophysiology. Front Cell Neurosci 2013; 7(October): 1–19

Devi L, Anandatheerthavarada HK. Mitochondrial trafficking of APP and alpha synuclein: Relevance to mitochondrial dysfunction in Alzheimer's and Parkinson's diseases. Biochim Biophys Acta - Mol Basis Dis 2010; 1802(1): 11–19

East E, Golding JP, Phillips JB. A versatile 3D culture model facilitates monitoring of astrocytes undergoing reactive gliosis. J Tissue Eng Regen Med 2009; 3(8): 634–646

Elkabetz Y, Panagiotakos G, Al Shamy G, Socci ND, Tabar V, Studer L. Human ES cell-derived neural rosettes reveal a functionally distinct early neural stem cell stage. Genes Dev 2008; 22(2): 152–165

Falk A, Koch P, Kesavan J, Takashima Y, Ladewig J, … Brüstle O. Capture of neuroepithelial-like stem cells from pluripotent stem cells provides a versatile system for in vitro production of human neurons. PLoS One 2012; 7(1): 1–13

Finder VH, Glockshuber R. Amyloid-β aggregation. Neurodegener Dis 2007; 4(1): 13–27

Forrest VJ, Kang Y-H, McClain DE, Robinson DH, Ramakrishnan N. Oxidative stress-induced apoptosis prevented by trolox. Free Radic Biol Med 1994; 16(6): 675–684

Friedrich RP, Tepper K, Rönicke R, Soom M, Westermann M, … Fändrich M. Mechanism of amyloid plaque formation suggests an intracellular basis of Abeta pathogenicity. Proc Natl Acad Sci U S A 2010; 107(5): 1942–1947

Fukutani Y, Kobayashi K, Nakamura I, Watanabe K, Isaki K, Cairns NJ. Neurons, intracellular and extracellular neurofibrillary tangles in subdivisions of the hippocampal cortex in normal ageing and Alzheimer's disease. Neurosci Lett 1995; 200(1): 57–60

Garrido-Gil P, Rodriguez-Perez AI, Dominguez-Meijide A, Guerra MJ, Labandeira-Garcia JL. Bidirectional Neural Interaction Between Central Dopaminergic and Gut Lesions in Parkinson's Disease Models. Mol Neurodegener 2018

Gate D, Rezai-Zadeh K, Jodry D, Rentsendorj A, Town T. Macrophages in Alzheimer's disease: The blood-borne identity. J Neural Transm 2010; 117(8): 961–970

Goedert M, Eisenberg DS, Crowther RA. Propagation of Tau Aggregates and Neurodegeneration. Annu Rev Neurosci 2017; 40: 189–210

Gorris R, Fischer J, Erwes KL, Kesavan J, Peterson DA, … Brüstle O. Pluripotent stem cell-derived radial glia-like cells as stable intermediate for efficient generation of human oligodendrocytes. Glia 2015; 63(12): 2152–2167

Grabher BJ. Effects of Alzheimer Disease on Patients and Their Family. J Nucl Med Technol 2018; 46(4): 335–341

Grathwohl SA, Kälin RE, Bolmont T, Prokop S, Winkelmann G, … Mathews PM. Formation and maintenance of Alzheimer's disease β-amyloid plaques in the absence of microglia. Nat Neurosci 2009; 12(11): 1361–1363

Guerreiro R, Wojtas A, Bras J, Carrasquillo M, Rogaeva E, … Hardy J. TREM2 Variants in Alzheimer's Disease. N Engl J Med 2013; 368(2): 117–127

Hall CN, Klein-Flügge MC, Howarth C, Attwell D. Oxidative phosphorylation, not glycolysis, powers pre- and postsynaptic mechanisms underlying brain information processing. J Neurosci 2012; 32(26): 8940–8951

Hane F, Leonenko Z. Effect of Metals on Kinetic Pathways of Amyloid-β Aggregation. Biomolecules 2014; 4: 101–116

He WT, Wan H, Hu L, Chen P, Wang X, … Han J. Gasdermin D is an executor of pyroptosis and required for interleukin-1β secretion. Cell Res 2015; 25(12): 1285–1298

Hebert LE, Weuve J, Scherr PA, Evans DA. Alzheimer disease in the United States (2010–2050) estimated using the 2010 census. Neurology 2013; 80(19): 1778 LP-1783

Hellwig S, Masuch A, Nestel S, Katzmarski N, Meyer-Luehmann M, Biber K. Forebrain microglia from wild-type but not adult 5xFAD mice prevent amyloid-β plaque formation in organotypic hippocampal slice cultures. Sci Rep 2015; 5(April): 14624

Hoffmann D, Schott JW, Geis FK, Lange L, Müller F-J, … Schambach A. Detailed comparison of retroviral vectors and promoter configurations for stable and high transgene expression in human induced pluripotent stem cells. Gene Ther 2017; 24: 298

Hong S, Beja-glasser VF, Nfonoyim BM, Frouin A, Ramakrishnan S, … Stevens B. Complement and Microglia Mediate Early Synapse Loss in Alzheimer Mouse Models. Science (80-) 2016; 352(6286): 712–716

Hoshi A, Tsunoda A, Yamamoto T, Tada M, Kakita A, Ugawa Y. Altered expression of glutamate transporter-1 and water channel protein aquaporin-4 in human temporal cortex with Alzheimer's disease. Neuropathol Appl Neurobiol 2018: n/a--n/a

Hotta A, Ellis J. Retroviral Vector Silencing During iPS Cell Induction: An Epigenetic Beacon that Signals Distinct Pluripotent States. J Cell Biochem 2008; 105: 940–948

Hsiao KK, Borchelt DR, Olson K, Johannsdottir R, Kitt C, … Carlson G. Age-related CNS disorder and early death in transgenic FVB/N mice overexpressing Alzheimer amyloid precursor proteins. Neuron 1995; 15(5): 1203–1218

Hu WT, Watts KD, Shaw LM, Howell JC, Trojanowski JQ, … Levey AI. CSF beta-amyloid 1–42 – what are we measuring in Alzheimer's disease? Ann Clin Transl Neurol 2015; 2(2): 131–139

Huang YA, Zhou B, Wernig M, Su TC, Huang YA, … Suedhof TC. ApoE2, ApoE3, and ApoE4 Differentially Stimulate APP Transcription and Ab Secretion. Cell 2017: 427–441

Huang Y, Mucke L. Alzheimer mechanisms and therapeutic strategies. Cell 2012; 148(6): 1204–1222

Inoue M, Kaida S, Nakano S, Annoni C, Nakata E, Konno T. Phosphorylation regulates fibrillation of an aggregation core peptide in the second repeat of microtubule-binding domain of human tau. Bioorg Med Chem 2014; 22(22): 6471–6480

Irwin DJ, Brettschneider J, McMillan CT, Cooper F, Olm C, … Trojanowski JQ. Deep Clinical and Neuropathological Phenotyping of Pick's Disease. Ann Neurol 2016; 79(2): 272–287

Jaunmuktane Z, Mead S, Ellis M, Wadsworth JDF, Nicoll AJ, … Brandner S. Evidence for human transmission of amyloid-β pathology and cerebral amyloid angiopathy. Nature 2015; 525(7568): 247–250

Jeganathan S, Hascher A, Chinnathambi S, Biernat J, Mandelkow E. Proline-directed Pseudo-phosphorylation at AT8 and PHF1 Epitopes Induces a Compaction of the Paperclip Folding of Tau and Generates a Pathological (MC-1) Conformation. J Biol Chem 2008; 283(46): 32066–32076

Jensen JB, Parmar M. Strengths and limitations of the neurosphere culture system - Jensen and Parmar Mol Neurobiol 2006 (1).pdf. Mol Neurobiol 2006; 34(3): 153–161

Jinek M, East A, Cheng A, Lin S, Ma E, Doudna J. RNA-programmed genome editing in human cells. Elife 2013; 2013(2): 1–9

Joh Y, Choi W-S. Mitochondrial Complex I Inhibition Accelerates Amyloid Toxicity. Dev Reprod 2017; 21(4): 417–424

Jorfi M, Avanzo CD, Tanzi RE, Kim DY, Irimia D. Human Neurospheroid Arrays for In Vitro Studies of Alzheimer ' s Disease. Sci Rep 2018; 8: 1–13

Joung JK, Sander JD. TALENs: a widely applicable technology for targeted genome. Nat Rev Mol Cell Biol 2013; 14(1): 49–55

Kalback W, Watson MD, Kokjohn TA, Kuo Y, Weiss N, … Roher AE. APP Transgenic Mice Tg2576 Accumulate A Peptides That Are Distinct from the Chemically Modified and Insoluble Peptides Deposited in Alzheimer ' s Disease Senile Plaques †. Biochemistry 2002; 41: 922–928

Kanaan NM, Pigino GF, Brady ST, Lazarov O, Binder LI, Morfini GA. Axonal degeneration in Alzheimer's disease: When signaling abnormalities meet the axonal transport system. Exp Neurol 2013; 246: 44–53

Karagiannis P, Takahashi K, Saito M, Yoshida Y, Okita K, … Osafune K. Induced pluripotent stem cells and their use in human models of disease and development. Physiol Rev 2019; 99(1): 79–114

Kaufman AC, Salazar S V., Haas LT, Yang J, Kostylev MA, … Strittmatter SM. Fyn Inhibition Rescues Established Memory and Synapse Loss in Alzheimer Mice. Ann Neurol 2015; 77(6): 953–971

Kim YH, Choi SH, Avanzo CD, Hebisch M, Bylykbashi E, … Kim DY. A 3D human neural cell culture system for modeling Alzheimer's disease. Nat Protoc 2015; 10(7): 985–1006

Koch P, Breuer P, Peitz M, Jungverdorben J, Kesavan J, … Brüstle O. Excitation-induced ataxin-3 aggregation in neurons from patients with Machado–Joseph disease. Nature 2011: 0–5

Koch P, Opitz T, Steinbeck J a, Ladewig J, Brüstle O. A rosette-type, self-renewing human ES cell-derived neural stem cell with potential for in vitro instruction and synaptic integration. Proc Natl Acad Sci U S A 2009; 106(9): 3225–3230

Kotin RM, Linden RM, Berns KI. Characterization of a preferred site on human chromosome 19q for integration of adeno-associated virus DNA by non-homologous recombination. EMBO J 1992; 11(13): 5071–5078

Kroemer G, Galluzzi L, Vandenabeele P, Abrams J, Alnemri E, … Melino G.

Classification of Cell Death: Recommendations of the Nomenclature Committee on Cell Death 2009. Cell Death Differ 2009; 16(1): 3–11

Kühlbrandt W. Structure and function of mitochondrial membrane protein complexes. BMC Biol 2015; 13(1): 1–11

Kuo Y, Kokjohn TA, Beach TG, Sue LI, Brune D, … Roher AE. Comparative Analysis of Amyloid-b Chemical Structure and Amyloid Plaque Morphology of Transgenic Mouse and Alzheimer's Disease Brains. J Biol Chem 2001; 276(16): 12991–12998

Kwak SS, Washicosky KJ, Brand E, von Maydell D, Aronson J, … Kim DY. Amyloid-β42/40 ratio drives tau pathology in 3D human neural cell culture models of Alzheimer's disease. Nat Commun 2020; 11(1): 1377

Kwan AC, Duff K, Gouras GK, Webb WW. Optical visualization of Alzheimer's pathology via multiphoton-excited intrinsic fluorescence and second harmonic generation. Opt Express 2009; 17(5): 3679–3689

LaFramboise T. Single nucleotide polymorphism arrays: A decade of biological, computational and technological advances. Nucleic Acids Res 2009; 37(13): 4181–4193

Lalonde R, Dumont M, Staufenbiel M, Strazielle C. Neurobehavioral characterization of APP23 transgenic mice with the SHIRPA primary screen. Behav Brain Res 2005; 157(1): 91–98

Lancaster MA, Knoblich J. Generation of Cerebral Organoids from Human Pluripotent Stem. Nat Protoc 2015; 9(10): 2329–2340

Lane CA, Hardy J, Schott JM. Alzheimer's disease. Eur J Neurol 2018; 25: 59–70

Lehmann S, Delaby C, Boursier G, Catteau C, Ginestet N, … Gabelle A. Relevance of Aβ42/40 ratio for detection of Alzheimer disease pathology in clinical routine: The PLMRscale. Front Aging Neurosci 2018; 10(MAY): 1–8

Liebmann T, Renier N, Bettayeb K, Greengard P, Flajolet M, … Flajolet M. Three-Dimensional Study of Alzheimer ' s Disease Hallmarks Using the iDISCO Clearing Method Resource Three-Dimensional Study of Alzheimer ' s Disease Hallmarks Using the iDISCO Clearing Method. CellReports 2016; 16(4): 1138–1152

Liedmann A, Frech S, Morgan PJ, Rolfs A, Frech MJ. Differentiation of Human Neural Progenitor Cells in Functionalized Hydrogel Matrices. Biores Open Access 2012; 1(1): 16–24

Lin MT, Beal MF. Alzheimer's APP mangles mitochondria. Nat Med 2006; 12(11): 1241–1243

Liu C-C, Zhao N, Yamaguchi Y, Cirrito JR, Kanekiyo T, … Bu G. Neuronal heparan sulfates promote amyloid pathology by modulating brain amyloid-β clearance and aggregation in Alzheimer's disease. Sci Transl Med 2016; 8(332): 332ra44-332ra44

López-Crisosto C, Bravo-Sagua R, Rodriguez-Peña M, Mera C, Castro PF, … Lavandero S. ER-to-mitochondria miscommunication and metabolic diseases. Biochim Biophys Acta - Mol Basis Dis 2015; 1852(10): 2096–2105

Lund RJ, Närvä E, Lahesmaa R. Genetic and epigenetic stability of human pluripotent stem cells. Nat Rev Genet 2012; 13(10): 732–744

McMahon SB. Emerging concepts in the analysis of transcriptional targets of the MYC oncoprotein: Are the targets targetable? Genes and Cancer 2010; 1(6): 560–567

Meijering E, Jacob M, Sarria JF, Steiner P, Hirling H, Unser M. Design and Validation of a Tool for Neurite Tracing and Analysis in Fluorescence Microscopy Images. Cytometry 2004; 58(2): 167–176

Mertens J, Stüber K, Poppe D, Doerr J, Ladewig J, … Koch P. Embryonic stem cell-based modeling of tau pathology in human neurons. Am J Pathol 2013; 182(5): 1769–1779

Michaelson DM. APOE ε4: The most prevalent yet understudied risk factor for Alzheimer's disease. Alzheimer's Dement 2014; 10(6): 861–868

Mirra SS, Heyman A, McKeel D, Sumi SM, Crain BJ, … Berg L. The Consortium to Establish a Registry for Alzheimer's Disease (CERAD). Neurology 1991; 41(4): 479–479

Mizuguchi H, Xu Z, Ishii-Watabe A, Uchida E, Hayakawa T. IRES-Dependent Second Gene Expression Is Significantly Lower Than Cap-Dependent First Gene Expression in a Bicistronic Vector. Mol Ther 2000; 1(4): 376–382

Mizuno KI, Lambert S, Baldacci G, Murray JM, Carr AM. Nearby inverted repeats fuse to generate acentric and dicentric palindromic chromosomes by a replication template exchange mechanism. 2009: 2876–2886

Motoki K, Kume H, Oda A, Tamaoka A, Hosaka A, … Araki W. Neuronal β-amyloid generation is independent of lipid raft association of β-secretase BACE1: analysis with a palmitoylation-deficient mutant. Brain Behav 2012; 2(3): 270–282

Mucke L, Masliah E, Yu GQ, Mallory M, Rockenstein EM, … McConlogue L. High-level neuronal expression of abeta 1-42 in wild-type human amyloid protein precursor transgenic mice: synaptotoxicity without plaque formation. J Neurosci 2000; 20(11): 4050–4058

Mudher A, Colin M, Dujardin S, Medina M, Dewachter I, … Brion J. What is the evidence that tau pathology spreads through prion-like propagation? Acta Neuropathol Commun 2017; 5(99): 1–20

Muguruma K, Nishiyama A, Kawakami H, Hashimoto K, Sasai Y. Self-Organization of Polarized Cerebellar Tissue in 3D Culture of Human Pluripotent Stem Cells. Cell Rep 2015; 10(4): 537–550

Mukherjee SK, Yasharel R, Klaidman LK, Hutchin TP, Adams JD. Apoptosis and dna fragmentation as induced by tertiary butylhydroperoxide in the brain. Brain Res Bull 1995; 38(6): 595–604

Müller FJ, Schuldt BM, Williams R, Mason D, Altun G, … Loring JF. A bioinformatic assay for pluripotency in human cells. Nat Methods 2011; 8(4): 315–317

Naj AC, Jun G, Reitz C, Kunkle BW, Perry W, … Yu L. Effects of multiple genetic loci on age at onset in late-onset Alzheimer disease: a genome-wide association study. JAMA Neurol 2014; 71(11): 1394–1404

Nalivaeva NN, Turner AJ. The amyloid precursor protein: A biochemical enigma in brain development, function and disease. FEBS Lett 2013; 587(13): 2046–2054

Nault J-C, Datta S, Imbeaud S, Franconi A, Zucman-Rossi J. Adeno-associated virus type 2 as an oncogenic virus in human hepatocellular carcinoma. Mol Cell Oncol 2016; 3(2): e1095271

Neniskyte U, Fricker M, Brown GC. Amyloid β induces microglia to phagocytose neurons via activation of protein kinase Cs and NADPH oxidase. Int J Biochem Cell Biol 2016; 81: 346–355

Ni HM, Williams JA, Ding WX. Mitochondrial dynamics and mitochondrial quality control. Redox Biol 2015; 4: 6–13

Oddo S, Caccamo A, Shepherd JD, Murphy MP, Golde TE, … LaFerla FM. Triple-transgenic model of Alzheimer's Disease with plaques and tangles: Intracellular Aβ and synaptic dysfunction. Neuron 2003; 39(3): 409–421

Oliveira PH, Da Silva CL, Cabral JMS. Concise review: Genomic instability in human stem cells: Current status and future challenges. Stem Cells 2014; 32: 2824–2832

Olsson F, Schmidt S, Althoff V, Munter LM, Jin S, … Lundkvist J. Characterization of intermediate steps in amyloid beta (Aβ) production under near-native conditions. J Biol Chem 2014; 289(3): 1540–1550

Owens R a. Second generation adeno-associated virus type 2-based gene therapy systems with the potential for preferential integration into AAVS1. Curr Gene Ther 2002; 2(2): 145–159

Paasch F, Den Brave F, Psakhye I, Pfander B, Jentsch S. Failed mitochondrial import and impaired proteostasis trigger SUMOylation of mitochondrial proteins. J Biol Chem 2018; 293(2): 599–609

Papapetrou EP, Schambach A. Gene insertion into genomic safe harbors for human gene therapy. Mol Ther 2016; 24(4): 678–684

Peitz M, Jungverdorben J, Brüstle O. Disease-specific iPS cell models in neuroscience. Curr Mol Med 2013; 13(5): 832–841

Pensalfini A, Iii RA, Rasool S, Wu J, Hatami A, … Corrada M. Intracellular amyloid and the neuronal origin of Alzheimer neuritic plaques. Neurobiol Dis 2014: 53–61

Perl DP. Neuropathology of Alzheimer's Disease. Mt Sinai J Med 2010; 77(1): 32–42

Petersen R, Doody R, Kurz A, Mohs R, Morris J, … Winblad B. Current Concepts in Mild Cognitive Impairment. Arch Neurol 2001; 58

Petersen RC, Lopez O, Armstrong MJ, Getchius TSD. Practice guideline update summary : Mild cognitive impairment Report of the Guideline Development , Dissemination , and Implementation. Neurology 2018; 90(3): 126–135

Pfeifer D, Pantic M, Skatulla I, Rawluk J, Kreutz C, … Veelken H. Genome-wide analysis of DNA copy number changes and LOH in CLL using high-density SNP arrays. Neoplasia 2006; 109(3): 1202–1211

Pinho CM, Teixeira PF, Glaser E. Mitochondrial import and degradation of amyloid-β peptide. Biochim Biophys Acta - Bioenerg 2014; 1837(7): 1069–1074

Placone AF, McGuiggan PM, Bergles DE, Guerrero-Cazares H, Quiñones-hinojosa A, Searson PC. Human Astrocytes Develop Physiological Morphology and Remain Quiescent in a Novel 3D Matrix. Biomaterials 2015; 42: 134–143

Preibisch S, Saalfeld S, Tomancak P. Globally optimal stitching of tiled 3D microscopic image acquisitions. Bioinformatics 2009; 25(11): 1463–1465

Qian K, Huang C-L, Chen H, Blackbourn LW, Chen Y, … Zhang S-C. A simple and efficient system for regulating gene expression in human pluripotent stem cells and derivatives. Stem Cells 2014; 32(5): 1230–1238

Ran FA, Hsu PD, Wright J, Agarwala V, Scott DA, Zhang F. Genome engineering using the CRISPR-Cas9 system. Nat Protoc 2013; 8(11): 2281–2308

Rebuzzini P, Zucotti M, Redi CA, Garagna S. Chromosomal Abnormalities in Embryonic and Somatic Stem Cells. Cytogenet Genome Res 2015; 147: 1–9

Richards RI, Robertson S a., O'Keefe L V., Fornarino D, Scott A, … Baune BT. The Enemy within: Innate Surveillance-Mediated Cell Death, the Common Mechanism of Neurodegenerative Disease. Front Neurosci 2016; 10(May): 1–20

Roese-koerner B, Stappert L, Berger T, Braun NC, Veltel M, … Bru O. Reciprocal Regulation between Bifunctional miR-9/9* and its Transcriptional Modulator Notch in Human Neural Stem Cell Self-Renewal and Differentiation. Stem Cell Reports 2016; 7

Sadleir KR, Kandalepas PC, Buggia-Prévot V, Nicholson D a., Thinakaran G, Vassar R. Presynaptic dystrophic neurites surrounding amyloid plaques are sites of microtubule disruption, BACE1 elevation, and increased Aβ generation in Alzheimer's disease. Acta Neuropathol 2016; 132(2): 1–22

Sasaguri H, Nilsson P, Hashimoto S, Nagata K, Saito T, … Saido TC. APP mouse

models for Alzheimer's disease preclinical studies. EMBO J 2017; 36(17): e201797397

Scheffler K, Stenzel J, Krohn M, Lange C, Hofrichter J, … Pahnke J. Determination of spatial and temporal distribution of microglia by 230nm-high-resolution, high-throughput automated analysis reveals different amyloid plaque populations in an APP/PS1 mouse model of Alzheimer's disease. Curr Alzheimer Res 2011; 8(7): 781–788

Schoch KMM, DeVos SLL, Miller RLL, Chun SJJ, Norrbom M, … Miller TMM. Increased 4R-Tau Induces Pathological Changes in a Human-Tau Mouse Model. Neuron 2016; 90(5): 941–947

Schoch KMM, DeVos SLL, Miller RLL, Chun SJJ, Norrbom M, … Miller TMM. Increased 4R-Tau Induces Pathological Changes in a Human-Tau Mouse Model. Neuron 2016; 90(5): 941–947

Schwarz MK, Scherbarth A, Sprengel R, Engelhardt J, Theer P, Giese G. Fluorescent-protein stabilization and high-resolution imaging of cleared, intact mouse brains. PLoS One 2015; 10(5): 1–26

Selkoe DJ, Hardy J, Selkoe D, Hardy J. The amyloid hypothesis of Alzheimer ' s disease at 25 years. EMBO Mol Med 2016; 8(6): 595–608

Serrano-Pozo A, Frosch MP, Masliah E, Hyman BT. Neuropathological Alterations in Alzheimer Disease. Cold Spring Harb Perspect Med 2011: 1–23

Shi Y, Inoue H, Wu JC, Yamanaka S. Induced pluripotent stem cell technology: A decade of progress. Nat Rev Drug Discov 2017; 16(2): 115–130

Shi Y, Kirwan P, Livesey FJ. Directed differentiation of human pluripotent stem cells to cerebral cortex neurons and neural networks. Nat Protoc 2012; 7(10): 1836–1846

Shi Y, Kirwan P, Smith J, MacLean G, Orkin SH, Livesey FJ. A human stem cell model of early Alzheimer's disease pathology in Down syndrome. Sci Transl Med 2012; 4(124): 124ra29

Shirwany N a., Payette D, Xie J, Guo Q. The amyloid beta ion channel hypothesis of Alzheimer's disease. Neuropsychiatr Dis Treat 2007; 3(5): 597–612

Simunovic M, Brivanlou AH. Embryoids, organoids and gastruloids: new approaches to understanding embryogenesis. Development 2017; 144(6): 976–985

Snowdon DA. Healthy Aging and Dementia: Findings from the Nun Study. Ann Intern Med 2003; 139: 450–454

Solito E, Sastre M. Microglia function in Alzheimer's disease. Front Pharmacol 2012; 3 FEB(February): 1–10

Söllvander S, Nikitidou E, Brolin R, Söderberg L, Sehlin D, … Erlandsson A. Accumulation of amyloid-β by astrocytes result in enlarged endosomes and microvesicle-induced apoptosis of neurons. Mol Neurodegener 2016; 11(1): 38

Sproul AA, Jacob S, Pre D, Kim SH, Nestor MW, … Noggle SA. Characterization and Molecular Profiling of PSEN1 Familial Alzheimer ' s Disease iPSC-Derived Neural Progenitors. PLoS One 2014; 9(1)

Stieger K, Belbellaa B, Le Guiner C, Moullier P, Rolling F. In vivo gene regulation using tetracycline-regulatable systems. Adv Drug Deliv Rev 2009; 61(7–8): 527–541

Stoothoff WH, Johnson GVW. Tau phosphorylation: Physiological and pathological consequences. Biochim Biophys Acta - Mol Basis Dis 2005; 1739(2): 280–297

Stroud JC, Liu C, Teng PK, Eisenberg D. Toxic fibrillar oligomers of amyloid-β have cross-β structure. Proc Natl Acad Sci U S A 2012; 109(20): 7717–7722

Sugiyama Y, Fujita T. Stimulation of the respiratory and phosphorylating activities in rat brain mitochondria by idebenone (CV-2619), a new agent improving cerebral metabolism. FEBS Lett 1985; 184(1): 48–51

Tait SWG, Ichim G, Green DR. Die another way – non-apoptotic mechanisms of cell death. J Cell Sci 2014; 127(10): 2135–2144

Takahashi K, Tanabe K, Ohnuki M, Narita M, Ichisaka T, … Yamanaka S. Induction of pluripotent stem cells from adult human fibroblasts by defined factors. Cell 2007; 131(5): 861–872

Takahashi K, Yamanaka S. Induction of pluripotent stem cells from mouse embryonic and adult fibroblast cultures by defined factors. Cell 2006; 126(4): 663–676

Takahashi RH, Milner T a, Li F, Nam EE, Edgar M a, … Gouras GK. Intraneuronal Alzheimer abeta42 accumulates in multivesicular bodies and is associated with synaptic pathology. Am J Pathol 2002; 161(5): 1869–1879

Tanokashira D, Mamada N, Yamamoto F, Taniguchi K, Tamaoka A, … Araki W. The neurotoxicity of amyloid β-protein oligomers is reversible in a primary neuron model. Mol Brain 2017; 10(1): 1–10

Thal LJ, Grundman M, Berg J, Ernstrom K, Margolin R, … Thomas RG. Idebenone treatment fails to slow cognitive decline in Alzheimer's disease. Neurology 2003; 61(11): 1498 LP-1502

Thériault P, ElAli A, Rivest S. The dynamics of monocytes and microglia in Alzheimer's disease. Alzheimers Res Ther 2015; 7(1): 41

Thomson JA, Joseph I-E, Shapiro SS, Waknitz MA, Swiergiel JJ, … Jones JM. Embryonic Stem Cell Lines Derived from Human Blastocysts. Science (80-) 1998; 282(5391): 1145–1147

Thonhoff JR, Lou DI, Jordan PM, Zhao X, Wu P. Compatibility of human fetal neural stem cells with hydrogel biomaterials in vitro. Brain Res 2008; 1187: 42–51

Tsankov AM, Akopian V, Pop R, Chetty S, Gifford CA, … Meissner A. An improved

ScoreCard to assess the differentiation potential of human pluripotent stem cells. Nat Biotechnol 2016; 33(11): 1182–1192

Tun H, Marlow L, Pinnix I, Kinsey R, Sambamurti K. Lipid rafts play an important role in A beta biogenesis by regulating the beta-secretase pathway. J Mol Neurosci 2002; 19(1–2): 31–35

Tyan S-H, Shih AY-J, Walsh JJ, Murayama H, Sarsoza F, … Dickstein DL. Amyloid precursor protein (APP) regulates synaptic structure and function. Mol Cell Neurosci 2012; 51: 43–52

Umar T, Hoda N. Alzheimer's Disease: A Systemic Review Of Substantial Therapeutic Targets And The Leading Multi-Functional Molecules. Curr Top Med Chem 2017; 17: 3370–3389

Urnov FD, Rebar EJ, Holmes MC, Zhang HS, Gregory PD. Genome editing with engineered zinc finger nucleases. Nat Rev Genet 2010; 11(9): 636–646

Vanderweyde T, Apicco DJ, Youmans-kidder K, Li H, Petrucelli L, … Wolozin B. Interaction of tau with the RNA-Binding Protein TIA1 Regulates tau Pathophysiology and Toxicity. Cell Rep 2016; 15: 1455–1466

Vargas JE, Chicaybam L, Stein RT, Tanuri A, Delgado-Cañedo A, Bonamino MH. Retroviral vectors and transposons for stable gene therapy: Advances, current challenges and perspectives. J Transl Med 2016; 14(1): 1–15

Verret L, Mann EO, Hang GB, Barth AMI, Cobos I, … Palop JJ. Inhibitory Interneuron Deficit Links Altered Network Activity and Cognitive Dysfunction in Alzheimer Model. Cell 2012; 149(3): 708–721

Villemagne VL, Doré V, Burnham SC, Masters CL, Rowe CC. Imaging tau and amyloid-β proteinopathies in Alzheimer disease and other conditions. Nat Rev Neurol 2018

Vina J, Lloret A. Why Women Have More Alzheimer ' s Disease Than Men : Gender and Mitochondrial Toxicity of Amyloid- β Peptide. J Alzheimer's Dis 2010; 20: 527–533

Vinters H V, Hyman BT. National Institute on Aging-Alzheimer's Association guidelines for the neuropathologic assessment of Alzheimer's disease: a practical approach. Acta Neuropathol 2012; 123(1): 1–11

Wang W, Yin J, Ma X, Zhao F, Siedlak SL, … Zhu X. Inhibition of mitochondrial fragmentation protects against Alzheimer's disease in rodent model. Hum Mol Genet 2017; 26(21): 4118–4131

Wiseman FK, Al-Janabi T, Hardy J, Karmiloff-Smith A, Nizetic D, … Strydom A. A genetic cause of Alzheimer disease: mechanistic insights from Down syndrome. Nat Rev Neurosci 2015; 16(9): 564–574

Wurtman R. Biomarkers in the diagnosis and management of Alzheimer's disease.

Metabolism 2015; 64(3): S47–S50

Yang N, Chanda S, Marro S, Ng Y, Janas JA, … Wernig M. Generation of pure GABAergic neurons by transcription factor programming. Nat Publ Gr 2017(may)

Yu C, Liu Y, Ma T, Kai L, Xu S, … Qi LS. Small Molecules Enhance CRISPR Genome Editing in Pluripotent Stem Cells. Cell Stem Cell 2015; 16(2): 142–147

Yu J, Vodyanik MA, Kim S-O, Jessica A-B, Frane JL, … Thomson JA. Induced pluripotent stem cell lines derived from human somatic cells. Sci {(New} York, {NY)} 2007; 318(5858): 1917–1920

Zhang D, Pekkanen-Mattila M, Shahsavani M, Falk A, Teixeira AI, Herland A. A 3D Alzheimer's disease culture model and the induction of P21-activated kinase mediated sensing in iPSC derived neurons. Biomaterials 2014; 35(5): 1420–1428

Zhang L, Zhang S, Maezawa I, Trushin S, Minhas P, … Trushina E. Modulation of Mitochondrial Complex I Activity Averts Cognitive Decline in Multiple Animal Models of Familial Alzheimer's Disease. EBioMedicine 2015; 2(4): 294–305

Zhang XH, Tee LY, Wang XG, Huang QS, Yang SH. Off-target effects in CRISPR/Cas9-mediated genome engineering. Mol Ther - Nucleic Acids 2015; 4(11): e264

Zhang Y, Pak C, Han Y, Ahlenius H, Zhang Z, … Drive C. Rapid Sngle-Step Induction of Functional Neurons from Human Pluripotent Stem Cells. Neuron 2013; 78(5): 785–798

Zhang Z-N, Freitas BC, Qian H, Lux J, Acab A, … Almutairi A. Layered hydrogels accelerate iPSC-derived neuronal maturation and reveal migration defects caused by MeCP2 dysfunction. Proc Natl Acad Sci 2016; 113(12): 3185–3190

9. Acknowledgements